

**Coherence Properties of the Entangled
Two-Photon Field Produced by
Parametric Down-Conversion**

by

Anand Kumar Jha

Submitted in Partial Fulfillment of
the Requirements for the Degree
Doctor of Philosophy

Supervised by
Professor Robert W. Boyd

The Institute of Optics
Arts, Sciences and Engineering
Edmund A. Hajim School of Engineering and Applied Sciences

University of Rochester
Rochester, New York

2009

To My Parents, My Sisters, and all My Teachers

Curriculum Vitae

Anand Kumar Jha was born in Darbhanga, India in 1978. His early education was completed in Sarvodaya High School, Darbhanga, India and C. M. Science College, Darbhanga, India. He studied at the Indian Institute of Technology, Kharagpur, India from 1997 to 2002 and obtained his B.Sc. and M.Sc. degrees in Physics. In the fall of 2002, he joined the Physics Ph.D. program at the University of Illinois at Urbana-Champaign, from where he transferred to the University of Rochester in 2003. Since then, he has been a Ph.D. student at the Institute of Optics, University of Rochester, researching the broad area of quantum optics under the supervision of Prof. Robert W. Boyd.

Publications

1. “Temporal coherence and indistinguishability in two-photon interference effects,” A. K. Jha, M. N. O’Sullivan, K. W. C. Chan, and R. W. Boyd, *Phys. Rev. A* **77**, 021801(R) (2008).
2. “Exploring energy-time entanglement using geometric phase,” A. K. Jha, M. Malik, and R. W. Boyd, *Phys. Rev. Lett.* **101**, 180405 (2008).
3. “Fourier relationship between the angle and angular momentum of entangled photons,” A. K. Jha, B. Jack, E. Yao, J. Leach, R. W. Boyd, G. S. Buller, S. M. Barnett, S. Franke-Arnold, and M. J. Padgett, *Phys. Rev. A* **78**, 043810 (2008).
4. “Propagation of quantum states of light through absorbing and amplifying media,” R. W. Boyd, G. S. Agarwal, K. W. C. Chan, A. K. Jha, and M. N. O’Sullivan, *Opt. Comm.* **281**, 3732 (2008).
5. “Violation of a Bell inequality in two-dimensional orbital angular momentum state-spaces,” J. Leach, B. Jack, J. Romero, M. Ritsch-Marte, R. W. Boyd, A. K. Jha, S. M. Barnett, S. Franke-Arnold, and M. J. Padgett, *Opt. Express* **17**, 8287 (2009).
6. “Angular two-qubit states and two-photon angular interference,” A. K. Jha, J. Leach, B. Jack, S. Franke-Arnold, S. M. Barnett, R. W. Boyd, and M. J. Padgett, *submitted to Phys. Rev. Lett.*
7. “Spatial two-photon coherence of the entangled field produced by down-conversion using a partially spatially coherent pump beam,” A. K. Jha and R. W. Boyd, *submitted to Phys. Rev. A*.
8. “Temporal coherence of the entangled two-photon field produced by down-conversion,” A. K. Jha, M. N. O’Sullivan, K. W. C. Chan, and R. W. Boyd, *to be submitted*.

Conference Papers

1. “Entangled light sources for quantum imaging,” R. W. Boyd, K. W. C. Chan, A. K. Jha, M. N. O’Sullivan, and H. Shin, *SPIE Optics+Photonics* (2007).
2. “Fourier relationship between angular position and orbital angular momentum of entangled photons”, A. K. Jha, B. Jack, E. Yao, J. Leach, R. W. Boyd, G. S. Buller, S. M. Barnett, S. Franke-Arnold, and M. J. Padgett, *OSA Annual Meeting* (2008).
3. “Exploring energy-time entanglement using geometric phase,” A. K. Jha, M. Malik, and R. W. Boyd, *CLEO/IQEC* (2009).

Acknowledgments

First of all, I would like to express my deep-felt gratitude to Prof. Robert W. Boyd, my thesis supervisor, for his guidance, support and care. Whatever has been achieved in this thesis is because of the never-ending encouragement, appreciation and help that I have received from him. His philosophy of understanding a concept at the most intuitive level was always a guiding light along my research efforts. Secondly, I thank Prof. Carlos R. Stroud for allowing me to approach him whenever I had a question or a doubt. Discussions with Prof. Stroud always brought much clarity and insight to me. I am grateful to Prof. Emil Wolf for a most insightful course on Coherence Theory that he taught in the fall of 2005. Some of the ideas presented in this thesis are very much inspired from what I learnt during his course. I would also like to sincerely thank Prof. Miles Padgett and his group at the University of Glasgow, Scotland, and Prof. Steve Barnett at the University of Strathclyde, Scotland for a very fruitful collaboration. Most of what is presented in Chapter 4 of this thesis is an outcome of this collaboration. I am thankful also to Prof. Stroud, Prof. Alonso and Prof. Jordan for accepting to be on my thesis committee. I shall always remain indebted to all the staff at the Institute of Optics, especially Maria Schnitzler, Lissa Cotter and Noelene Votens, who, with their infinite patience and loving care, were always there to help. Finally, I thank all the current and past members of Boyd's group for those numerous inspiring discussions, and all my friends at Rochester and elsewhere for their company and well wishes.

Abstract

Parametric down-conversion is a second-order nonlinear optical process in which a pump photon breaks up into two separate photons known as the signal photon and the idler photon. The constraints of energy and momentum conservation render the signal and idler photons entangled in several different variables including time and energy, position and transverse momentum, and angular position and orbital angular momentum. Because of these correlations, the down-converted signal and idler photons can be described adequately only as a single, two-photon system. In this thesis, we present our theoretical and experimental studies of the coherence properties of the down-converted, entangled two-photon fields, through two-photon interference effects in temporal, spatial and angular domains.

First of all, we study the temporal coherence properties of the down-converted two-photon fields, in the limit in which the frequency bandwidth of the pump field is much narrower than that of the down-converted field. We present a formalism to completely characterize temporal two-photon interference effects in terms of the variations of two length parameters—called the two-photon path length difference and the two-photon path-asymmetry length difference—which we construct using the six different length parameters that a general two-photon interference experiment involves. Next, we extend this formalism to describe also the spatial coherence properties of the two-photon field. By explicitly treating the case of a partially spatially coherent pump beam of Gaussian Schell-model type, we show that in parametric down-conversion the spatial coherence properties of the pump field get entirely transferred to the spatial coherence properties of the down-converted two-photon field. As an important consequence of this study, we find that for two-qubit states that are based on the spatial correlations of the down-converted photons, the maximum achievable entanglement is bounded by the degree of spatial coherence of the pump field. In the last part of

this thesis, we study the coherence properties of the entangled two-photon field in the angular domain, by investigating two-photon angular interference effects in situations in which the down-converted photons are made to pass through apertures in the form of double angular-slits.

Contents

Acknowledgments	vi
Abstract	vii
List of Figures	xiii
1 Background	1
1.1 Introduction	1
1.2 Temporal one-photon interference	3
1.3 Spatial one-photon interference	7
1.4 Angular one-photon interference	10
1.5 Basics of nonlinear optics	13
1.6 Two-photon field produced by parametric down-conversion	14
1.7 Quantum entanglement and EPR paradox	17
1.8 Bell inequalities and beyond	19
1.9 Two-photon coherence and two-photon entanglement	21
1.10 Summary	22
2 Two-Photon Coherence Effects: Temporal	24
2.1 Introduction	24
2.2 Two-photon state produced by parametric down-conversion	25
2.3 Representing two-photon interference using path diagrams	30

2.4	Temporal two-photon interference	32
2.5	Time-averaged coincidence count rate	36
2.6	The two correlation functions	40
2.7	Two-photon coherence and the HOM effect	42
2.8	Time-energy entanglement	47
2.9	Bell inequality for time and energy	48
2.10	Exploring time-energy entanglement using geometric phase	51
2.11	Summary	58
3	Two-Photon Coherence Effects: Spatial	60
3.1	Introduction	60
3.2	Two-photon state produced by parametric down-conversion	61
3.3	Spatial two-photon interference: conceptual description	65
3.4	Spatial coherence properties of the two-photon field: the degenerate case	69
3.5	Spatial coherence properties of the two-photon field: the general case	75
3.6	Position-momentum entanglement	79
3.7	Spatial two-photon coherence and entanglement of spatial two-qubit states	80
3.8	Summary	85
4	Two-Photon Coherence Effects: Angular	87
4.1	Introduction	87
4.2	Orbital angular momentum of light	88
4.3	Angular Fourier relationship	91
4.4	Conservation of orbital angular momentum in down-conversion	92
4.5	Angular-position-orbital-angular-momentum entanglement	93
4.6	Angular two-qubit states and two-photon angular interference	94
4.7	Experimental realization of an angular two-qubit state	101
4.8	Summary	104

<i>CONTENTS</i>	xi
5 Conclusions and Discussion	105
Bibliography	109
A Calculating $\gamma'(\Delta L')$ for various phase matching conditions	126
A.1 Filter bandwidths much broader than the down-conversion bandwidth	128
A.2 Filter bandwidths much narrower than the down-conversion bandwidth	130
B Induced coherence experiment	131

List of Figures

1.1	Temporal one-photon interference in a Michelson interferometer	5
1.2	Schematic representation of spatial one-photon interference	8
1.3	Schematic representation of angular one-photon interference	11
1.4	Nonlinear optical process of parametric down-conversion	16
2.1	Producing two-photon fields by parametric down-conversion	26
2.2	Schematic representation of temporal two-photon interference using two-photon path diagrams	31
2.3	Schematic of a Hong-Ou-Mandel (HOM) experiment	43
2.4	Schematic of the double-pass setup	44
2.5	Experimental results in the double-pass setup	45
2.6	Franson interferometer	50
2.7	Experimental setup to show a geometric-phase-based violation of Bell's inequality	52
2.8	Poincaré-sphere representation of polarization states	54
2.9	Measured number of coincidence counts as a function of the geometric phase of signal photon	56
3.1	Schematic representation of spatial two-photon interference	66
3.2	Schematic representation of a partially spatially coherent pump beam	72
3.3	Physical interpretation of the two-photon correlation width and the two-photon transverse coherence width	74

3.4	A generic scheme to prepare spatial two-qubit states.	81
4.1	The intensity and phase patterns of the first three Laguerre-Gaussian modes	89
4.2	Schematic of a method used to generate Laguerre-Gaussian beams . .	90
4.3	Schematic of the setup used for preparing angular two-qubit states . .	96
4.4	Measurements of the OAM-mode probabilities	102
4.5	Measurements in the angular position basis	102
4.6	Measurements in the OAM basis	103
B.1	Schematic of the induced-coherence experiment	132

Chapter 1

Background

1.1 Introduction

The superposition principle, which underlies all interference effects, is at the heart of quantum mechanics [1]. Feynman referred to interference as the only mystery of quantum mechanics. Interference effects have been studied with one-photon fields [2], with two-photon fields [3, 4, 5, 6, 7, 8, 9, 10], and also with three- [11] and four-photon fields [12]. In a one-photon interference experiment, a single detector is used to measure the probability of detecting a photon as a function of time or space. As this probability depends on the second power of the field and on the detection of one photon at a time, this is referred to as one-photon or second-order interference. Interference experiments in which two detectors are used in coincidence to measure the joint probability of detecting two separate photons are referred to as two-photon or fourth-order interference experiments, because the joint probability in this case depends on the fourth power of the field. The study of one-photon interference dates back to Thomas Young's classic double-slit experiment in the beginning of the 19th century, while the study of multi-photon interference effects can be said to have started with the experiments of Hanbury-Brown and Twiss [13, 14]. Multi-photon interference became an active field of research after the experiments to test the Bell

inequalities began in the 1960s [15, 16].

In some of the multi-photon interference experiments, the concept of quantum entanglement is naturally encountered, which has also been described as really the only quantum mystery and which led Einstein, Podolsky and Rosen to conclude that the quantum mechanical description of physical reality was incomplete [17]. Multi-photon interference effects play important roles in many practical applications as well as in fundamental research. Through two-photon interference experiments, violations of Bell inequalities [18] have been reported for many degrees of freedom [7, 8, 9, 19, 20, 21, 22], which have established the incompatibility of the local hidden variable interpretations [23, 24] of quantum mechanics. Multi-photon interference effects are also central to many quantum information and quantum computation protocols including quantum cryptography [25], quantum dense coding [26], quantum teleportation [27], entanglement swapping [28], and quantum lithography [29]. Semi-classical descriptions of some of the multi-photon effects were provided by Mandel and Wolf [30]. However, the complete quantum-mechanical framework to describe multi-photon effects was worked out by Glauber [31, 32].

This thesis focuses on those two-photon interference effects that involve entangled two-photon fields produced by parametric down-conversion (PDC). Parametric down-conversion is the most widely used process for producing entangled two-photon fields; it is a second-order nonlinear optical process that takes place in non-centrosymmetric crystals. In parametric down-conversion, a photon of higher frequency interacts with a nonlinear crystal and gets down-converted into two separate photons of lower frequencies [33]. The photon of higher frequency is called the pump photon and the photons of lower frequencies are called the signal and idler photons. The constraints of energy and momentum conservation in PDC render the two photons entangled in various degrees of freedom. Entanglement of the two photons in a given degree of freedom manifests itself as two-photon coherence in the corresponding domain. This thesis studies the coherence properties of the entangled two-photon field produced by

parametric down-conversion, through two-photon interference effects in the temporal, spatial and angular domains. There are other processes, such as four-wave mixing [34, 35] that also produce entangled two-photon fields, but throughout this thesis, we consider only the entangled two-photon fields that are produced by parametric down-conversion.

This chapter is organized as follows. Sections 1.2, 1.3, and 1.4 present conceptual descriptions of one-photon interference in the temporal, spatial and angular domains, respectively. In Sections 1.5 and 1.6, the nonlinear optical process of parametric down-conversion is described in detail. The concept of entanglement in light of the arguments forwarded by Einstein, Podolsky and Rosen is discussed in Section 1.7. In Section 1.8, brief discussions related to Bell inequalities and entanglement measures are presented. Section 1.9 discusses the connection between two-photon coherence and two-photon entanglement and Section 1.10 presents the summary.

1.2 Temporal one-photon interference

The descriptions of one-photon interference presented in this and the next sections are based on the treatment given by Mandel and Wolf [30]. This section describes temporal one-photon interference in a Michelson interferometer [Fig. 1.1(a)]. We take the source to produce a quasi-monochromatic, stationary field of light. By quasi-monochromatic, we mean that the effective frequency bandwidth $\Delta\omega_0$ of the field is small compared with its mean frequency ω_0 [2]. The fields produced by most sources, including continuous-wave lasers, are stationary. In the setup of Fig. 1.1(a), a photon from the source has two alternative pathways by which it can reach detector D_A . These two alternative pathways are shown in Fig. 1.1(b). In alternative 1, a photon first gets reflected by the beam splitter and reaches detector D_A after getting reflected back by the upper mirror. In alternative 2, a photon gets transmitted by the beam splitter and reaches the detector after getting reflected back by the side mirror. These

two alternative pathways can be represented in an unfolded manner by the one-photon path diagrams of Fig. 1.1(c), where l_1 and l_2 denote the optical path lengths traveled by the photons in alternatives 1 and 2, respectively. $\Delta l = l_1 - l_2$ is the difference of the optical path lengths in the two alternatives. The probability amplitudes of these two alternative pathways add up to produce one-photon interference, as long as the two alternative pathways are coherent, that is, indistinguishable from each other [36].

To find the condition for coherence between the two alternatives, we calculate the intensity at detector D_A . We denote the times needed to travel through the alternatives 1 and 2 by $t_1 = l_1/c$ and $t_2 = l_2/c$, respectively, and write the electric field $V_A(t)$ at time t at detector D_A as the sum of the electric fields reaching the detector by the two alternatives pathways:

$$V_A(t) = V_1(t - t_1) + V_2(t - t_2). \quad (1.1)$$

Subscripts 1 and 2 denote the two alternatives, and $V_1(t - t_1)$ and $V_2(t - t_2)$ represent the electric field amplitudes of the source at times $t - t_1$ and $t - t_2$, respectively. The instantaneous intensity $I(t)$ at a point is defined as $I(t) = V^*(t)V(t)$ [30]; Therefore, it follows that the instantaneous intensity $I_A(t)$ at detector D_A is

$$I_A(t) = I_1(t - t_1) + I_2(t - t_2) + V_1^*(t - t_1)V_2(t - t_2) + \text{c.c.} \quad (1.2)$$

The first and second terms are the instantaneous intensities when the electric fields from only alternative 1 and 2, respectively, are incident. The two other terms are due to interference, and they appear when both alternatives are simultaneously incident. Instantaneous intensity is usually the intensity from a single realization of the field. The interference effects observed in the instantaneous intensity distribution are referred to as the transient interference effects. Such effects have been observed in several optical experiments in 1950s and 1960s [37, 38]. However, in most experiments, what is observed is not the instantaneous intensity, or the intensity from a

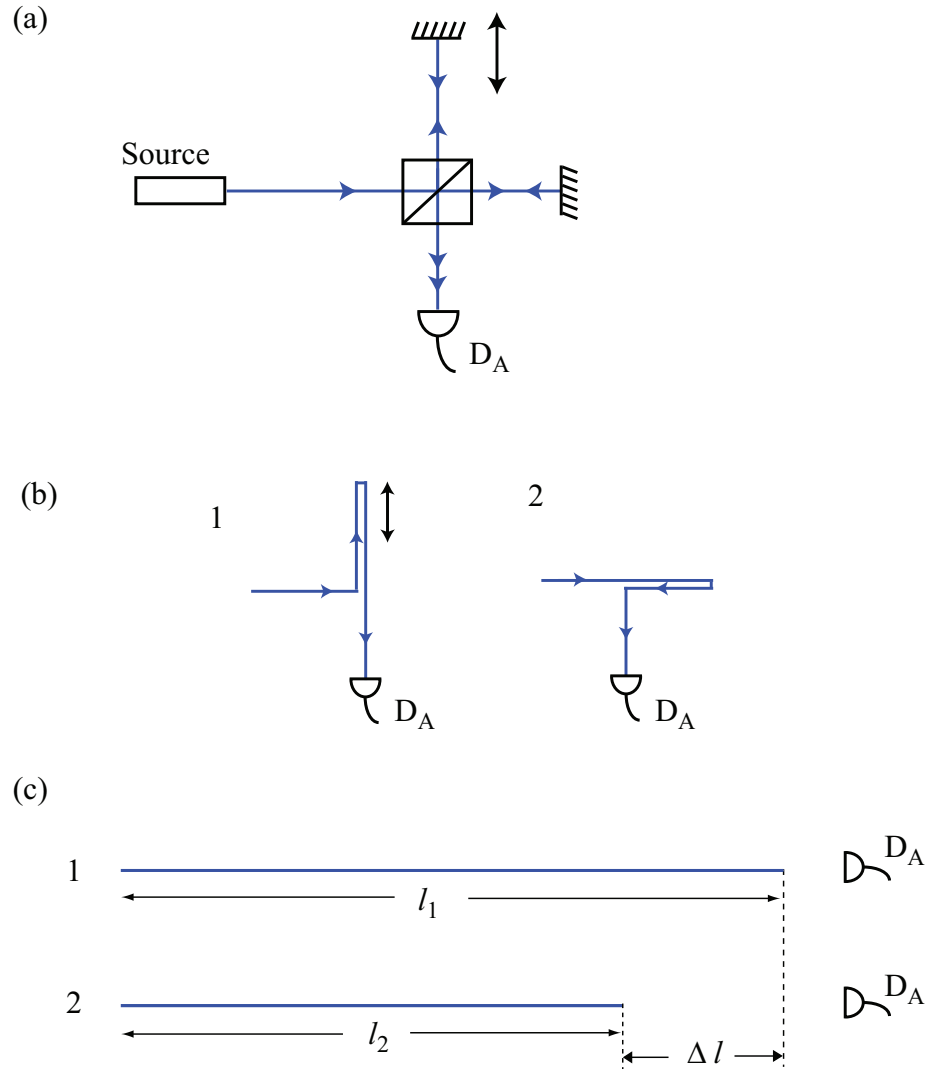


Figure 1.1: Temporal one-photon interference in a Michelson interferometer (a) Schematic of a Michelson interferometer. The source produces a quasi-monochromatic, stationary field of light. (b) 1 and 2 are the two alternative pathways by which a photon from the source reaches detector D_A . (c) Unfolded one-photon path diagrams representing the two interfering alternatives. Interference occurs because the probability amplitudes of the two alternatives must be summed. Δl is the difference between the optical path lengths l_1 and l_2 . As a function of Δl , sinusoidal interference fringes are observed in the intensity at detector D_A . The interference fringes get washed out once Δl exceeds the coherence length of the field.

single realization of the field, but the intensity averaged over an ensemble of realizations of the field. For stationary fields, ensemble averages become time-independent,

and they can therefore be replaced by the corresponding time-averages. Taking the time-average of the instantaneous intensity $I_A(t)$, we obtain the following expression for the time-averaged intensity $\langle I_A(t) \rangle_t$ at detector D_A :

$$\langle I_A(t) \rangle_t = \langle I_1(t - t_1) \rangle_t + \langle I_2(t - t_2) \rangle_t + 2\text{Re}\langle V_1^*(t - t_1)V_2(t - t_2) \rangle_t, \quad (1.3)$$

where $\langle \dots \rangle_t$ represents the time average over a period that is long compared with $1/\Delta\omega_0$, the reciprocal frequency-bandwidth of the field. Due to the stationarity of the field, the time-averaged intensities $\langle I_1(t - t_1) \rangle_t$ and $\langle I_2(t - t_2) \rangle_t$ become independent of the time arguments. Therefore, they are replaced by constant intensities: $\langle I_1(t - t_1) \rangle_t = I_1$ and $\langle I_2(t - t_2) \rangle_t = I_2$. The quantity $\langle V_1^*(t - t_1)V_2(t - t_2) \rangle_t = \Gamma(t_1, t_2)$ is the temporal coherence function of the field [2], and because of the stationarity of the field, it depends on the two time arguments only through their difference $t_1 - t_2$. The temporal coherence function $\Gamma(t_1 - t_2)$ can be written as $\Gamma(t_1 - t_2) = \sqrt{I_1 I_2} \gamma(t_1 - t_2) e^{i\omega_0(t_1 - t_2)}$, where $\gamma(t_1 - t_2)$ is the degree of temporal coherence between the two alternatives. The time-averaged intensity $\langle I_A(t) \rangle_t$ at detector D_A can then be written as

$$\langle I_A(t) \rangle_t \equiv I_A = I_1 + I_2 + 2\text{Re}\sqrt{I_1 I_2} \gamma(t_1 - t_2) e^{i\omega_0(t_1 - t_2)}, \quad (1.4)$$

Replacing $t_1 - t_2$ by $\Delta l/c$, and ω_0 by ck_0 , where k_0 is the central vacuum wave-vector magnitude of the field, we obtain the following expression for the intensity I_A at detector D_A :

$$I_A = I_1 + I_2 + 2\sqrt{I_1 I_2} \gamma(\Delta l) \cos(k_0 \Delta l). \quad (1.5)$$

The rms width of $\gamma(\Delta l)$ as a function of Δl is a measure of the coherence length of the field and is determined by the frequency bandwidth of the field. Interference is observed as a function of Δl and gets washed out once Δl exceeds the coherence length

of the field. Therefore, a necessary condition for temporal one-photon interference is that the optical path length difference Δl should be smaller than the coherence length of the field.

In Chapter 2, we develop an analogous formalism to describe temporal two-photon interference effects and obtain similar necessary conditions for coherence in two-photon interference. Although the above description using stationary fields captures all the essential features of temporal one-photon interference, there are other features that are observed only with non-stationary fields. Non-stationary fields are produced mostly by pulsed lasers. The coherence properties of the non-stationary fields are still a subject of research [39, 40, 41]. In this thesis, most of our studies are limited to stationary fields.

1.3 Spatial one-photon interference

This section reviews the concept of spatial coherence and presents a basic description of spatial one-photon interference using a Young's double-slit setup shown in Fig. 1.2(a). The source is quasi monochromatic and is, spatially, a partially coherent beam with its beam waist located at $z = 0$. The light from the source falls on the double-slit plane located at z . There are two alternative pathways—shown by the one-photon path diagrams of Fig. 1.2(b)—by which a photon from the source can reach detector D_A . In alternative 1, a photon passes through the upper slit located at transverse position x_1 , and in alternative 2, it passes through the lower slit located at transverse position x_2 . $\Delta x = x_1 - x_2$ is the separation between the two slits. The probability amplitudes of a photon to be in the two alternatives add up to produce interference effects as long as the fields in the two alternatives are coherent with each other.

To obtain the necessary condition for coherence, we evaluate the intensity, or the photon-count rate, at detector D_A located at transverse position x . The electric

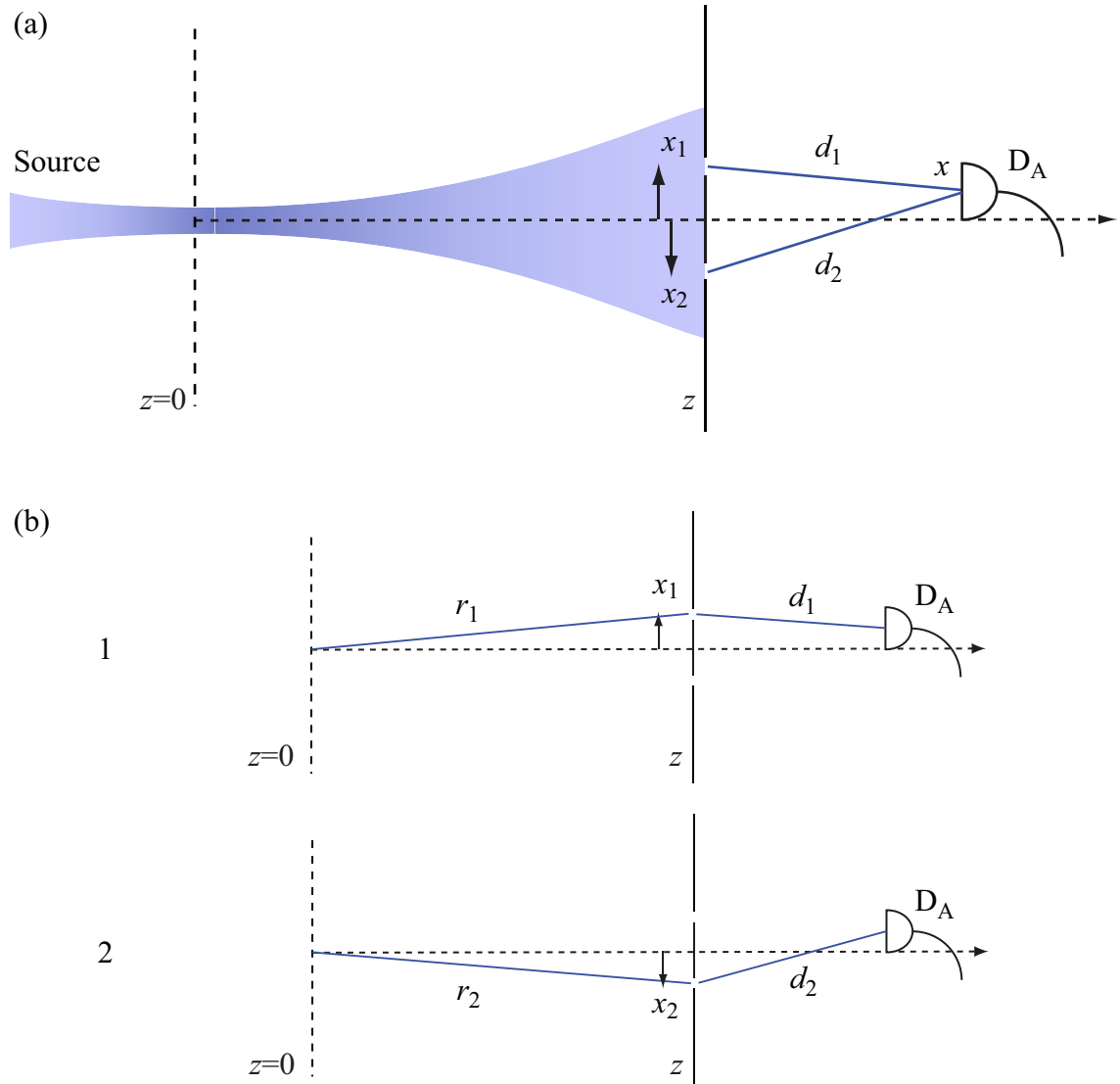


Figure 1.2: (a) Schematic representation of spatial one-photon interference in a Young's double-slit interferometer. The transverse positions of the two slits are denoted by x_1 and x_2 and their distances from the detector by d_1 and d_2 , respectively. $\Delta x = x_1 - x_2$ is the separation between the two slits. (b) Path diagrams representing alternative pathways 1 and 2 by which a photon from the source can reach detector D_A ; r_1 and r_2 are the distances from the center of the source beam at plane $z = 0$ to slits 1 and 2, respectively.

field amplitude $V_A(x)$ at detector D_A is the sum of the field amplitudes reaching the detector from transverse positions x_1 and x_2 . Thus, $V_A(x)$ can be written as

$$V_A(x) = k_1 V(x_1, z) e^{ik_0 d_1} + k_2 V(x_2, z) e^{ik_0 d_2}, \quad (1.6)$$

where k_0 is the vacuum wave-vector magnitude of the field, d_1 and d_2 are the distances of the two slits from detector D_A , and $V(x_1, z)$ and $V(x_2, z)$ are the field amplitudes at positions (x_1, z) and (x_2, z) , respectively. The factors k_1 and k_2 depend on the size of the slits and on the geometry of the arrangement. The intensity $I_A(x)$ at detector D_A is calculated by taking the ensemble average $\langle \dots \rangle_e$ of $V_A^*(x)V_A(x)$ over the different realizations of the source field. Taking the ensemble average, we obtain

$$\begin{aligned} \langle V_A^*(x)V_A(x) \rangle_e \equiv I_A(x) &= k_1^2 S(x_1, z) + k_2^2 S(x_2, z) \\ &+ k_1 k_2 W(x_1, x_2, z) e^{-ik_0(d_1-d_2)} + \text{c.c.} \end{aligned} \quad (1.7)$$

where $S(x_1, z) \equiv \langle V^*(x_1, z)V(x_1, z) \rangle_e$ and $S(x_2, z) \equiv \langle V^*(x_2, z)V(x_2, z) \rangle_e$ are the spectral densities in alternatives 1 and 2, respectively, and where $W(x_1, x_2, z) \equiv \langle V^*(x_1, z)V(x_2, z) \rangle_e$ is the cross-spectral density of the field at plane z . We assume that the field could be modelled as a Gaussian Schell-model beam (see [30], section 5.6.); the cross-spectral density $W(x_1, x_2, z)$ can then be written as

$$W(x_1, x_2, z) = \sqrt{S(x_1, z)S(x_2, z)} \mu(\Delta x, z) e^{-ik_0(r_1-r_2)}, \quad (1.8)$$

where r_1 and r_2 are the distances from the center of the beam at $z = 0$ to slits 1 and 2, respectively; $\mu(\Delta x, z)$ is the degree of spatial coherence of the field at x_1 and x_2 . The width of $\mu(\Delta x, z)$ as a function of Δx is a measure of the transverse coherence length of the field at the double-slit plane. The intensity $I_A(x)$ at detector D_A can

now be written as

$$I_A(x) = k_1^2 S(x_1, z) + k_2^2 S(x_2, z) + 2k_1 k_2 \sqrt{S(x_1, z)S(x_2, z)} \mu(\Delta x, z) \cos(k_0 \Delta l), \quad (1.9)$$

where we have substituted $l_1 = r_1 + d_1$, $l_2 = r_2 + d_2$ and $\Delta l = l_1 - l_2$. Thus, a necessary condition for interference is that the slit separation Δx should be smaller than the transverse coherence length of the field. The transverse coherence length of the field at plane z depends on the spatial coherence properties of the source at $z = 0$ [30]. In Chapter 3, we develop an analogous description of spatial interference effects with the entangled two-photon field.

Spatial coherence properties of fields produced by various primary and secondary sources have been studied by Wolf [30, 42, 43]. A general treatment of the spatial coherence properties of the Gaussian Schell-model beams is given in Sec. 5.6 of Ref. [30].

1.4 Angular one-photon interference

It is known that angular position and its conjugate variable, orbital angular momentum (OAM), form Fourier pairs [44, 45, 46]. In the case of a photon field, the Fourier relationship can be represented as

$$\psi_l = \frac{1}{\sqrt{2\pi}} \int_{-\pi}^{\pi} d\phi \Psi(\phi) \exp(-il\phi); \quad (1.10)$$

$$\Psi(\phi) = \frac{1}{\sqrt{2\pi}} \sum_{l=-\infty}^{+\infty} \psi_l \exp(il\phi). \quad (1.11)$$

Here ψ_l is the probability amplitude that the photon field is carrying orbital angular momentum $l\hbar$, while $\Psi(\phi)$ is the probability amplitude that the angular position of the photon is ϕ . Here we are representing the orbital angular momentum of a photon in a basis consisting of Laguerre-Gaussian (LG) modes, with azimuthal phase given

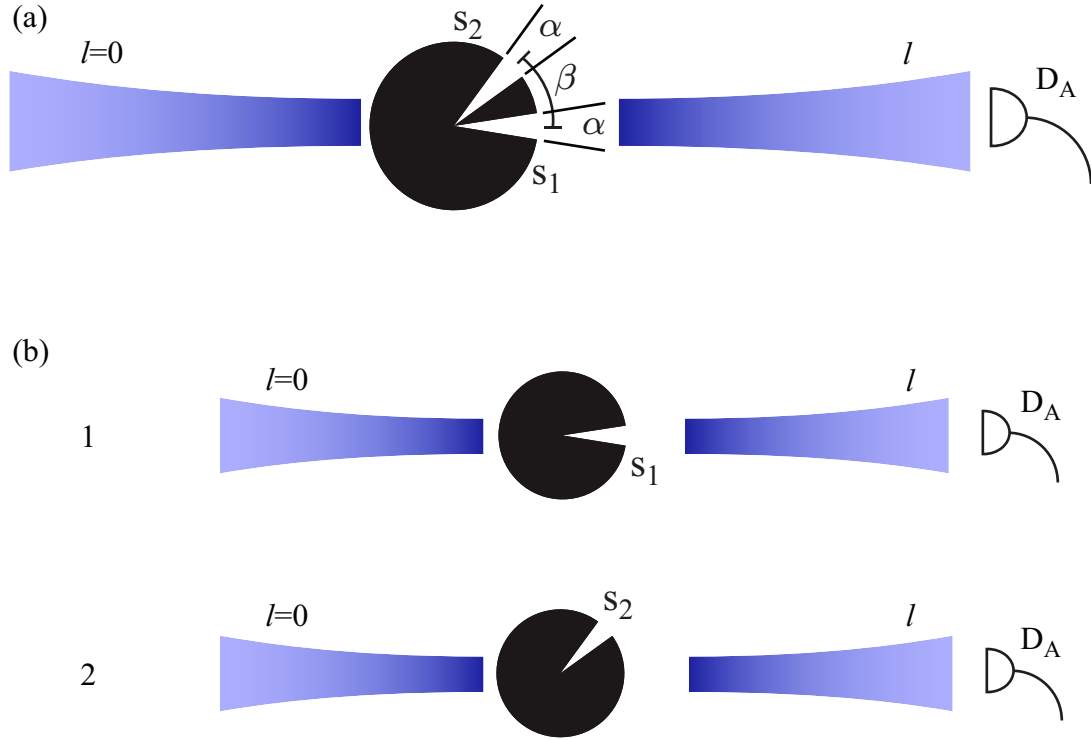


Figure 1.3: (a) Schematic representation of angular one-photon interference. A Gaussian pump field ($l = 0$) falls on an angular aperture in the form of a double angular-slit. The angular width of each slit is α , and the angular separation between the slits is β . The OAM-mode distribution of the field after the aperture is obtained using detector D_A , which is an OAM-mode selector. (b) 1 and 2 are the two alternative pathways by which a photon can pass through the angular-slits and get detected at detector D_A . The probability amplitudes in the two alternatives add up to produce angular interference.

by $e^{-il\phi}$ [47, 48]. Laguerre-Gaussian modes are characterized by index l ; a photon in an OAM-mode of order l carries an orbital angular momentum equal to $l\hbar$ [48] (see Section 4.2 for a detailed description of LG beams). The existence of such a Fourier relationship gives rise to interesting interference effects in the distribution of the OAM modes of a photon field when it passes through an angular aperture [49, 50].

We describe angular interference with one-photon fields using the setup shown in Fig. 1.3(a). A Gaussian beam ($l = 0$) falls on a double angular-slit. The angular width of each slit is α and the angular separation between the two slits is β . Detector D_A is an OAM-mode selector; it selects out different OAM-modes and measures their

intensities. In the scheme of Fig. 1.3(a), there are two alternative pathways—shown in Fig. 1.3(b)—by which a photon can pass through the slits and reach detector D_A . In alternative 1, a photon passes through the slit labelled s_1 , and in alternative 2, it passes through the slit labelled s_2 . The probability amplitudes of a photon to be in these two alternatives add up to produce interference in the distribution of the OAM modes of the photon. The probability amplitude ψ_{1l} that in alternative 1 a photon is in an OAM-mode l is given by:

$$\psi_{1l} = \frac{1}{\sqrt{2\pi}} \int_{-\pi}^{\pi} d\phi \Psi_1(\phi) e^{-il\phi}, \quad (1.12)$$

where $\Psi_1(\phi)$ is the amplitude transmission function of the aperture in alternative 1; $\Psi_1(\phi)$ is equal to unity for $-\alpha/2 < \phi < \alpha/2$ and to zero, otherwise. Substituting for $\Psi_1(\phi)$, we obtain

$$\psi_{1l} = \frac{\alpha}{\sqrt{2\pi}} \text{sinc} \left(\frac{l\alpha}{2} \right). \quad (1.13)$$

In a similar manner, we calculate the probability amplitude ψ_{2l} in alternative 2. The probability amplitude ψ_{2l} differs from the probability amplitude ψ_{1l} by only an exponential factor: $\psi_{2l} = \psi_{1l} e^{-il\beta}$. The total probability amplitude ψ_l that a photon is in an OAM mode l at detector D_A is now given by

$$\psi_l = \frac{\alpha}{\sqrt{2\pi}} \text{sinc} \left(\frac{l\alpha}{2} \right) [1 + e^{-il\beta}]. \quad (1.14)$$

The intensity I_A in mode l at detector D_A thus becomes

$$I_A = C |\psi_l|^2 = C \frac{\alpha^2}{\pi} \text{sinc}^2 \left(\frac{l\alpha}{2} \right) [1 + \cos(l\beta)], \quad (1.15)$$

where C is some constant. The intensity I_A shows sinusoidal interference fringes as a function of the angular separation β and the OAM-mode index l . The sinc-envelope is due to the diffraction from the individual angular-slits.

Angular interference effects have been observed in several experiments, thus verifying the angular Fourier relationship [45, 49, 50]. In Chapter 4, we study angular interference effects with the entangled two-photon field produced by parametric down-conversion.

1.5 Basics of nonlinear optics

When an atom is placed in an external electric field, the electrons in the atom experience a force due to this field. The electrons, which are bound in the Coulomb field of the nucleus, also experience a restoring force by the nucleus. As a result of these two competing forces, the electrons get displaced from their equilibrium positions and the atom acquires a net dipole moment. The dipole moment per unit volume which is called the polarization depends on the strength of the applied electric field.

In the case of linear optics, that is, when the applied field strength is small, the restoring force exerted on the electron is proportional to its displacement from the equilibrium position, and the atom is modelled as a harmonic oscillator. The induced polarization $P(\mathbf{r}, t)$ at position \mathbf{r} and time t depends linearly on the applied field strength $E(\mathbf{r}, t)$ and is given by [33]

$$P(\mathbf{r}, t) = \epsilon_0 \chi^{(1)} E(\mathbf{r}, t) \quad (1.16)$$

where $\chi^{(1)}$ is the linear susceptibility and ϵ_0 is the permittivity of the free space.

In the case of nonlinear optics, that is, when the applied field strength is strong, the restoring force exerted on the electron is no longer proportional to its displacement from the equilibrium position. As a result, the simple linear dependence of the induced polarization on the applied electric field is no longer valid [51]. The induced polarization $P(\mathbf{r}, t)$ gets contributions that are not only linear in electric field

strength, but also bilinear, trilinear, etc, and is given by [33]

$$P(\mathbf{r}, t) = \epsilon_0 \chi^{(1)} E(\mathbf{r}, t) + \epsilon_0 \chi^{(2)} E^2(\mathbf{r}, t) + \epsilon_0 \chi^{(3)} E^3(\mathbf{r}, t) + \dots \quad (1.17)$$

where $\chi^{(2)}$ and $\chi^{(3)}$ are known as the second-order and third-order nonlinear optical susceptibilities, respectively. $P^{(2)}(\mathbf{r}, t) = \epsilon_0 \chi^{(2)} E^2(\mathbf{r}, t)$ is the second-order nonlinear polarization. The second-order nonlinear polarization can occur only in crystals that are non-centrosymmetric, that is, in crystals that have no inversion symmetry. The contribution $P^{(2)}(\mathbf{r}, t)$ to the energy $H(t)$ of the electromagnetic field is given by [52, 53]

$$H(t) = \frac{1}{2} \int_{\mathcal{V}} d^3\mathbf{r} P^{(2)}(\mathbf{r}, t) \cdot E(\mathbf{r}, t), \quad (1.18)$$

where the integration extends over the volume \mathcal{V} of the nonlinear medium. In the next section, we study a specific example of second-order nonlinear optical process.

1.6 Two-photon field produced by parametric down-conversion

Parametric down-conversion is one of the most important second-order nonlinear process, in which a photon of higher frequency interacts with a non-centrosymmetric crystal and breaks up into two separate photons of lower frequencies. The photon of higher frequency is called the pump photon and the photons of lower frequencies are called the signal photon and the idler photon. The word parametric refers to processes in which the initial and final quantum-mechanical states of the system are identical, as opposed to non-parametric processes in which the final state of the system is different from its initial state due to the transfer of population from one real level to another [33]. In a parametric process photon energy is always conserved and the process can always be described by a real susceptibility. In contrast, in a

non-parametric process photon energy need not be conserved and the process needs to be described by a complex susceptibility. Parametric down-conversion in a nonlinear crystal was first investigated theoretically by Klyshko [54] and experimentally by Burnham and Weinberg [55], who showed that the down-converted signal and idler photons appear simultaneously within the resolving time of the detectors and the associated electronics. For the early work on parametric amplification and down-conversion, see Refs. [52, 56, 57]. The energy level diagram and the schematic of parametric down-conversion in a nonlinear crystal is depicted in Fig. 1.4.

The contribution to the energy of the electromagnetic field due to a second-order nonlinear interaction is given by the general expression in Eq. (1.18). In the case of parametric down-conversion, this contribution to the energy takes the following form:

$$H(t) = \frac{\epsilon_0}{2} \int_{\mathcal{V}} d^3\mathbf{r} \chi^{(2)} E_p(\mathbf{r}, t) E_s(\mathbf{r}, t) E_i(\mathbf{r}, t), \quad (1.19)$$

where p , s and i stand for the pump, signal and idler, respectively, $E(\mathbf{r}, t)$ is the electric field inside the nonlinear crystal at position \mathbf{r} and time t , and \mathcal{V} is the volume of the interacting part of the nonlinear crystal.

When the field is quantized, $E(\mathbf{r}, t)$ becomes a Hilbert space operator $\hat{E}(\mathbf{r}, t)$, which can be decomposed into its positive-frequency and negative-frequency parts, $\hat{E}^{(+)}(\mathbf{r}, t)$ and $\hat{E}^{(-)}(\mathbf{r}, t)$, respectively. The quantized electric fields can be written in terms of the plane-wave mode expansion of the form [53]

$$\hat{E}^{(+)}(\mathbf{r}, t) = \sum_{\mathbf{k}} i \left[\frac{\hbar \omega_{\mathbf{k}}}{2\epsilon_0 L^3} \right]^{1/2} \hat{a}_{\mathbf{k}}(t) e^{i(\mathbf{k} \cdot \mathbf{r} - \omega t)} \quad (1.20)$$

where L^3 is the quantization volume and $\hat{a}_{\mathbf{k}}(t)$ the photon annihilation operator for the mode \mathbf{k} at frequency $\omega_{\mathbf{k}}$. We write the energy contribution $H(t)$ of Eq. (1.19) in terms of the quantized fields, by expressing the pump, signal and idler fields in terms of their positive- and negative-frequency components. The resulting expression for the energy contribution $H(t)$ is then the interaction Hamiltonian $\hat{H}(t)$ for

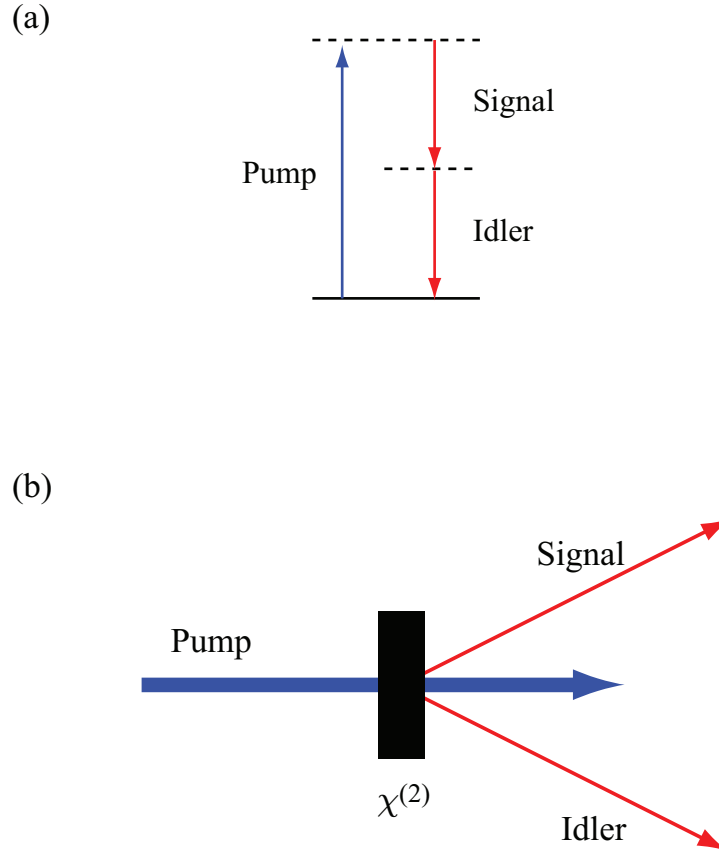


Figure 1.4: Nonlinear optical process of parametric down-conversion. (a) Energy-level diagrams describing parametric down-conversion. The solid line represents a real energy level, whereas the dashed lines represent virtual energy levels. In parametric down-conversion, a pump photon of higher frequency gets destroyed and two photons of lower frequencies known as the signal photon and the idler photon get produced. (b) Schematic of down-conversion in a second-order nonlinear crystal. Most of the pump photons pass through the crystal without interacting with it. One in about 10^8 pump photon interacts with the crystal and gets down-converted.

the process of parametric down-conversion. It is a sum of eight different terms with all possible combinations of the three fields. However, there are only two terms, $E_p^{(+)} E_s^{(-)} E_i^{(-)}$ and $E_p^{(-)} E_s^{(+)} E_i^{(+)}$, that lead to energy conserving processes and thus contribute appreciably to the down-conversion process. The contributions due to the other six terms, such as $E_p^{(-)} E_s^{(-)} E_i^{(-)}$ and $E_p^{(+)} E_s^{(+)} E_i^{(+)}$, get averaged out when the interaction Hamiltonian $\hat{H}(t)$ is integrated over time. Therefore, we neglect the contributions due to these other terms; neglecting these contributions is equivalent to

making the rotating-wave approximation as in the case of treating atomic absorption and emission processes (see Ref. [58], Section 2.3). We note that these approximations hold only for second-order processes and that for the higher-order processes the non-energy-conserving terms may lead to important contributions. The effective interaction Hamiltonian for the process of parametric down-conversion can then be given by the following simplified form:

$$\hat{H}(t) = \frac{\epsilon_0}{2} \int_{\mathcal{V}} d^3\mathbf{r} \chi^{(2)} \hat{E}_p^{(+)}(\mathbf{r}, t) \hat{E}_s^{(-)}(\mathbf{r}, t) \hat{E}_i^{(-)}(\mathbf{r}, t) + \text{H.c.} \quad (1.21)$$

This Hamiltonian is used in chapter 2 and 3 to derive the quantum-mechanical state of the two-photon field produced by parametric down-conversion.

The constraints of energy and momentum conservation in down-conversion require that the sum of the energies of the signal and idler photons be equal to the energy of the pump photon and that the sum of the momenta of the signal and idler photons be equal to the momentum of the pump photon. These constraints due to conservation laws render the two photons entangled in their time-energy, position-momentum, and angular-position–OAM degrees of freedom.

The phase-matching conditions in PDC can be adjusted so that both photons come out in a direction collinear with the pump, in which case it is known as the collinear phase-matching. Alternatively, the two photons come out in two separate directions, in which case it is known as the non-collinear phase-matching. Phase-matching conditions can also be adjusted so that the polarizations of the two photons are the same (type-I down-conversion) or orthogonal to each other (type-II down-conversion).

1.7 Quantum entanglement and EPR paradox

In 1935 A. Einstein, B. Podolsky, and N. Rosen recognized a spooky feature in the quantum description of physical reality [17]. This feature, now known as entangle-

ment, was originally called by Schrödinger “Verschränkung,” which implies the existence of global states of a composite system that cannot be described as a product of the states of the individual subsystems [59]. For an extensive review of the subject of quantum entanglement, see the article by Horodecki *et al.* [60].

According to Einstein, Podolsky and Rosen (EPR) [17]: “In a complete theory there is an element corresponding to each element of reality. A sufficient condition for the reality of a physical quantity is the possibility of predicting it with certainty, without disturbing the system. In quantum mechanics in the case of two physical quantities described by non-commuting operators, the knowledge of one precludes the knowledge of the other. Then either (1) the description of reality given by the wave function in quantum mechanics is not complete or (2) these two quantities cannot have simultaneous reality. Consideration of the problem of making predictions concerning a system on the basis of measurements made on another system that had previously interacted with it leads to the result that if (1) is false then (2) is also false. One is thus led to conclude that the description of reality as given by a wave function is not complete.”

Here Einstein, Podolsky and Rosen were explicitly considering a system of two entangled particles, which had once interacted in the past but had no interactions thereafter. They showed that in such a system, by measuring either the position or the momentum of one of the particles, either the position or the momentum of the other particle can be predicted with complete certainty without in any way disturbing the other particle. But, since position and momentum are non-commuting observables, they cannot be measured simultaneously and thus cannot be regarded as simultaneous elements of reality of a system. So they concluded that in entangled two-particles systems, the reality of position and momentum of the second system depend upon the process of measurement carried out on the first system, which does not disturb the second system in any way. On noting this apparent non-locality in the quantum theory, Einstein, Podolsky and Rosen argued that the quantum-mechanical

description of physical reality is not complete and that it should be supplemented by postulating the existence of “hidden variables,” the specifications of which will predetermine the result of measuring any observable of the system. EPR’s inherent belief was that the predictions of quantum mechanics are correct but only as a consequence of the statistical distribution of hidden variables.

A “hidden variable” interpretation of quantum mechanics was formally constructed by David Bohm in 1950s [23, 24]. Bohm believed that hidden variable theories lead to precisely the same results for all physical processes as does the quantum theory, while providing a precise and continuous description of all physical processes. For quite some time, there was no conclusive way to test the validity of these two theories. Then in 1964 John S. Bell came up with his inequalities, an experimental violation of which would rule out any local hidden variable interpretations of quantum mechanics [18].

1.8 Bell inequalities and beyond

In 1964 John S. Bell proposed a decisive test to check whether the local hidden variable interpretations of quantum mechanics were compatible with the statistical predictions of quantum mechanics or not [18]. Bell formalized EPR’s idea of a deterministic world in terms of the local hidden variable models. He showed that for a single particle system local hidden variable models produce all the results correctly; however, in the case of a system consisting of two particles, the hidden variable models do not correctly predict all the results, which are predicted correctly by quantum mechanics. He then constructed an inequality and proved that the quantum-mechanical correlations could violate his inequality, but the correlations based on hidden variable models must satisfy it. Bell further showed that for the suggested hidden variable models [23, 24] to violate Bell’s inequality, they have to be non-local and would have to involve faster than light propagation as well. In his own words, “in a hidden variable theory

in which parameters are added to quantum mechanics to determine the results of individual measurements, without changing the statistical predictions, there must be a mechanism whereby the setting of one measuring device can influence the reading of another instrument, however remote. Moreover, the signal involved must propagate instantaneously, so that such a theory could not be Lorentz invariant [18].” A popular description of the concepts of non-locality and Bell’s inequality has been presented by Kwiat and Hardy [61, 62].

In their proposed form, Bell’s inequalities were not particularly suitable for experiments. Clauser, Horne, Shimony and Holt (CHSH) generalized Bell’s inequality so that it could be applied to realizable experiments [63]. The first experiment attempting to show a violation of Bell inequalities was carried out by Kocher and Commins [15]. Later, using the generalized CHSH-Bell inequalities, Freedman and Clauser reported an improved experiment providing strong evidence against the local hidden variable theories [16]. However, the first convincing test of the violations of Bell inequalities was performed by Aspect *et al.* [19, 20], using correlated photons produced in atomic cascade. Since then, using entangled pair of photons produced by parametric down-conversion, violations of the CHSH forms of Bell’s inequality have been observed for various degrees of freedom including polarization [64, 65], phase and momentum [21], time and energy [7, 8, 9], spatial-parity [66], frequency [67] and OAM [68]. Using hyperentangled states, even simultaneous violations of Bell inequalities for more than one degrees of freedom have been reported [69, 70, 71, 72]. More recently, Bell inequalities have been constructed even for bipartite quantum systems of arbitrarily high dimensionality [73]. The first demonstration of a high-dimensional Bell inequality was reported by Vaziri *et al.* [22], who showed a violation in three dimensions by more than 18 standard deviations. The results of these experiments have strongly confirmed the predictions of quantum mechanics and have provided very strong evidence against the local hidden variable interpretations of quantum mechanics.

Until mid 1990s, studies related to Bell's inequality and entanglement were mostly centered at probing the foundations of quantum mechanics. However, in recent years entanglement is beginning to be seen as a resource that could also be used for many useful applications. Some of these proposed applications include quantum cryptography [25], quantum dense coding [26] quantum teleportation [27], entanglement swapping [28] and quantum lithography [29].

With the increase in the number of applications based on quantum entanglement, quantifying the amount of entanglement in a system has become a very fundamental question in quantum information theory. Several different measures to quantify the amount of entanglement of a bipartite (two party) system have been proposed, including relative entropy of entanglement [74], Schmidt number [75], concurrence [76, 77] and negativity [78]. Although there are a few entanglement measures for multipartite pure state system [79], quantifying entanglement in multipartite mixed state system is still an open problem. In this thesis, we use one of the bipartite entanglement measure, namely, concurrence, in Chapter 3 and 4.

1.9 Two-photon coherence and two-photon entanglement

The physics of one-photon interference, discussed in Sections 1.2 through 1.4, is understood in terms of the famous statement of Dirac that a photon interferes only with itself [80]. Interference occurs as long as the different one-photon alternatives are indistinguishable, that is, as long as the one-photon fields in different interfering alternatives are coherent with each other. The coherence properties of one-photon fields can be described in terms of either the classical coherence functions [2] or their quantum counterpart [31, 32]. The physics of two-photon interference, which forms the subject matter of this thesis, is understood similarly in terms of a two-photon interfering with itself [1, 6, 81]. Two-photon interference occurs as long as the differ-

ent two-photon alternatives are indistinguishable, that is, as long as the two-photon fields in different interfering alternatives are coherent with each other. The coherence properties of two-photon fields can be completely described in terms of only the quantum-mechanical correlation functions [31, 32].

As pointed out in section 1.6, the “two-photon” nature of the down-converted field is due to the entanglement of the two photons. It is then evident that two-photon coherence and two-photon entanglement are interrelated concepts. Two-photon entanglement in a given degree of freedom implies two-photon coherence in the corresponding domain. Two-photon interference experiments are, therefore, used as tools to verify, explore and quantify two-photon entanglement. In the next three chapters, we study the coherence properties of the entangled two-photon field in the temporal, spatial and angular domains, and we establish some general connections between two-photon coherence and two-photon entanglement.

1.10 Summary

In this chapter, we have reviewed the basics of one-photon interference in the temporal, spatial and angular domains. We have discussed the nonlinear optical process of parametric down-conversion, which is a process that produces entangled two-photon fields. We have also discussed some of the key concepts related to quantum entanglement. In the next three chapters, we present our studies of the coherence properties of the entangled two-photon field produced by parametric down-conversion. In Chapter 2, we study the temporal coherence properties of the entangled two-photon field and present a new formalism for describing temporal two-photon interference effects. We also describe our work related to exploring time-energy entanglement using geometric phases of the entangled photons. In Chapter 3, we study the effects of the spatial coherence properties of the pump field on the spatial coherence properties of the down-converted two-photon field. We establish certain general connections be-

tween the degree of two-photon coherence and the degree of entanglement of spatial two-qubit states. In Chapter 4, two-photon interference effects in the angular domain are studied. By utilizing the angular-position correlations of the down-converted photons, we describe a new method for preparing entangled two-qubit states. Chapter 5 presents the general conclusions.

Chapter 2

Two-Photon Coherence Effects: Temporal

2.1 Introduction

In the past few decades, much attention has been devoted to studying the temporal two-photon interference effects involving the signal and idler photons produced by parametric down-conversion (PDC) [1, 3, 4, 5, 6, 7, 8, 9, 10, 82, 83]. The Hong-Ou-Mandel (HOM) effect [3], two-photon fringes in the Franson interferometer [7, 8, 9], induced coherence without induced emission [4], frustrated two-photon creation [5] and postponed compensation [6] are some of the very interesting temporal two-photon interference effects observed among many others.

In this chapter, we study the temporal coherence properties of the entangled two-photon field in a general two-photon interference scheme. The description of temporal two-photon interference experiment with the photons produced by PDC involves six different length parameters, which are the path lengths traveled by the pump, signal and idler photons in two interfering alternatives. Using these six different length parameters, we construct two separate length parameters—called the two-photon path-length difference and the two-photon path-asymmetry-length difference. In terms of

the two constructed parameters, we present a description of temporal two-photon interference, in situations in which the frequency bandwidth of the pump field is much narrower than that of the down-converted signal and idler fields.

This chapter is organized as follows. In Section 2.2, the derivation of the two-photon state produced by parametric down-conversion is reviewed. Sections 2.3 through 2.6 present a description of temporal two-photon interference in terms of the two length parameters constructed in Section 2.3. In Section 2.7, we report a two-photon interference experiment in which the effects due to the variations of the two length parameters can be independently studied. Sections 2.8 and 2.9 contain brief discussions related to time-energy entanglement and Bell inequality for time and energy, respectively. In Section 2.10, we report our experimental work demonstrating that the time-energy entanglement of the down-converted signal and idler photons can be explored by means of their geometric phases. Section 2.11 presents the summary.

2.2 Two-photon state produced by parametric down-conversion

Figure 2.1 depicts the process of parametric down-conversion. At time $t' = -t_{\text{int}}$, a pump photon starts interacting with the nonlinear crystal. The interaction persists until time $t' = 0$ during which the pump photon can get absorbed by the crystal and down-convert into two separate photons, called the signal photon and the idler photon. In Chapter 1, the basic physics behind the nonlinear optical process of parametric down-conversion was described in detail and an expression for the interaction Hamiltonian was derived under certain approximations [Eq. (1.21)]. Substituting t' for t in Eq. (1.21), we write the interaction Hamiltonian $\hat{H}(t')$ as [84, 85]

$$\hat{H}(t') = \frac{\epsilon_0}{2} \int_{\mathcal{V}} d^3\mathbf{r} \chi^{(2)} \hat{E}_p^{(+)}(\mathbf{r}, t') \hat{E}_s^{(-)}(\mathbf{r}, t') \hat{E}_i^{(-)}(\mathbf{r}, t') + \text{H.c.} \quad (2.1)$$

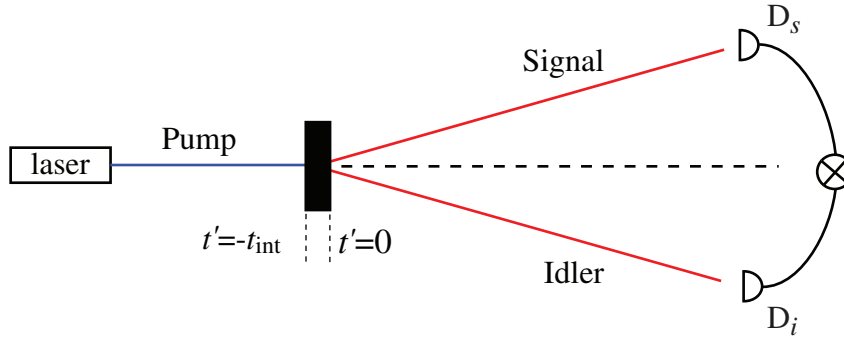


Figure 2.1: Producing two-photon field by parametric down-conversion. The pump photon starts interacting with the nonlinear crystal at time $t' = -t_{\text{int}}$. The interaction persists until $t' = 0$ during which a pump photon can down-convert into signal and idler photons. The measurements on the two-photon field are carried by detecting the signal and idler photons in coincidence.

Here \mathcal{V} is the volume of the interacting part of the nonlinear crystal and $\chi^{(2)}$ is the second-order nonlinear susceptibility. $\hat{E}_j^{(+)}(\mathbf{r}, t')$ and $\hat{E}_j^{(-)}(\mathbf{r}, t')$ are the positive- and negative-frequency parts of the electric field, where $j = p, s$ and i stand for the pump, signal and idler, respectively. In order to avoid complexities associated with refractions of signal and idler modes at the dielectric-air interface, we assume that the nonlinear crystal is embedded in a passive linear medium of suitable refractive index [53, 86].

We now derive the state of the two-photon field produced by PDC. The general form of the interaction Hamiltonian will be used in Chapter 3, where we shall derive the two-photon state for the most general case. In the present chapter, since we are considering only the temporal coherence effects, we shall use a simplified form of the interaction Hamiltonian of Eq. (2.2). We assume the transverse area of the interacting part of the nonlinear crystal to be very large. We also assume that the emission directions of the signal and idler fields are fixed such that the transverse wave-vectors of the pump field (\mathbf{q}_p) is equal to the sum of the transverse wave-vectors of the signal (\mathbf{q}_s) and idler (\mathbf{q}_i) fields, that is, $\mathbf{q}_p = \mathbf{q}_s + \mathbf{q}_i$, where $\mathbf{k}_p \equiv (\mathbf{q}_p, k_{pz})$, $\mathbf{k}_s \equiv (\mathbf{q}_s, k_{sz})$ and $\mathbf{k}_i \equiv (\mathbf{q}_i, k_{iz})$ are the wave-vectors of the pump, signal and idler

fields, respectively. In a two-photon interference experiment, perfect phase-matching for the transverse wave-vectors is usually ensured by placing pin-holes in the signal and idler photon paths. With the above assumptions, the interaction Hamiltonian $\hat{H}(t')$ for parametric down-conversion takes the following form:

$$\hat{H}(t') = \frac{\epsilon_0}{2} \int_{-L}^0 dz \chi^{(2)} \hat{E}_p^{(+)}(z, t') \hat{E}_s^{(-)}(z, t') \hat{E}_i^{(-)}(z, t') + \text{H.c.}, \quad (2.2)$$

where L is the thickness of the nonlinear crystal. The three electric fields are given as

$$\hat{E}_p^{(+)}(z, t') = \int_0^\infty A_p d\omega_p V(\omega_p) e^{i[k_{pz}(\omega_p)z - \omega_p t']} e^{i(\omega_p \tau_p + \phi_p)}, \quad (2.3)$$

$$\hat{E}_s^{(-)}(z, t') = \int_0^\infty A_s^* d\omega_s \hat{a}_s^\dagger(\omega_s) e^{i[\omega_s t' - k_{sz}(\omega_s)z]}, \quad (2.4)$$

$$\hat{E}_i^{(-)}(z, t') = \int_0^\infty A_i^* d\omega_i \hat{a}_i^\dagger(\omega_i) e^{i[\omega_i t' - k_{iz}(\omega_i)z]}, \quad (2.5)$$

where k_{jz} is the z -component of wave-vector \mathbf{k}_j , with $j = p, s, i$. A_j is a frequency dependent quantity. However, it varies very slowly within the frequency range of interest for most down-conversion experiments; and therefore, it can be taken outside the integral. The pump field has been assumed to be very strong and will be treated classically. The strength of the pump field at frequency ω_p is represented by $V(\omega_p)$. τ_p represents the time taken by the pump photon in travelling the optical path length l_p between the laser and the nonlinear crystal, while ϕ_p is the phase other than the dynamical one accumulated during this travel. In writing $\hat{E}_p^{(+)}(\mathbf{r}, t')$, we have explicitly included the phase factor $e^{i(\omega_p \tau_p + \phi_p)}$. This is to take into account those interference effects in which the pump photon accumulates different phases in two interfering alternatives [4, 5, 87]. Using Eqs. (2.3), (2.4) and (2.5), we write Eq. (2.2)

as

$$\begin{aligned} \hat{H}(t') = & \frac{A_p A_s^* A_i^* \epsilon_0 \chi^{(2)}}{2} \int_{-L}^0 dz \iiint_0^\infty d\omega_p d\omega_s d\omega_i \hat{a}_s^\dagger(\omega_s) \hat{a}_i^\dagger(\omega_i) V(\omega_p) \\ & \times e^{i[k_{pz}(\omega_p) - k_{sz}(\omega_s) - k_{iz}(\omega_i)]z} e^{i(\omega_s + \omega_i - \omega_p)t'} e^{i(\omega_p \tau_p + \phi_p)} + \text{H.c.} \end{aligned} \quad (2.6)$$

The second-order nonlinear susceptibility $\chi^{(2)}$ has been assumed to be independent of frequency over the range of interest. The state of the down-converted field at time $t' = -t_{\text{int}}$ is given by $|\psi(-t_{\text{int}})\rangle = |\text{vac}\rangle_s |\text{vac}\rangle_i$, which is a vacuum state with no photons in either the signal or the idler mode. The state $|\psi(0)\rangle$ of the two-photon field at $t' = 0$ is then calculated using the Schrödinger equation to be

$$|\psi(0)\rangle = \exp\left[\frac{1}{i\hbar} \int_{-t_{\text{int}}}^0 dt' \hat{H}(t')\right] |\psi(-t_{\text{int}})\rangle. \quad (2.7)$$

The parametric interaction is assumed to be very weak so that the state in Eq. (2.7) can be approximated by the first two terms of a perturbative expansion. The first term is simply the initial vacuum state. The second term $|\psi_{\text{tp}}\rangle$ is calculated by substituting from Eq. (2.6) into Eq. (2.7) to be

$$\begin{aligned} |\psi_{\text{tp}}\rangle = & \frac{A_p A_s^* A_i^* \epsilon_0 \chi^{(2)}}{2i\hbar} \int_{-t_{\text{int}}}^0 dt' \int_{-L}^0 dz \iiint_0^\infty d\omega_p d\omega_s d\omega_i V(\omega_p) \\ & \times e^{i[k_{pz}(\omega_p) - k_{sz}(\omega_s) - k_{iz}(\omega_i)]z} e^{i(\omega_s + \omega_i - \omega_p)t'} e^{i(\omega_p \tau_p + \phi_p)} \hat{a}_s^\dagger(\omega_s) \hat{a}_i^\dagger(\omega_i) |\text{vac}\rangle_s |\text{vac}\rangle_i. \end{aligned} \quad (2.8)$$

We note that although the interaction Hamiltonian $\hat{H}(t')$ in Eq. (2.6) contains two separate terms, including the Hermitian conjugate, the two-photon state $|\psi_{\text{tp}}\rangle$ in Eq. (2.8) contains only one term. This is due to the fact that the operator $\hat{a}_s(\omega_s) \hat{a}_i(\omega_i)$ in the Hermitian conjugate term adds no contribution to the generated two-photon state when it acts on the vacuum state $|\text{vac}\rangle_s |\text{vac}\rangle_i$.

The interaction time t_{int} is taken to be much longer than the time scale over which down-conversion takes place. Therefore, both limits of the time integration

in Eq. (2.8) is extended to infinity [84, 88]. Carrying out the time integration then yields

$$|\psi_{\text{tp}}\rangle = A \int_{-L}^0 dz \iiint_0^\infty d\omega_p d\omega_s d\omega_i V(\omega_p) \delta(\omega_s + \omega_i - \omega_p) e^{i[k_{pz}(\omega_p) - k_{sz}(\omega_s) - k_{iz}(\omega_i)]z} \times e^{i(\omega_p \tau_p + \phi_p)} |\omega_s\rangle_s |\omega_i\rangle_i. \quad (2.9)$$

Here, we have absorbed all the constant factors into A . Next, we evaluate the ω_i -integral and obtain

$$|\psi_{\text{tp}}\rangle = A \int_{-L}^0 dz \iint_0^\infty d\omega_p d\omega_s V(\omega_p) \times e^{i[k_{pz}(\omega_p) - k_{sz}(\omega_s) - k_{iz}(\omega_p - \omega_s)]z} e^{i(\omega_p \tau_p + \phi_p)} |\omega_s\rangle_s |\omega_p - \omega_s\rangle_i. \quad (2.10)$$

By rearranging the above equation, we obtain the following expression for the two-photon state $|\psi_{\text{tp}}\rangle$ at the exit face of the crystal:

$$|\psi_{\text{tp}}\rangle = A \iint_0^\infty d\omega_p d\omega_s V(\omega_p) \Phi(\omega_s, \omega_p - \omega_s) e^{i(\omega_p \tau_p + \phi_p)} |\omega_s\rangle_s |\omega_p - \omega_s\rangle_i, \quad (2.11)$$

where

$$\Phi(\omega_s, \omega_p - \omega_s) = \int_{-L}^0 dz e^{i[k_{pz}(\omega_p) - k_{sz}(\omega_s) - k_{iz}(\omega_p - \omega_s)]z} \quad (2.12)$$

is called the phase-matching function. The exact form of the phase-matching function $\Phi(\omega_s, \omega_p - \omega_s)$ depends on the nonlinear crystal parameters and the type of down-conversion (type-I or type-II). Appendix A contains a detailed calculation of the phase-matching function for different types of down-conversion and crystal parameters.

2.3 Representing two-photon interference using path diagrams

In a two-photon interference experiment, the two-photon field is made to go through two alternative pathways. The fields in the two alternative pathways are then combined, and the interference is observed in the coincidence count rate of two detectors. We begin by representing a general two-photon two-alternative interference experiment by the two-photon path diagrams of Fig. 2.2. Diagrammatic approaches have previously also been used to describe two-photon interference effects (see Refs. [6, 10]). In this chapter, we consider only the polarization-independent, temporal two-photon interference effects, assuming perfect spatial coherence. We also assume that the frequency bandwidth of the pump field is much smaller than that of the signal and idler fields.

In Fig. 2.2, alternatives 1 and 2 are the two pathways by which a pump photon is down-converted and the down-converted signal and idler photons are detected in coincidence at single-photon detectors D_s and D_i . Two-photon interference is observed in the coincidence count rate of detectors D_s and D_i as long as the two alternatives are coherent, i.e., indistinguishable from each other. We adopt the convention that a signal photon is the one that reaches detector D_s and that an idler photon is the one that reaches detector D_i . In a two-photon interference experiment, these alternative pathways can be introduced by using beam splitters [3, 6], by passing the pump beam twice through a crystal [5], or even by using two different crystals [4]. In Fig. 2.2, l denotes the optical path length traveled by a photon and ϕ stands for phases other than the dynamic phase, such as the phase acquired due to reflections, geometric phase [83, 89], etc. Thus l_{s1} denotes the path length traveled by the signal photon in alternative 1, etc. For every optical path length traveled, the corresponding time elapsed is denoted by $\tau = l/c$. Thus τ_{s1} represents the time taken in traveling the distance l_{s1} . The various path-lengths and phases are used to define two length

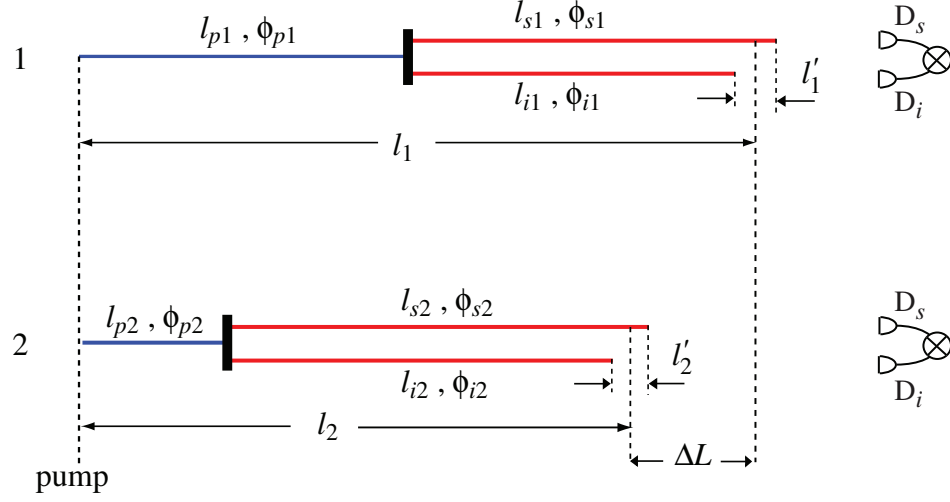


Figure 2.2: Schematic representation of temporal two-photon interference using two-photon path diagrams. Alternatives 1 and 2 are the two pathways by which a pump photon is down-converted and the down-converted signal and idler photons are detected at single-photon detectors D_s and D_i in coincidence.

parameters and one phase parameter as follows:

$$\begin{aligned}
 \Delta L &\equiv l_1 - l_2 = \left(\frac{l_{s1} + l_{i1}}{2} + l_{p1} \right) - \left(\frac{l_{s2} + l_{i2}}{2} + l_{p2} \right), \\
 \Delta L' &\equiv l'_1 - l'_2 = (l_{s1} - l_{i1}) - (l_{s2} - l_{i2}), \\
 \Delta \phi &\equiv \phi_1 - \phi_2 = (\phi_{s1} + \phi_{i1} + \phi_{p1}) - (\phi_{s2} + \phi_{i2} + \phi_{p2}). \tag{2.13}
 \end{aligned}$$

Here $l_{1(2)}$ and $l'_{1(2)}$ are the two-photon path length and the two-photon path asymmetry-length for alternative 1(2); they are also referred to as the biphoton path length and the biphoton path-asymmetry length, respectively [81]. In a particular alternative, the two-photon path length is defined to be the mean of the optical path lengths traveled by the signal and idler photons added to the optical path length traveled by the pump photon. The two-photon path-asymmetry length is defined to be the difference of the optical path lengths traveled by the signal and idler photons. ΔL is the difference of the two-photon path lengths l_1 and l_2 whereas $\Delta L'$ is the difference of the two-photon path-asymmetry lengths l'_1 and l'_2 . The corresponding times are

represented by $\Delta\tau$ and $\Delta\tau'$ respectively. Notice that if either ΔL or $\Delta L'$ is too large, alternatives 1 and 2 will become distinguishable and will no longer interfere.

2.4 Temporal two-photon interference

The two-photon state $|\psi_{\text{tp}}\rangle$ produced by down-conversion is given by Eq. (2.11). In a two-photon interference experiment, the complete two-photon state $|\psi\rangle$ is given by the coherent superposition of the two-photon states in alternatives 1 and 2, that is,

$$|\psi\rangle = |\psi_{\text{tp1}}\rangle + |\psi_{\text{tp2}}\rangle. \quad (2.14)$$

By substituting in Eq. (2.11) the relevant parameters corresponding to alternatives 1 and 2, we evaluate the two-photon states at the exit face of the crystal in the two alternatives. The complete two-photon state $|\psi\rangle$ is then given by

$$\begin{aligned} |\psi\rangle = & A \iint_0^\infty d\omega_p d\omega_s V_1(\omega_p) \Phi_1(\omega_s, \omega_p - \omega_s) e^{i(\omega_p \tau_{p1} + \phi_{p1})} |\omega_s\rangle_{s1} |\omega_p - \omega_s\rangle_{i1} \\ & + A \iint_0^\infty d\omega_p d\omega_s V_2(\omega_p) \Phi_2(\omega_s, \omega_p - \omega_s) e^{i(\omega_p \tau_{p2} + \phi_{p2})} |\omega_s\rangle_{s2} |\omega_p - \omega_s\rangle_{i2}. \end{aligned} \quad (2.15)$$

$V_{1(2)}(\omega_p)$ is the strength of the pump field at frequency ω_p in alternatives 1(2) and $\Phi_{1(2)}(\omega_s, \omega_p - \omega_s)$ is the phase-matching function in alternative 1(2). We denote the positive-frequency parts of the electric fields at detectors D_s and D_i by $\hat{E}_s^{(+)}(t)$ and $\hat{E}_i^{(+)}(t)$, respectively. The field at a detector is equal to the sum of the fields arriving at that detector by alternatives 1 and 2. Thus,

$$\begin{aligned} \hat{E}_s^{(+)}(t) &= \hat{E}_{s1}^{(+)}(t - \tau_{s1}) + \hat{E}_{s2}^{(+)}(t - \tau_{s2}), \\ \hat{E}_i^{(+)}(t) &= \hat{E}_{i1}^{(+)}(t - \tau_{i1}) + \hat{E}_{i2}^{(+)}(t - \tau_{i2}). \end{aligned} \quad (2.16)$$

Here $\hat{E}_{s1}^{(+)}(t - \tau_{s1})$ is the positive-frequency part of the field arriving at detector D_s in alternative 1, etc. The electric fields $\hat{E}_s^{(+)}(t)$ and $\hat{E}_i^{(+)}(t)$, respectively, can be written

as

$$\begin{aligned} \hat{E}_s^{(+)}(t) &= \int_0^\infty d\omega f_s(\omega - \omega_{s0}) \\ &\times [c_{s1}\hat{a}_{s1}(\omega)e^{-i[\omega(t-\tau_{s1})-\phi_{s1}]} + c_{s2}\hat{a}_{s2}(\omega)e^{-i[\omega(t-\tau_{s2})-\phi_{s2}]}] \end{aligned} \quad (2.17)$$

and

$$\begin{aligned} \hat{E}_i^{(+)}(t) &= \int_0^\infty d\omega' f_i(\omega' - \omega_{i0}) \\ &\times [c_{i1}\hat{a}_{i1}(\omega')e^{-i[\omega'(t-\tau_{i1})-\phi_{i1}]} + c_{i2}\hat{a}_{i2}(\omega')e^{-i[\omega'(t-\tau_{i2})-\phi_{i2}]}]. \end{aligned} \quad (2.18)$$

Here $f_s(\omega - \omega_{s0})$ and $f_i(\omega' - \omega_{i0})$ are the amplitude transmission functions of the filters placed before detectors D_s and D_i , respectively. The two filters are centered at frequencies ω_{s0} and ω_{i0} . It is assumed that perfect phase-matching is satisfied at frequencies ω_0 , ω_{s0} and ω_{i0} with $\omega_0 = \omega_{s0} + \omega_{i0}$. c_{s1} is the probability amplitude that the signal photon is detected in alternative 1, etc. Since all the phase information is already contained in ϕ_{s1} , etc., we take the probability amplitudes to be real quantities. The probability amplitudes are normalized such that $c_{s1}^2 + c_{s2}^2 = c_{i1}^2 + c_{i2}^2 = 1$.

The coincidence count rate $R_{si}(t, t + \tau)$, which is the probability per (unit time)² that a photon is detected at D_s at time t and another at D_i at time $t + \tau$, is given by: $R_{si}(t, t + \tau) = \alpha_s \alpha_i |\langle 0 | \hat{E}_i^{(+)}(t + \tau) \hat{E}_s^{(+)}(t) | \psi \rangle|^2$ [31], where α_s and α_i are the quantum efficiencies of detectors D_s and D_i , respectively. By substituting from Eqs. (2.15), (2.17) and (2.18), the coincidence count rate $R_{si}(t, t + \tau)$ can be shown to be

$$\begin{aligned} R_{si}(t, t + \tau) &= \alpha_s \alpha_i \left| \langle 0 | \hat{E}_i^{(+)}(t + \tau) \hat{E}_s^{(+)}(t) | \psi \rangle \right|^2 \\ &= \alpha_s \alpha_i \left| \langle 0 | \hat{E}_{i1}^{(+)}(t + \tau) \hat{E}_{s1}^{(+)}(t) | \psi \rangle + \langle 0 | \hat{E}_{i2}^{(+)}(t + \tau) \hat{E}_{s2}^{(+)}(t) | \psi \rangle \right|^2, \end{aligned} \quad (2.19)$$

where

$$\begin{aligned} \langle 0 | \hat{E}_{i1}^{(+)}(t + \tau) \hat{E}_{s1}^{(+)}(t) | \psi \rangle &= A c_1 e^{i\phi_1} \iint_0^\infty d\omega_p d\omega_s V_1(\omega_p) \Phi_1(\omega_s, \omega_p - \omega_s) \\ &\times f_s(\omega_s - \omega_{s0}) f_i(\omega_p - \omega_s - \omega_{i0}) e^{i\omega_s(\tau - \tau_{i1} + \tau_{s1})} e^{-i\omega_p(t + \tau - \tau_{i1} - \tau_{p1})}, \end{aligned} \quad (2.20)$$

and

$$\begin{aligned} \langle 0 | \hat{E}_{i2}^{(+)}(t + \tau) \hat{E}_{s2}^{(+)}(t) | \psi \rangle &= A c_2 e^{i\phi_2} \iint_0^\infty d\omega_p d\omega_s V_2(\omega_p) \Phi_2(\omega_s, \omega_p - \omega_s) \\ &\times f_s(\omega_s - \omega_{s0}) f_i(\omega_p - \omega_s - \omega_{i0}) e^{i\omega_s(\tau - \tau_{i2} + \tau_{s2})} e^{-i\omega_p(t + \tau - \tau_{i2} - \tau_{p2})}. \end{aligned} \quad (2.21)$$

Here we have substituted $c_1 = c_{s1}c_{i1}$ and $c_2 = c_{s2}c_{i2}$. The two terms inside the modulus bracket are the two-photon probability amplitudes [90] in alternatives 1 and 2, respectively.

We now evaluate the two-photon probability amplitude $\langle 0 | \hat{E}_{i1}^{(+)}(t + \tau) \hat{E}_{s1}^{(+)}(t) | \psi \rangle$ in alternative 1. We assume that the pump field $V_1(\omega_p)$ is centered around $\omega_p = \omega_0$ and has a spectral width $\Delta\omega_p$, which is small enough such that the phase-matching function and the filter functions do not change appreciably in the frequency range $(\omega_0 - \Delta\omega_p/2, \omega_0 + \Delta\omega_p/2)$. The above assumption regarding the pump spectral width remains valid for most continuous wave and pulsed lasers. However, this assumption may not remain valid for very short pulsed pump [88, 91]. Substituting ω_s by $\omega'_s + \omega_{s0}$ and replacing ω_p by its central value ω_0 in the phase-matching function, we write $\langle 0 | \hat{E}_{i1}^{(+)}(t + \tau) \hat{E}_{s1}^{(+)}(t) | \psi \rangle$ as a product of two integrals

$$\begin{aligned} \langle 0 | \hat{E}_{i1}^{(+)}(t + \tau) \hat{E}_{s1}^{(+)}(t) | \psi \rangle &= A c_1 e^{i\phi_1} e^{i\omega_d(\tau + \tau'_1)} \int_{-\omega_0/2}^\infty d\omega'_s \Phi_1(\omega'_s + \omega_{s0}, \omega_0 - \omega_{s0} - \omega'_s) \\ &\times f_s(\omega'_s) f_i(-\omega'_s) e^{i\omega'_s(\tau + \tau'_1)} \int_0^\infty d\omega_p V_1(\omega_p) e^{i\omega_0(\tau + \tau'_1)/2} e^{-i\omega_p(t + \tau - \tau_{i1} - \tau_{p1})}, \end{aligned} \quad (2.22)$$

where following substitutions have been made: $\tau_1 = (\tau_{s1} + \tau_{i1})/2 + \tau_{p1}$, $\tau'_1 = \tau_{s1} - \tau_{i1}$ and $\omega_d = (\omega_{s0} - \omega_{i0})/2$. We note that when the above assumption regarding the

pump spectral width is not valid, $\langle 0 | \hat{E}_{i1}^{(+)}(t + \tau) \hat{E}_{s1}^{(+)}(t) | \psi \rangle$ cannot be written as two separate integrals, and in that case it would have to be evaluated differently [88, 91].

Eq. (2.22) can be simplified as

$$\begin{aligned} \langle 0 | \hat{E}_{i1}^{(+)}(t + \tau) \hat{E}_{s1}^{(+)}(t) | \psi \rangle &= A c_1 e^{i\phi_1} e^{i\omega_d(\tau + \tau'_1)} \int_{-\omega_0/2}^{\infty} d\omega'_s g_1(\omega'_s) e^{i\omega'_s(\tau + \tau'_1)} \\ &\times \int_0^{\infty} d\omega_p V_1(\omega_p) e^{i\omega_0(\tau + \tau'_1)/2} e^{-i\omega_p(t + \tau - \tau_{i1} - \tau_{p1})}, \end{aligned} \quad (2.23)$$

with

$$g_1(\omega'_s) = \Phi_1(\omega'_s + \omega_{s0}, \omega_0 - \omega_{s0} - \omega'_s) f_s(\omega'_s) f_i(-\omega'_s) \quad (2.24)$$

being the amplitude of the effective signal-idler field at the displaced frequency ω'_s . We refer to the spectral width $\Delta\omega$ of function $g(\omega'_s)$ as the frequency bandwidth of the signal-idler field; the spectral width of the phase-matching function $\Phi_1(\omega'_s + \omega_{s0}, \omega_0 - \omega_{s0} - \omega'_s)$ which depends on the nonlinear-crystal parameters will be referred to as the down-conversion frequency bandwidth. The signal-idler frequency bandwidth $\Delta\omega$ depends on the frequency bandwidths of both the phase-matching function and the filters functions, and it is usually much smaller than the central frequency ω_{s0} . Therefore, we extend the lower limit of the ω'_s integral to $-\infty$. Next, we substitute $\omega'_p = \omega_p - \omega_0$ in Eq. (2.23), and assuming the spectral width $\Delta\omega_p$ of the pump field to be much smaller than its central frequency ω_0 , we write Eq. (2.23) as

$$\begin{aligned} \langle 0 | \hat{E}_{i1}^{(+)}(t + \tau) \hat{E}_{s1}^{(+)}(t) | \psi \rangle &= \\ &A c_1 e^{i\phi_1} e^{i\omega_d(\tau + \tau'_1)} e^{-i\omega_0(t + \tau/2 - \tau_1)} g_1^*(\tau + \tau'_1) v_1(t + \tau - \tau_1 + \tau'_1/2), \end{aligned} \quad (2.25)$$

where

$$g_1^*(\tau) \equiv \int_{-\infty}^{\infty} d\omega'_s g_1(\omega'_s) e^{i\omega'_s \tau} \quad \text{and} \quad (2.26)$$

$$v_1(t) \equiv \int_{-\infty}^{\infty} d\omega'_p V_1(\omega'_p + \omega_0) e^{-i\omega'_p t}. \quad (2.27)$$

A similar expression for the two-photon probability amplitude $\langle 0 | \hat{E}_{i2}^{(+)}(t+\tau) \hat{E}_{s2}^{(+)}(t) | \psi \rangle$ in alternative 2 is obtained. Eq. (2.19) is now written as

$$R_{si}(t, t + \tau) = K \left| c_1 g_1^*(\tau + \tau'_1) v_1(t + \tau - \tau_1 + \tau'_1/2) e^{i(\omega_0 \tau_1 + \omega_d \tau'_1 + \phi_1)} + c_2 g_2^*(\tau + \tau'_2) v_2(t + \tau - \tau_2 + \tau'_2/2) e^{i(\omega_0 \tau_2 + \omega_d \tau'_2 + \phi_2)} \right|^2, \quad (2.28)$$

where $K = |A|^2 \alpha_s \alpha_i$ is a constant. $R_{si}(t, t + \tau)$ is the expression for the coincidence count rate in a two-alternative, temporal two-photon interference. Eq. (2.28) can be easily generalized to take into account those situations in which the signal and idler photons arrive at the two detectors by more than two alternative pathways, or even by an infinite number of alternative pathways. In the latter situation, a single sum in Eq. (2.28) will be replaced by an integral.

2.5 Time-averaged coincidence count rate

In most experiments, one does not measure the coincidence count rate of Eq. (2.28). Instead, one measures the coincidence count rate averaged with respect to t over the photon collection time T_{collect} and with respect to τ over the coincidence time-window T_{coinc} . We now calculate the time-averaged coincidence count rate from the coincidence count rate given in Eq. (2.28). Substituting $\tau_1 - \tau_2 = \Delta\tau$, $\tau'_1 - \tau'_2 = \Delta\tau'$

and $\phi_1 - \phi_2 = \Delta\phi$, we rewrite Eq. (2.28) as

$$\begin{aligned}
R_{si}(t, t + \tau) = & \\
& K \left[|c_1 g_1(\tau + \tau'_1) v_1(t + \tau - \tau_1 + \tau'_1/2)|^2 + |c_2 g_2(\tau + \tau'_2) v_2(t + \tau - \tau_2 + \tau'_2/2)|^2 \right. \\
& + c_1 c_2 g_1^*(\tau + \tau'_1) g_2(\tau + \tau'_2) v_1(t + \tau - \tau_1 + \tau'_1/2) v_2^*(t + \tau - \tau_2 + \tau'_2/2) \\
& \left. \times e^{i(\omega_0 \Delta\tau + \omega_d \Delta\tau' + \Delta\phi)} + \text{c.c.} \right]. \quad (2.29)
\end{aligned}$$

In a two-photon interference experiment, the photon collection time T_{collect} is usually a few seconds whereas the reciprocal of the pump spectral width $1/\Delta\omega_p$ for a typical laboratory laser source is usually a few microseconds or smaller. Thus T_{collect} is always much longer than $1/\Delta\omega_p$, and if in addition $T_{\text{collect}} \gg |\tau - \tau_1 + \tau'_1/2|$, $|\tau - \tau_2 + \tau'_2/2|$, the t -averaged pump intensities become independent of time arguments:

$$\left\langle |v_1(t + \tau - \tau_1 + \tau'_1/2)|^2 \right\rangle_t = |v_1|^2, \quad \left\langle |v_2(t + \tau - \tau_2 + \tau'_2/2)|^2 \right\rangle_t = |v_2|^2. \quad (2.30)$$

Thus the time-averaging in Eq. (2.29) with respect to t over the photon collection time T_{collect} yields

$$\begin{aligned}
R_{si}(\tau) = & \langle R_{si}(t, t + \tau) \rangle_t \\
= & K \left[|c_1 g_1(\tau + \tau'_1) v_1|^2 + |c_2 g_2(\tau + \tau'_2) v_2|^2 + c_1 c_2 g_1^*(\tau + \tau'_1) g_2(\tau + \tau'_2) \right. \\
& \left. \times \langle v_1(t - \tau_1 + \tau'_1/2) v_2^*(t - \tau_2 + \tau'_2/2) \rangle_t e^{i(\omega_0 \Delta\tau + \omega_d \Delta\tau' + \Delta\phi)} + \text{c.c.} \right]. \quad (2.31)
\end{aligned}$$

The coincidence time window T_{coinc} in a two-photon interference experiment is usually a few nanoseconds whereas the reciprocal of the signal-idler frequency bandwidth, $1/\Delta\omega$, is typically a few picoseconds or smaller [3, 90]. Thus T_{coinc} is always much longer than $1/\Delta\omega$. If in addition $T_{\text{coinc}} \gg \tau'_1, \tau'_2$, we get: $\langle |g_1(\tau + \tau'_1)|^2 \rangle_\tau = |g_1|^2$ and $\langle |g_2(\tau + \tau'_2)|^2 \rangle_\tau = |g_2|^2$. We now take the time average of Eq. (2.31) with respect to

τ over the coincidence time window T_{coin} , which yields

$$R_{si} = \langle R_{si}(\tau) \rangle_{\tau} = K \left[|c_1 g_1 v_1|^2 + |c_2 g_2 v_2|^2 + c_1 c_2 \langle g_1^*(\tau + \tau'_1) g_2(\tau + \tau'_2) \rangle_{\tau} \right. \\ \left. \times \langle v_1(t - \tau_1 + \tau'_1/2) v_2^*(t - \tau_2 + \tau'_2/2) \rangle_t e^{i(\omega_0 \Delta\tau + \omega_d \Delta\tau' + \Delta\phi)} + \text{c.c.} \right]. \quad (2.32)$$

In what follows, we take the pump field to be a stationary, continuous-wave field. The time-averaged pump correlation function $\langle v_1(t - \tau_1 + \tau'_1/2) v_2^*(t - \tau_2 + \tau'_2/2) \rangle_t$ is then a real function and depends on the two time arguments only through their difference. With the assumption of the stationarity of the pump field, the time-averaged pump correlation function can be written as

$$\langle v_1(t - \tau_1 + \tau'_1/2) v_2^*(t - \tau_2 + \tau'_2/2) \rangle_t = \sqrt{|v_1|^2 |v_2|^2} \gamma(\Delta L - \Delta L'/2), \quad (2.33)$$

where $\gamma(\Delta L - \Delta L'/2)$ is the time-averaged degree of correlations of the pump field. In writing Eq. (2.33), we have used the definitions of Eq. (2.13): $\Delta L = c\Delta\tau = c(\tau_1 - \tau_2)$ and $\Delta L' = c\Delta\tau' = c(\tau'_1 - \tau'_2)$. As we show in Appendix A, for most phase-matching conditions, the time-averaged signal-idler correlation function $\langle g_1^*(\tau + \tau'_1) g_2(\tau + \tau'_2) \rangle_{\tau}$ is a real function and depends on the two time arguments only through their difference. The time-averaged signal-idler correlation function can be written as (see Appendix A for details.)

$$\langle g_1^*(\tau + \tau'_1) g_2(\tau + \tau'_2) \rangle_{\tau} = \sqrt{|g_1|^2 |g_2|^2} \gamma'(\Delta L'), \quad (2.34)$$

where $\Delta L' = c\Delta\tau' = c(\tau'_1 - \tau'_2)$, and where $\gamma'(\Delta L')$ is the time-averaged degree of correlation of the signal-idler field. Eq. (2.32) can now be written in a much simplified form by noting that c_1 and c_2 are real numbers. Substituting from Eqs. (2.33) and (2.34) into Eq. (2.32), we obtain the following expression for the time-averaged

coincidence count rate R_{si} :

$$R_{si} = R_1 + R_2 + 2\sqrt{R_1 R_2} \gamma'(\Delta L') \gamma(\Delta L - \Delta L'/2) \cos(k_0 \Delta L + k_d \Delta L' + \Delta \phi), \quad (2.35)$$

where $k_0 = \omega_0/c$ and $k_d = \omega_d/c$, and where

$$R_1 = K |c_1 g_1 v_1|^2 \quad \text{and} \quad (2.36)$$

$$R_2 = K |c_2 g_2 v_2|^2 \quad (2.37)$$

are the coincidence count rates when coincidences are collected from only alternatives 1 and 2, respectively. The frequency bandwidth $\Delta\omega$ of the signal-idler field was assumed to be much broader than the frequency bandwidth $\Delta\omega_p$ of the pump field. Therefore, we approximate the product of the two correlation functions $\gamma'(\Delta L') \gamma(\Delta L - \Delta L'/2)$ as $\gamma'(\Delta L') \gamma(\Delta L)$ and write Eq. (2.35) as

$$R_{si} = R_1 + R_2 + 2\sqrt{R_1 R_2} \gamma'(\Delta L') \gamma(\Delta L) \cos(k_0 \Delta L + k_d \Delta L' + \Delta \phi), \quad (2.38)$$

The product $\gamma'(\Delta L') \gamma(\Delta L)$ is the time-averaged degree of two-photon correlation. In an interference experiment, two-photon fringes are observed only so long as the product $\gamma'(\Delta L') \gamma(\Delta L)$ is greater than zero. Two-photon interference gets washed out once either of the two correlation function becomes much smaller than unity. From the expression for the coincidence count rate R_{si} , it follows that two-photon interference effects in the temporal domain can be completely described in terms of the variations of the two length parameters, ΔL and $\Delta L'$. In the special case, when the down-converted fields are degenerate, that is $k_d = 0$, and $R_1 = R_2 = C$, the expression for the coincidence count rate reduces to

$$R_{si} = C[1 + \gamma'(\Delta L') \gamma(\Delta L) \cos(k_0 \Delta L + \Delta \phi)]. \quad (2.39)$$

In what follows we use this simplified expression for the coincidence count rate.

Part of the analysis presented so far in this chapter has been reported in Ref. [81]. In the formalism presented here, we have taken the pump field to be a stationary field. In a separate work, we have extended this formalism to also study the effects due to a non-stationary pump field [92].

In the next section, we analyze the time-averaged correlation functions for some simple cases. In the section following that, we report an experiment in which the effects due to the variations of the two length parameters can be independently controlled and studied.

2.6 The two correlation functions

The time-averaged degree of correlations of the pump and the signal-idler fields depend on the spectrum of the pump and the signal-idler fields, respectively. For the special case when the pump is a stationary (continuous-wave) field having a Gaussian spectrum of rms frequency width $\Delta\omega_p$, the time-averaged degree of correlation of the pump field can be evaluated using the generalized Wiener-Kintchine theorem (see Ref. [2], Chapter 3) to be

$$\gamma(\Delta L) = \exp\left[-\frac{1}{2}\left(\frac{\Delta L}{l_{\text{coh}}^p}\right)^2\right]. \quad (2.40)$$

Here $l_{\text{coh}}^p = c/\Delta\omega_p$ is the coherence length of the pump field. In Appendix A, we evaluate the time-averaged degree of correlation $\gamma'(\Delta L')$ of the signal-idler field for various phase-matching conditions. In situations in which the signal-idler field has a Gaussian spectrum of width $\Delta\omega$, the time-averaged degree of correlation of the signal-idler field can be written as

$$\gamma'(\Delta L') = \exp\left[-\frac{1}{2}\left(\frac{\Delta L'}{l_{\text{coh}}}\right)^2\right], \quad (2.41)$$

where $l_{\text{coh}} = c/\Delta\omega$ is the rms width of $\gamma'(\Delta L')$ as a function of $\Delta L'$ and is a measure of the reciprocal bandwidth of the signal-idler field. It is also taken quite often as a measure of the coherence length of the signal-idler field [3, 6, 81]. However, we note that this is strictly true only when the signal-idler field is completely stationary.

We now look at the effects of varying ΔL and $\Delta L'$ on the coincidence count rate R_{si} of Eq. (2.39) by considering two limiting cases.

Case I: For $\Delta L' = 0$ and $\Delta\phi = 0$,

$$R_{si} = C [1 + \gamma(\Delta L) \cos(k_0\Delta L)]. \quad (2.42)$$

Interference is observed in the coincidence count rate as ΔL is varied and gets washed out once ΔL exceeds the pump coherence length. Thus ΔL plays the same role in two-photon interference as does the optical path-length difference in one-photon interference. It is because of this analogy that we call ΔL the two-photon path-length difference [see Eq. (1.5) in Chapter 1 for comparison]. The coincidence fringes seen in Franson-type interferometers [8, 9] and in the double-pass setup [5] are examples of effects due to variations in ΔL .

Case II: For ΔL and $\Delta\phi$ fixed,

$$R_{si} = C [1 + K\gamma'(\Delta L')], \quad (2.43)$$

where $K = \gamma(\Delta L) \cos(k_0\Delta L + \Delta\phi)$ is constant. The coincidence count rate can show a dip when the two alternatives interfere destructively ($K < 0$), and a hump when the two alternatives interfere constructively ($K > 0$), as $\Delta L'$ is varied. These profiles, with widths equal to l_{coh} , represent how the coherence between two two-photon alternatives changes with a variation in $\Delta L'$. $\Delta L'$ has no one-photon counterpart. Effects observed in the HOM experiment [3], and in the postponed compensation experiment [6] are examples of two-photon interference effects due to variations in $\Delta L'$. In the HOM experiment [3], the effect was seen with $\Delta L = 0$, whereas in the postponed

compensation experiment [6], the effects were seen in the limit $l_{\text{coh}} \ll \Delta L \ll l_{\text{coh}}^p$.

2.7 Two-photon coherence and the HOM effect

As illustrated in Fig. 2.3(a), in the Hong-Ou-Mandel (HOM) experiment [3], the signal and idler photons from PDC are mixed at a beam splitter and the two-photon interference effect is observed in the coincidence count rate of detectors D_s and D_i , as a function of the beam splitter position x . The experiment can be understood in terms of the two-photon path diagrams shown in Fig. 2.3(b). In alternative 1, both the signal and idler photons get reflected by the beam splitter, while in alternative 2, they both get transmitted by the beam splitter. Using the two-photon path diagrams, we find that $\Delta L = 0$, $\Delta L' = 4x \cos \theta$, and $\Delta \phi = \pi$. The coincidence count rate R_{si} is then calculated using Eq. (2.39) to be

$$R_{si} = C[1 - \gamma'(4x \cos \theta)] \quad (2.44)$$

At $x = 0$, that is, at the balanced position of the beam splitter, the coincidence count rate R_{si} is equal to zero. This implies that at the balanced position of the beam splitter, both photons always leave through the same output port of the beam splitter. As a result, a null is observed in the coincidence count rate at the balanced position, leading to a dip in the coincidence count rate as a function of the beam splitter position x . An intuitive explanation of this effect can be given in terms of the bunching of signal and idler photons at a beam splitter [93]. However, the bunching interpretation is not adequate for the postponed compensation [6] and related experiments [10] in which HOM-like effects are observed, even when signal and idler photons do not simultaneously arrive at a beam splitter. As discussed in the previous section, both HOM and HOM-like effects are consequences of how temporal two-photon coherence changes as a function of the two-photon path-asymmetry-length difference $\Delta L'$.

The HOM and HOM-like experiments [3, 6, 10] required mixing of signal and idler

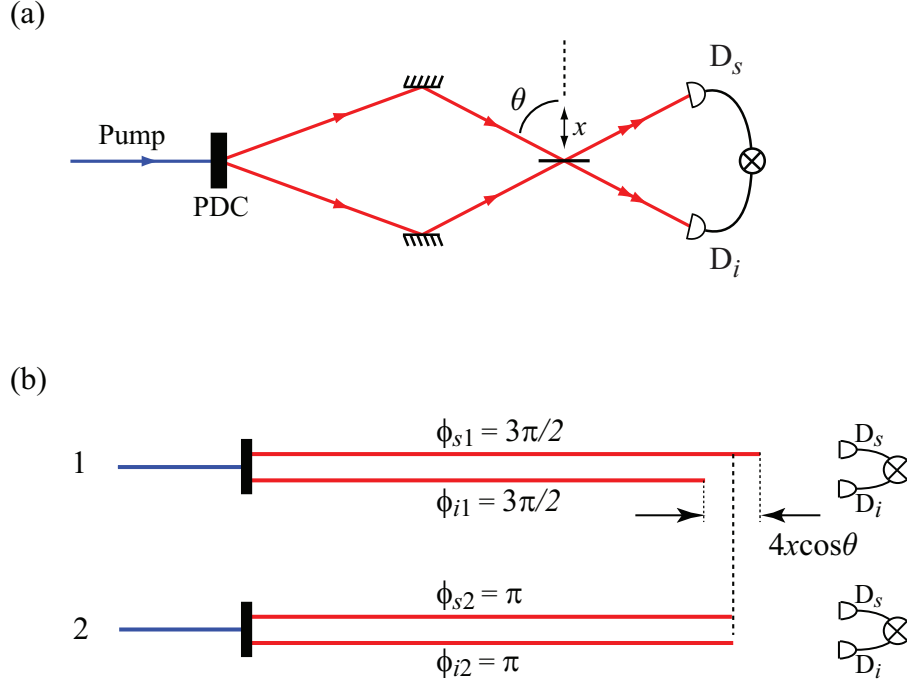


Figure 2.3: (a) Schematic of the Hong-Ou-Mandel (HOM) experiment. (b) Two-photon path diagrams illustrating two-photon interference in a HOM experiment. In alternative 1, both the signal and idler photons get reflected by the beam splitter, while in alternative 2, they both get transmitted.

photons at a beam splitter. In contrast, we next report our experimental observations of changes in two-photon coherence as a function of $\Delta L'$, in a double pass setup (shown in Fig. 2.4), which does not involve mixing of signal and idler photons at a beam splitter. A similar setup was used earlier to demonstrate the frustrated two-photon creation [5]. In this setup, there are many ways in which ΔL and $\Delta L'$ could be varied either independently or simultaneously, by displacing the signal (M_s), idler (M_i) and the pump (M_p) mirrors. In our experiments we change only the signal and idler mirror positions.

In the balanced position of the setup of Fig. 2.4(a), the distances of the signal, idler and the pump mirrors from the crystal remain equal. We denote the displacements of the signal and idler mirrors from the balanced position by x_s and x_i respectively. Using the two-photon path diagrams of Fig. 2.4(b), we find that $\Delta L = x_s + x_i$,

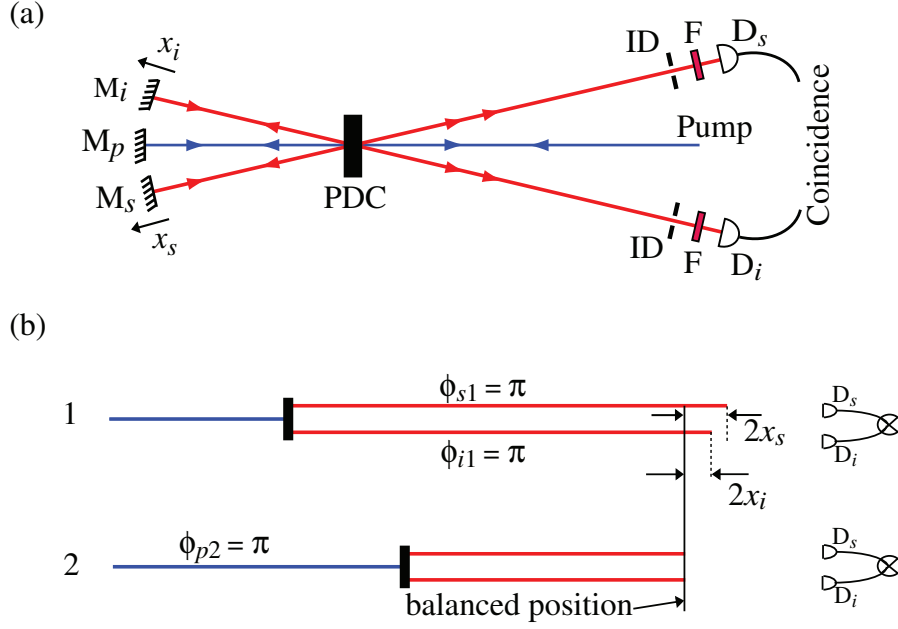


Figure 2.4: (a) Schematic of the experimental setup. (b) Two-photon path diagrams. In alternative 1, the pump photon gets downconverted in the forward pass while in alternative 2, it gets downconverted in the backward pass. F is an interference filter with 10-nm bandwidth, centered at 727.6 nm; ID is an iris diaphragm.

$\Delta L' = 2x_s - 2x_i$ and $\Delta\phi = \pi$. Assuming ΔL to be always much smaller than the pump coherence length l_{coh}^p , which in our experiment is about 5 cm, we calculate the coincidence count rate R_{si} for detectors D_s and D_i using Eq. (2.39) to be

$$R_{si} = C\{1 - \gamma'(2x_s - 2x_i) \cos[k_0(x_s + x_i)]\}. \quad (2.45)$$

A displacement of either the signal or idler mirror changes both ΔL and $\Delta L'$; therefore, the coincidence count rate R_{si} will show fringes as a function of the idler mirror position. However, equal displacements of the signal and idler mirrors in opposite directions change $\Delta L'$ while keeping ΔL ($= x_s + x_i$) fixed; and therefore, the coincidence count rate R_{si} will show either a dip or a hump as a function of the joint displacement, depending on the fixed value of ΔL .

Figure 2.5 shows the results of our experimental investigations. A cw Ar-ion laser

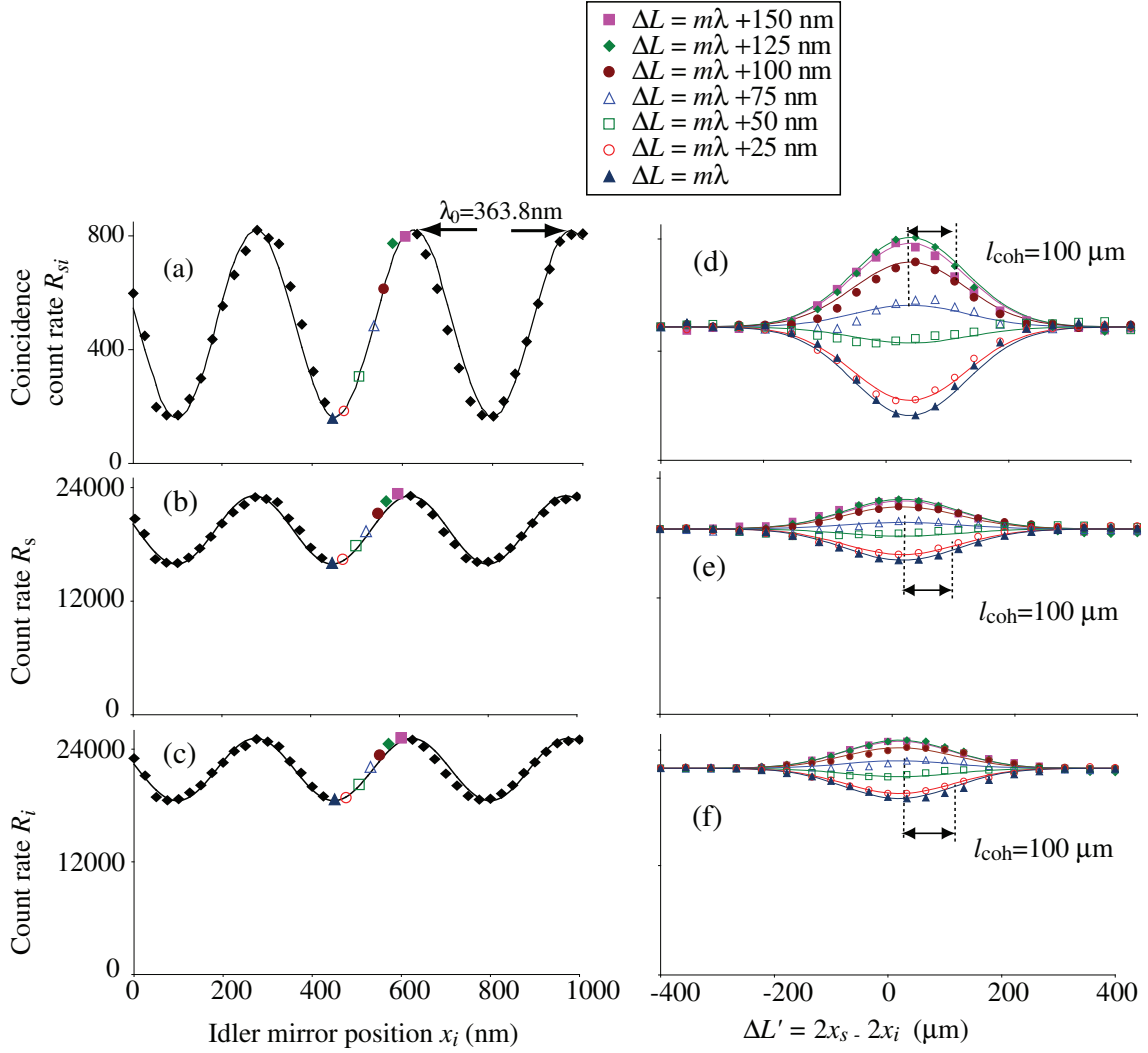


Figure 2.5: Measured (a) coincidence count rate R_{si} , (b) count rate R_s and (c) count rate R_i as a function of the idler mirror position. Measured (d) coincidence count rate R_{si} , (e) count rate R_s and (f) count rate R_i , as a function of $\Delta L'$ for various fixed values of ΔL . Solid lines are the theoretical best fits.

operating at $\lambda_0 = 363.8$ nm was used as a pump to produce degenerate type-I PDC. The signal and idler photons were collected into multimode fibers and detected using two avalanche photodiodes. The distance between the crystal and each detector was about 1.2 m. With the diaphragms set to a size of about 1.2 mm, the effective bandwidth of the signal-idler field becomes 0.85 nm, resulting in a coherence length

l_{coh} of about $100 \mu\text{m}$.

The idler mirror was first scanned around the balanced position and as a result fringes were observed in the coincidence count rate R_{si} [Fig. 2.5(a)]. Next, the idler mirror was placed at different fixed positions corresponding to different values of ΔL , as shown in Fig. 2.5(a) and in the inset, where m is an integer. Starting from each idler mirror position, the signal and idler mirrors were displaced equally in opposite directions. Dip and hump profiles of width $100 \mu\text{m}$ were observed in the coincidence count rate R_{si} [Fig. 2.5(d)].

In addition, profiles similar to that of the coincidence count rate were also observed in the single photon count rates R_s and R_i . As a function of the idler mirror position, fringes were observed in count rates of R_s [Fig. 2.5(b)] and R_i [Fig. 2.5(c)]; and as a function of the simultaneous displacements of the signal and idler mirrors, dip and hump profiles of width $100 \mu\text{m}$ were observed in count rates R_s [Fig. 2.5(e)] and R_i [Fig. 2.5(f)].

These one-photon effects cannot be described by second-order (in the field) coherence theory [2] because the one-photon path-length differences involved in these experiments are much longer than the coherence lengths of the one-photon fields. Interference effects in one photon count rates have previously also been observed in many two-photon experiments including induced coherence [4], frustrated two-photon creation [5] and interference experiment from separate pulses [82]. Although these one-photon effects have been interpreted differently, they can all be described entirely in terms of the sum of two-photon interference profiles. Thus, we represent the one-photon count rate R_X at a detection position X as the sum of the coincidence count rates R_{XY_i} between X and all the other positions Y_i where the twin of the photon detected at X can go, i.e.,

$$R_X = \sum_i R_{XY_i}, \quad (2.46)$$

Summing over the detector positions R_{Y_i} in Eq. (2.46) is same as taking the partial trace over all the possible modes of the twin. The summation turns into an integral

whenever the twin has finite probabilities of arriving at a continuous set of detection points. A detailed description of the induced coherence experiment [4] based on Eq. (2.46) is worked out in Appendix B.

Now, for the setup in Fig. 2.4, the twin of a photon detected at D_s can go only to D_i and vice versa. Therefore, using Eq. (2.46) we find that the one-photon count rates R_s and R_i are each equal to the coincidence count rate R_{si} . Hence, as a function of either ΔL or $\Delta L'$, the one-photon count rates show profiles similar to that of the coincidence count rate.

The dip-hump visibilities for R_{si} , R_s and R_i were found to be 67%, 18% and 15%, respectively. The overall interference visibilities are low due to imperfect mode matching of the fields in the two alternatives. The visibilities of one-photon count rates are much smaller than that of the coincidence count rate, because of the limited detection efficiency of the system, which affects the one-photon count rate more strongly than the coincidence count rate. Less than perfect experimental fits are due to the uncontrollable drifts of translation stages.

We see that both in this experiment, and in the HOM [3] and HOM-like [6, 10] experiments the same effect, that is, the change in two-photon coherence as a function of the two-photon path-asymmetry-length difference, is observed. However, in our experiment—in contrast to the earlier experiments—this effect is observed in a setup that does not involve mixing of signal and idler photons at a beam splitter. Moreover, to the best of our knowledge, we have observed for the first time that the changes in two-photon coherence can manifest itself in the count rates of individual detectors as dip and hump profiles. These results were reported in Ref. [81].

2.8 Time-energy entanglement

Two-photon coherence and two-photon entanglement are interrelated concepts. Two-photon coherence in the temporal domain implies entanglement in the time-energy

degree of freedom of the two photons. In the next three sections, we discuss the time-energy entanglement of the down-converted two-photon fields. The precise meaning of time-energy entanglement can be understood in terms of an EPR-type argument [17], which is that by measuring either the arrival-time or the energy of one of the two photon, either the arrival-time or the energy, respectively, of the other photon can be inferred, in principle, with complete certainty [94]. The existence of such simultaneous correlations in both time and energy is what is meant by time-energy entanglement. The implication of this interpretation is that for conditional measurements the non-commuting observables time and energy could be known with more certainty than is allowed by the uncertainty principle.

Time-energy entanglement is verified through a violation of the Bell inequality for time and energy, proposed by J. D. Franson [7]. The experimental verification of time-energy entanglement through a Bell-violation was first attempted by Brendel *et al.* [9]; however, it was Kwiat *et al.* [8] who demonstrated an unambiguous violation [8]. The feasibility of using time-energy entanglement for quantum communication was suggested by Brendel *et al.*, using a novel interferometric scheme [95]. Generalizing this scheme, Thew *et al.* have recently realized time-energy entangled qutrits that could be utilized in quantum communication based architectures [96].

2.9 Bell inequality for time and energy

In 1989, a Bell inequality for time and energy was suggested by J. D. Franson using an experimental scheme commonly known as the Franson interferometer [7]. Franson's scheme for violating a Bell inequality requires changing the phases of the signal and idler photons in one of the interfering alternatives. A Franson interferometer is depicted in Fig. 2.6(a). In this interferometer, there are, in principle, four alternative pathways by which signal and idler photons can pass through the interferometer and get detected at detector D_s and D_i in coincidence. Two of the alternative pathways

are shown in Fig. 2.6(b). In alternative 1, both the signal and idler photons pass through the long arms of the interferometer, while in alternative 2, they pass through the short arms. The other two alternative pathways are: (i) the signal photon passes through the long arm of the interferometer and the idler through the short arm; (ii) the signal photon passes through the short arm of the interferometer and the idler through the long arm. Franson's scheme relies on the assumption that these two other alternatives can be filtered out through the detection process. In experiments, this is accomplished by making sure that the coincidence detection-window is much shorter than the travel-time difference between the long and the short arms. However, this inherent post-selection in Franson's scheme allows for the local hidden variable interpretations of correlations observed in the Franson interferometer [97]. A scheme to avoid this problem was demonstrated by Strekalov *et al.* [69], who reported a post-selection free violation using pair of photons that were entangled in both the time-energy and polarization degrees of freedom. Recently, Cabello *et al.* have proposed a modified Franson interferometer that does not suffer from the above mentioned problem [98].

We now describe Franson's original scheme, using the setup shown in Fig. 2.6(a). In Fig. 2.6(a), Φ_s and Φ_i are the total extra phases acquired by the signal and idler photons, respectively, in the long arms compared to the phases acquired in the short arms. The complete two-photon state $|\psi_{\text{tp}}\rangle$ is the coherent sum of the two-photon states in alternatives 1 and 2, and it can be written as

$$|\psi_{\text{tp}}\rangle = |\psi_{\text{tp}}\rangle_1 + e^{-i(\Phi_s + \Phi_i)} |\psi_{\text{tp}}\rangle_2. \quad (2.47)$$

Here $|\psi_{\text{tp}}\rangle_{1(2)}$ is the two-photon state in alternative 1(2). We assume that ΔL and $\Delta L'$ in the setup are much smaller than the coherence lengths of the pump and the signal-idler fields, respectively. Using Eq. (2.39), we calculate the coincidence count

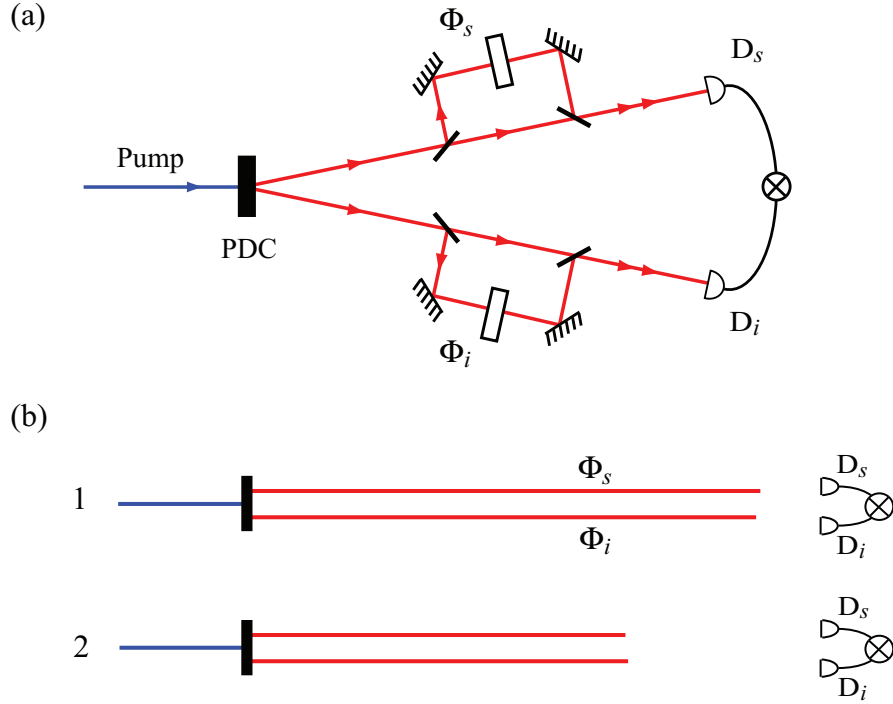


Figure 2.6: (a) The Franson interferometer for violating Bell inequality for time-energy. (b) 1 and 2 are the two alternative pathways by which the signal and idler photons can reach the two detectors. In alternative 1, both the signal and idler photons pass through the long arms of the interferometer, while in alternative 2, they pass through the short arms.

rate R_{si} of detectors D_s and D_i to be

$$R_{si} = C[1 + \cos(\Phi_s + \Phi_i)] \quad (2.48)$$

The quantum-mechanical correlation of the above equation leads to a violation of a Clauser-Horne-Shimony-Holt (CHSH)-Bell inequality [63]. According to the CHSH-bell inequality, the Bell parameter $|S|$ is always less than or equal to 2 for a local hidden variable theory, where, in this case,

$$S = E(\Phi_s, \Phi_i) + E(\Phi'_s, \Phi_i) + E(\Phi_s, \Phi'_i) - E(\Phi'_s, \Phi'_i) \quad (2.49)$$

and $E(\Phi_s, \Phi_i)$ is given by [99]

$$E(\Phi_s, \Phi_i) = \frac{R(\Phi_s, \Phi_i) + R(\Phi_s^\perp, \Phi_i^\perp) + R(\Phi_s, \Phi_i^\perp) - R(\Phi_s^\perp, \Phi_i)}{R(\Phi_s, \Phi_i) + R(\Phi_s^\perp, \Phi_i^\perp) + R(\Phi_s, \Phi_i^\perp) + R(\Phi_s^\perp, \Phi_i)}. \quad (2.50)$$

For quantum-mechanical correlations, the magnitude of the Bell parameter $|S|$ can be as high as $2\sqrt{2}$. For the correlations of Eq. (2.48), the maximum value of $|S|$ is obtained for the following settings of Φ_s and Φ_i : $\Phi_s = -22.5^\circ$, $\Phi_s^\perp = 67.5^\circ$, $\Phi_s' = 22.5^\circ$, $\Phi_s'^\perp = 112.5^\circ$; $\Phi_i = -45^\circ$, $\Phi_i^\perp = 45^\circ$, $\Phi_i' = 0^\circ$, $\Phi_i'^\perp = 90^\circ$. The magnitude of the Bell parameter $|S|$ is directly related to the visibility V of the coincidence fringes by the simple relation $|S| = 2\sqrt{2}V$. Thus an experimental demonstration of sinusoidal two-photon fringes as a function of Φ_s , at the four given settings of Φ_i , with visibilities more than 70.7% would imply a violation of CHSH-Bell inequality.

In all the experimental realizations of Franson's scheme so far, the phases of the signal and idler photons, Φ_s and Φ_i , have been changed by adjusting their dynamic phases, i.e., by adjusting their optical path lengths [8, 9]. Therefore, all these previous violations can be said to be the dynamic phase-based violations of Bell inequality for energy and time. In the next section, we show that the Bell inequality for energy and time can also be violated using geometric phases of the signal and idler photons and that therefore the time-energy entanglement can be explored using their geometric phases.

2.10 Exploring time-energy entanglement using geometric phase

Geometric phase, or Berry's phase, is the phase acquired by a system when it is transported around a closed circuit in an abstract space [100]. The manifestation of this phase in polarization optics is also known as Pancharatnam phase, which is the phase acquired by a photon field when its polarization is taken through a

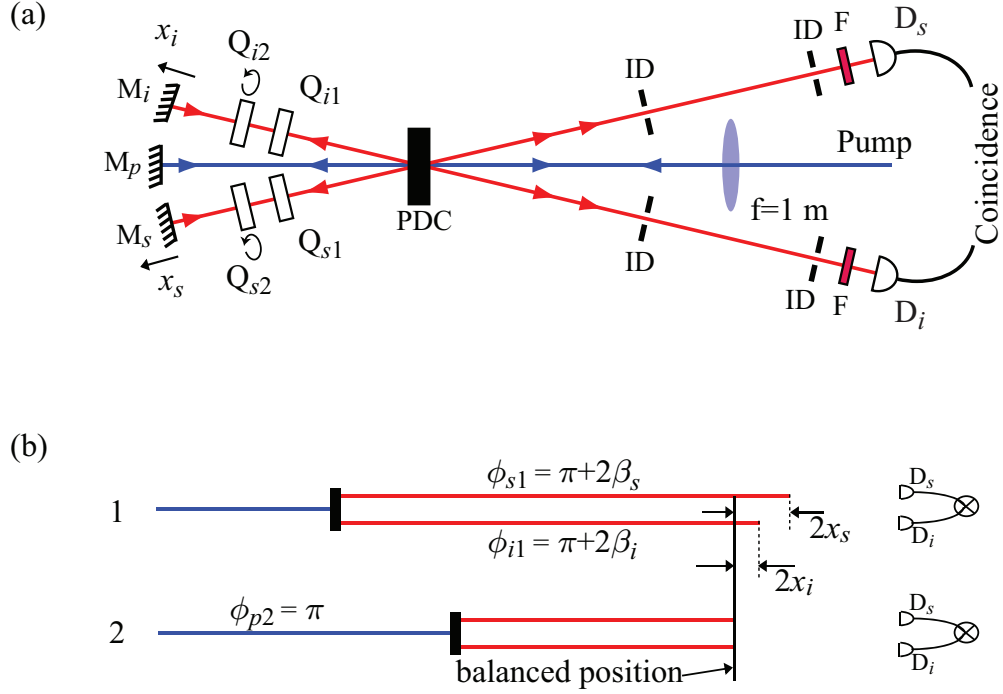


Figure 2.7: (a) Schematic of the experimental setup. Q_{s1} and Q_{i1} are quarter-wave plates with their optic axes oriented at 45° from the horizontal polarization direction. Q_{s2} and Q_{i2} are rotatable quarter-wave plates with their optic axes oriented at angles $135^\circ + \beta_s$ and $135^\circ + \beta_i$ from the horizontal polarization direction respectively. F is an interference filter with 10-nm bandwidth, centered at 727.6 nm; ID is an iris diaphragm. The signal and idler photons are collected into multimode fibers and detected using two avalanche photodiodes. A weak lens ($f=1$ m) focuses the pump beam onto the pump mirror M_p . (b) Two-photon path diagrams illustrating how the geometric phases $2\beta_s$ and $2\beta_i$ influence the two-photon interference.

closed circuit on the Poincaré sphere [101, 102, 103]. Pancharatnam phase has been observed both at high light levels [89, 104, 105] and at a single photon level [106]. Effects of Pancharatnam phase in two-photon interference, using the signal and idler photons produced by parametric downconversion (PDC), have also been studied in many different situations [83, 107, 108, 109, 110].

In what follows we show that the Bell inequality for time and energy can also be violated using the geometric phases of the signal and idler photons. Consider the double-pass setup [5] shown in Fig. 2.7(a). A cw Ar-ion laser operating at 363.8 nm is used as a pump to produce degenerate type-I parametric down-conversion

(PDC). The pump is vertically polarized and the down-converted photons are both horizontally polarized. The quarter-wave plates Q_{s1} and Q_{i1} are arranged with their optic axes oriented at angle 45° from the horizontal polarization direction, while the rotatable quarter-wave plates Q_{s2} and Q_{i2} are arranged with their optic axes oriented at angles $135^\circ + \beta_s$ and $135^\circ + \beta_i$ from the horizontal polarization direction, respectively. In this setup there are two alternative pathways—represented by the two-photon path diagrams in Fig. 2.7(b)—by which the pump photon gets down-converted and the down-converted photons get detected at single-photon detectors D_s and D_i . In alternative 1, a pump photon gets down-converted in its forward pass and the down-converted signal and idler photons reach the two detectors D_s and D_i after passing through the quarter-wave plates and getting reflected from the signal (M_s) and idler (M_i) mirrors. In alternative 2, a pump photon gets down-converted after getting reflected from the pump mirror (M_p) and the down-converted photons directly reach their respective detectors.

In alternative 1, a horizontally polarized signal photon passes through the quarter-wave plates Q_{s1} and Q_{s2} , gets reflected back from the signal mirror M_s and retraces its path through the quarter-wave plates Q_{s2} and Q_{s1} . It becomes horizontally polarized after completing the loop but in this process it acquires a geometric phase equal to $2\beta_s$, as illustrated in Fig. 2.8. This phase is in addition to the dynamic phase that the signal photon acquires. Similarly, the idler photon acquires a geometric phase equal to $2\beta_i$ in alternative 1. In the balanced position of the setup in Fig. 2.7(a), the optical path lengths between the crystal and each of the three mirrors are assumed to be equal, to about 15 cm. The displacements of the signal and idler mirrors from the balanced position are denoted by x_s and x_i respectively. The complete two-photon state $|\psi_{\text{tp}}\rangle$ produced by the double pass setup of Fig. 2.7(a) is the coherent sum of the two-photon states produced in alternatives 1 and 2, and using the definitions in

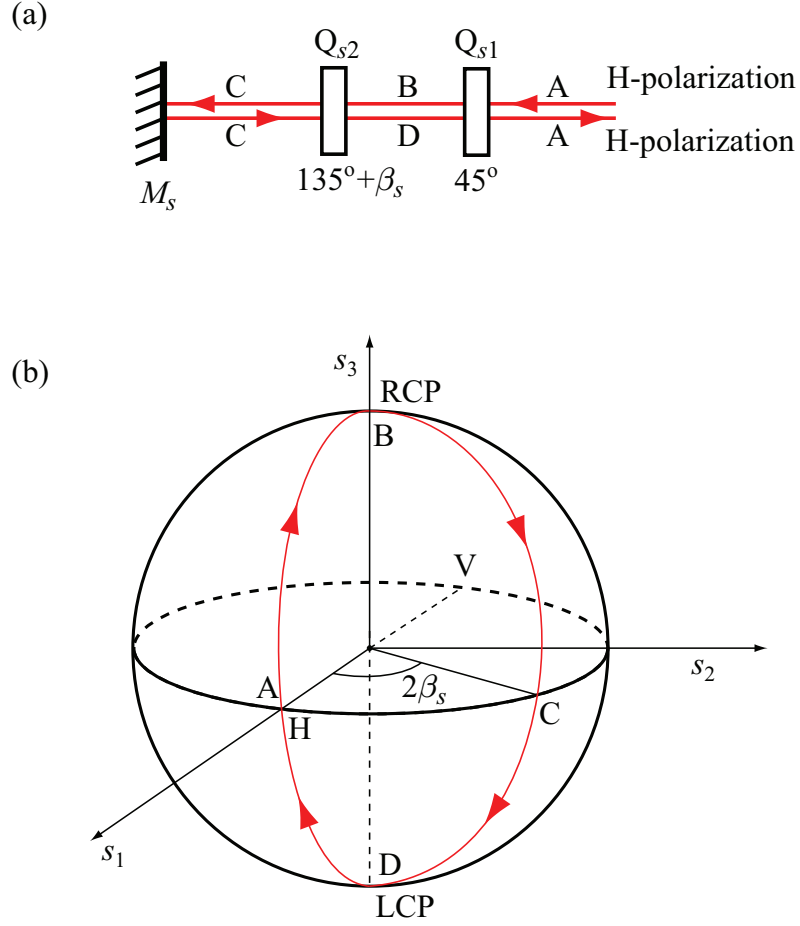


Figure 2.8: (a) The signal photon path ABCDA through the two quarter-wave plates Q_{s1} and Q_{s2} , in alternative 1. (b) Poincaré-sphere representation of polarization states of the signal photon corresponding to path ABCDA. Here, H and V represent horizontal and vertical polarizations, and RCP and LCP represent right and left circular polarizations. A signal photon acquires a phase $2\beta_s$ in going through path ABCDA, which is equal to half of the solid angle subtended by the closed circuit ABCDA on the Poincaré sphere.

Eq. (2.13), we write it as

$$|\psi_{\text{tp}}\rangle = |\psi_{\text{tp}}\rangle_1 + e^{-i(k_0\Delta L + \Delta\phi)} |\psi_{\text{tp}}\rangle_2. \quad (2.51)$$

Here $|\psi_{\text{tp}}\rangle_{1(2)}$ is the two-photon state in alternative 1(2); k_0 is the mean vacuum wavevector magnitude of the pump wave and $k_0\Delta L + \Delta\phi$ is the relative phase of the

two-photon state in alternative 2 with respect to the two-photon state in alternative 1. Interference is observed in the coincidence count rate R_{si} of detectors D_s and D_i , which can be calculated using the general expression given in Eq. (2.39):

$$R_{si} = C[1 + \gamma(\Delta L)\gamma'(\Delta L') \cos(k_0\Delta L + \Delta\phi)]. \quad (2.52)$$

Here C is a constant; $\gamma(\Delta L)$ is the time-averaged degree of correlation of the pump field, with a width equal to l_{coh}^p , the coherence length of the pump, which in our case is about 5 cm; $\gamma'(\Delta L')$ is the time-averaged degree of correlation of the signal-idler field with a width equal to l_{coh} . The signal-idler coherence length l_{coh} is determined by the widths of the interference filters and by the sizes of the iris diaphragms, and is equal to about 100 μm in our case. From the two-photon path diagram [Fig. 2.7(b)] and using Eq. (2.13), we find that $\Delta L = x_s + x_i$, $\Delta L' = 2x_s - 2x_i$ and $\Delta\phi = 2\beta_s + 2\beta_i + \pi$. With $|\Delta L| \ll l_{\text{coh}}^p$ and $|\Delta L'| \ll l_{\text{coh}}$, Eq. (2.52) simplifies to

$$R_{si} = C\{1 - \cos[k_0(x_s + x_i) + 2\beta_s + 2\beta_i]\}. \quad (2.53)$$

When the geometric phase $2\beta_s + 2\beta_i$ is held fixed, the variation of the coincidence count rate R_{si} with the dynamic phase $k_0(x_s + x_i)$ is of the form shown by Franson [7] to lead to a violation of a CHSH-Bell inequality. Bell inequality violations based on dynamic phase have been reported in many experiments [8, 9, 72]. Similarly, we note that when the dynamic phase $k_0(x_s + x_i)$ is held fixed and the geometric phase $2\beta_s + 2\beta_i$ is varied, the nature of the variation of the coincidence count rate R_{si} is still of the form to lead to a violation of the CHSH-Bell inequality, but this time based solely on geometric phase. We next describe our experimental procedure for establishing a violation of this inequality.

The experimental setup was initially aligned such that the distances of the three mirrors from the crystal were all equal to within a millimeter, and thus the condition $|\Delta L| = |x_s + x_i| \ll l_{\text{coh}}^p$ was satisfied. The idler mirror position was then scanned

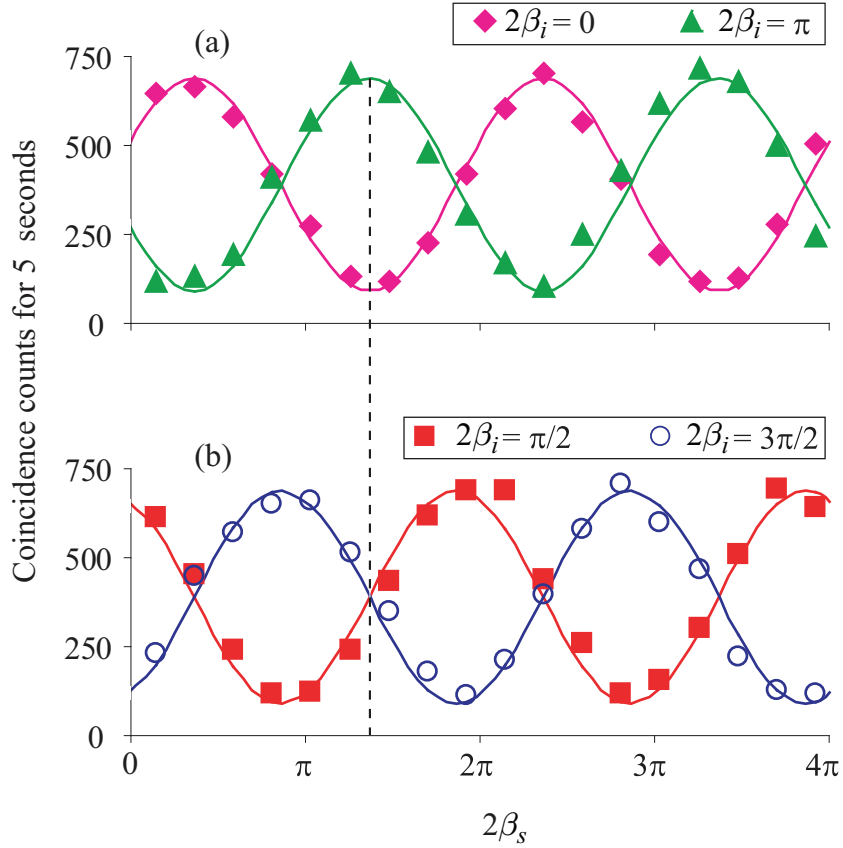


Figure 2.9: Measured number of coincidence counts as a function of $2\beta_s$, the geometric phase of signal photon in alternative 1, for four different fixed values of $2\beta_i$, the geometric phase of idler photon in alternative 1. (a) $2\beta_i=0$ and π ; (b) $2\beta_i=\pi/2$ and $3\pi/2$. The solid lines are sinusoidal fits. The distance of the dashed line from the origin is a measure of the fixed value of $k_0(x_s + x_i)$ to within the period 2π .

to observe fringes in the coincidence count rate as a function of x_i , and it was fixed at a position around which the observed fringe visibility was maximum. At this position, x_s and x_i were equal to within a few microns and thus the condition $|\Delta L'| = |2x_i - 2x_s| \ll l_{\text{coh}}$ was adequately satisfied. Next, the quarter-wave plate Q_{i2} was successively fixed at four different values of $2\beta_i$: $0, \pi/2, \pi, 3\pi/2$. For each value of $2\beta_i$, coincidence counts were measured as a function of $2\beta_s$. Figure 2.9 shows the number of coincidence counts plotted against $2\beta_s$ for four different values of $2\beta_i$.

The fringe visibilities shown in these plots are approximately 77%. An experimental demonstration of a violation of a CHSH-Bell inequality requires that the visibility

of coincidence fringes be greater than 70.7% [63, 99]. The value of the Bell parameter $|S|$ is determined by the visibility of the coincidence fringes [8, 21]. The sinusoidal coincidence fringes observed in our experiment as functions of $2\beta_s$ for four given values of $2\beta_i$ with visibilities of approximately 77% imply that the magnitude of the Bell parameter $|S|$ is approximately 2.18 ± 0.04 . Therefore, these measurements show a violation of a Bell inequality by approximately 5 standard deviations. A Bell inequality acts as an entanglement witness, and its violation verifies entanglement [72, 111]. Thus, these results demonstrate that energy-time entanglement can be explored using geometric phases of the signal and idler photons. In our experiment, coincidences were collected for only 5 seconds. Our choice of the coincidence collection time was limited by the overall stability of the interferometer. By collecting coincidences for a longer period of time, a violation with an increased number of standard deviations can be achieved [87].

Although 77% visibility is sufficient to show a Bell inequality violation, certain quantum information protocols require visibilities closer to 100%. The main reason for low visibility in our experimental setup is the imperfect overlap of the two interfering two-photon modes. This is caused by the relatively large divergences of the signal and idler modes in alternative 1 compared to their divergences in alternative 2. This effect could be minimized by using a single spherical mirror, with its center of curvature located at the crystal, for reflecting the pump, signal and idler modes [112, 113]. Another reason for low visibility is the unequal coincidence count rates in the two alternatives. This problem can be taken care of by inserting a variable neutral density filter into the pump beam path between the crystal and the pump mirror. The above factors have also been noted to cause low visibilities in energy-time entanglement experiments based on dynamic phase [8]. We believe that by using customized experimental setups, visibilities closer to the theoretical maximum of 100% should be achievable.

Geometric phase has found many applications in optics [114, 115]. One of the dis-

tinguishing features of geometric phase is its non-dispersive nature. Dynamic phase is introduced by changing the optical path length, and it remains inversely proportional to the wavelength. However, geometric phase is a topological phase and does not depend directly on the wavelength. The non-dispersive nature of geometric phase has been demonstrated in white-light interference using achromatic wave plates [114].

For quantum information science, one potential benefit of using geometric phase could be in exploring the time-energy entanglement of ultrabroadband PDC sources [116, 117]. For such sources, the signal-idler coherence length l_{coh} remains so small that the visibility of two-photon fringes—which is the magnitude of the product $\gamma(\Delta L)\gamma(\Delta L')$ —does not remain constant over the variations of $\Delta L'$ that are of the order of a wavelength. Therefore, with such sources, dynamic phase is unsuitable for performing Bell inequality violation experiments. Geometric phase, on the other hand, is non-dispersive. Changing geometric phase does not change the optical path lengths. Therefore, the two-photon fringe visibility remains constant as a function of the phase introduced geometrically, and this makes geometric phase particularly suitable for exploring the time-energy entanglement of ultrabroadband PDC sources.

Another benefit of using geometric phase lies in the ease of introducing very small phase shifts. In contrast with dynamic phase, where motorized translation stages are employed, geometric phase is quite easily manipulated by using rotating wave plates. These features of geometric phase may also aid in the construction of hyperentangled states [69, 70, 71, 72] with time-energy as one of the degrees of freedom.

2.11 Summary

The description of temporal two-photon interference with the signal and idler photons produced by parametric down-conversion involves, in general, six different length parameters. Using these six length parameters, we have constructed two independent length parameters—called the two-photon path-length difference and the two-photon

path-asymmetry length difference. In terms of the two length parameters, we have studied the temporal coherence properties of the two-photon field, in situations in which the frequency bandwidth of the pump field remains much narrower than that of the signal and idler fields. We have shown that temporal two-photon interference effects can be completely characterized in terms of the two constructed length parameters. We have also performed experiments in the double-pass setup where the effects due to the variations of these two parameters could be independently controlled and studied. We have reported experimental observations of “HOM-like” effects both in coincidence and in one-photon count rates, and we have argued that HOM and HOM-like effects can be best understood as observations of how two-photon coherence changes with a variation in the two-photon path-asymmetry-length difference.

Finally, we have presented our work related to exploring time-energy entanglement. In particular, we have shown that the time-energy entanglement of the down-converted signal and idler photons can be explored by means of their geometric phases. Using a double-pass setup, we have reported experimental observations of a violation of the Bell inequality for time and energy based purely on the geometric phases of the entangled signal and idler photons. These results provide an additional means by which entanglement can be manipulated, and therefore they may have important practical implications for quantum information science.

Chapter 3

Two-Photon Coherence Effects: Spatial

3.1 Introduction

The spatial coherence properties of the two-photon field produced by parametric down-conversion are affected by the crystal parameters as well as by the pump field parameters and have been studied in various different contexts [53, 86, 118, 119, 120, 121, 122]. In particular, it has been shown that the angular spectrum of the pump field gets completely transferred to the down-converted two-photon field [86]. Using the down-converted photons, several spatial two-photon interference effects have also been observed [123, 124, 125, 126, 127, 128, 129, 130]. In all these previous studies, the pump field has been taken to be spatially coherent, and the effects due to the limited spatial coherence of the pump field have so far not been investigated. In this chapter, the formalism developed in Chapter 2 for studying the temporal coherence effects is extended to include the spatial coherence effects. We study how the spatial coherence properties of the down-converted two-photon field get affected when the pump field is, spatially, a partially coherent beam.

This chapter is organized as follows. Section 3.2 presents a derivation of the two-

photon state produced by parametric down-conversion for the general case. In Section 3.3, we present a conceptual description of spatial two-photon interference in terms of two displacement parameters, which we construct using the transverse position vectors of the signal and idler photons in two interfering alternatives. In Sections 3.4 and 3.5, taking the pump field to be a partially coherent, Gaussian Schell-model beam [2, 30, 42], we show in terms of the two displacement parameters that the spatial coherence properties of the pump field get entirely transferred to the down-converted two-photon field. In Section 3.6, we discuss position-momentum entanglement and in Section 3.7, we study the connection between spatial two-photon coherence and the degree of entanglement of two-qubit states that are based on spatial correlations. We show that the entanglement of the spatial two-qubit states is directly related to the degree of spatial two-photon-coherence, and thus to the coherence properties of the pump field. Section 3.8 presents the summary.

3.2 Two-photon state produced by parametric down-conversion

The interaction Hamiltonian $\hat{H}(t')$ for parametric down-conversion is given by [see Eq. (1.21)]

$$\hat{H}(t') = \frac{\epsilon_0}{2} \int_{\mathcal{V}} d^3\mathbf{r} \chi^{(2)} \hat{E}_p^{(+)}(\mathbf{r}, t') \hat{E}_s^{(-)}(\mathbf{r}, t') \hat{E}_i^{(-)}(\mathbf{r}, t') + \text{H.c.}, \quad (3.1)$$

where \mathcal{V} is the volume of the interacting part of the nonlinear crystal; $\chi^{(2)}$ is the second-order nonlinear susceptibility; $\hat{E}_j^{(+)}(\mathbf{r}, t')$ and $\hat{E}_j^{(-)}(\mathbf{r}, t')$ are the positive- and negative-frequency parts of the field, where $j = p, s, i$ stands for the pump, signal and idler, respectively. We assume that the nonlinear crystal is embedded in a passive linear medium of suitable refractive index and that $\chi^{(2)}$ is independent of frequency

over the range of interest. [53, 86]. The three electric fields are written as

$$\hat{E}_p^{(+)}(\mathbf{r}, t') = \int_0^\infty A_p d^3 \mathbf{k}_p V(\mathbf{k}_p) e^{i(\mathbf{k}_p \cdot \mathbf{r} - \omega_p t')}, \quad (3.2)$$

$$\hat{E}_s^{(-)}(\mathbf{r}, t') = \int_0^\infty A_s^* d^3 \mathbf{k}_s \hat{a}_s^\dagger(\mathbf{k}_s) e^{i(\omega_s t' - \mathbf{k}_s \cdot \mathbf{r})}, \quad (3.3)$$

$$\hat{E}_i^{(-)}(\mathbf{r}, t') = \int_0^\infty A_i^* d^3 \mathbf{k}_i \hat{a}_i^\dagger(\mathbf{k}_i) e^{i(\omega_i t' - \mathbf{k}_i \cdot \mathbf{r})}. \quad (3.4)$$

Here $\mathbf{r} = (\boldsymbol{\rho}, z)$ and $\mathbf{k}_j = (\mathbf{q}_j, k_{jz})$. A_j is a frequency dependent quantity, and as it varies very slowly within the frequency range of interest for most two-photon interference experiments, it is taken outside the integral. The pump field has been assumed to be very strong, and it will be treated classically. The strength of the pump field at (ω_p, \mathbf{q}_p) is represented by $V(\omega_p, \mathbf{q}_p)$. Using the expressions for the three fields above, we write Eq. (3.1) as

$$\begin{aligned} \hat{H}(t') = \frac{A_p A_s^* A_i^* \epsilon_0 \chi^{(2)}}{2} \int_V d^3 \mathbf{r} \iiint \int_0^\infty d^3 \mathbf{k}_p d^3 \mathbf{k}_s d^3 \mathbf{k}_i V(\mathbf{k}_p) \hat{a}_s^\dagger(\mathbf{k}_s) \hat{a}_i^\dagger(\mathbf{k}_i) \\ \times e^{i(\mathbf{k}_p - \mathbf{k}_s - \mathbf{k}_i) \cdot \mathbf{r}} e^{i(\omega_s + \omega_i - \omega_p) t'} + \text{H.c.} \end{aligned} \quad (3.5)$$

The state $|\psi(0)\rangle$ of the down-converted field at $t' = 0$ is given by Eq. (2.7)

$$|\psi(0)\rangle = \exp \left[\frac{1}{i\hbar} \int_{-t_{\text{int}}}^0 dt' \hat{H}(t') \right] |\psi(-t_{\text{int}})\rangle, \quad (3.6)$$

Here $|\psi(-t_{\text{int}})\rangle = |\text{vac}\rangle_s |\text{vac}\rangle_i$ is the state of the down-converted field at $t' = -t_{\text{int}}$ which is a vacuum state with no photons in either the signal or the idler mode. The parametric interaction is assumed to be very weak and the state in Eq. (3.6) is approximated by the first two terms of a perturbative expansion. The first term is the initial vacuum state. The second term $|\psi\rangle$ is calculated by substituting from

Eq. (3.5) into Eq. (3.6), which yields

$$\begin{aligned}
|\psi\rangle = & \frac{A_p A_s^* A_i^* \epsilon_0 \chi^{(2)}}{2i\hbar} \int_{-t_{\text{int}}}^0 dt' \int_{\mathcal{V}} d^3\mathbf{r} \iiint_0^\infty d\omega_p d\omega_s d\omega_i \\
& \times \iiint d\mathbf{q}_p d\mathbf{q}_s d\mathbf{q}_i V(\omega_p, \mathbf{q}_p) e^{i[(\mathbf{q}_p - \mathbf{q}_s - \mathbf{q}_i) \cdot \boldsymbol{\rho} + (k_{pz} - k_{sz} - k_{iz})z]} \\
& \times e^{i(\omega_s + \omega_i - \omega_p)t'} \hat{a}_s^\dagger(\omega_s, \mathbf{q}_s) \hat{a}_i^\dagger(\omega_i, \mathbf{q}_i) |\text{vac}\rangle_s |\text{vac}\rangle_i. \quad (3.7)
\end{aligned}$$

The interaction time t_{int} is assumed to be much longer than the time scale over which down-conversion takes place and much smaller than the time interval between two consecutive down-conversion events. The limits of time integration in Eq. (3.7) are therefore extended to $\pm\infty$ [84, 88]. We evaluate the time integral, which yields the delta function $\delta(\omega_p - \omega_s - \omega_i)$. Integrating over ω_i , we obtain

$$\begin{aligned}
|\psi\rangle = & A \iint_0^\infty d\omega_p d\omega_s \iiint d\mathbf{q}_p d\mathbf{q}_s d\mathbf{q}_i V(\omega_p, \mathbf{q}_p) \\
& \times \Phi(\omega_p, \omega_s, \mathbf{q}_p, \mathbf{q}_s, \mathbf{q}_i) |\omega_s, \mathbf{q}_s\rangle_s |\omega_p - \omega_s, \mathbf{q}_i\rangle_i, \quad (3.8)
\end{aligned}$$

where

$$\Phi(\omega_p, \omega_s, \mathbf{q}_p, \mathbf{q}_s, \mathbf{q}_i) = \int_{\mathcal{V}} d^3\mathbf{r} e^{i[(\mathbf{q}_p - \mathbf{q}_s - \mathbf{q}_i) \cdot \boldsymbol{\rho} + (k_{pz} - k_{sz} - k_{iz})z]} \quad (3.9)$$

is the phase-matching function. All the constant factors have been absorbed into A . To keep our analysis simpler, we restrict ourselves to the collinear phase-matching conditions and work within the paraxial approximations:

$$k_{jz} = k_j - \frac{q_j^2}{2k_j}; \quad q_j = |\mathbf{q}_j|, \quad k_j = |\mathbf{k}_j(\omega_j)|, \quad (3.10)$$

where $j = p, s, i$. The space integral of Eq. (3.9) can be written as two separate integrals, $\int d^3\mathbf{r} \rightarrow \int d^2\boldsymbol{\rho} \int dz$. Substituting $\Delta k = k_p - k_s - k_i$ and $\Delta q = q_p^2/2k_p - q_s^2/2k_s - q_i^2/2k_i$ and assuming that the area of the nonlinear crystal illuminated by the

pump beam is sufficiently large [86, 118], we evaluate the phase-matching function $\Phi(\omega_p, \omega_s, \mathbf{q}_p, \mathbf{q}_s, \mathbf{q}_i)$ to be

$$\begin{aligned}\Phi(\omega_p, \omega_s, \mathbf{q}_p, \mathbf{q}_s, \mathbf{q}_i) &= \int d^2\rho e^{i(\mathbf{q}_p - \mathbf{q}_s - \mathbf{q}_i) \cdot \rho} \int_{-L}^0 dz e^{i(\Delta q + \Delta k)z} \\ &= \delta(\mathbf{q}_p - \mathbf{q}_s - \mathbf{q}_i) L e^{i(\Delta q + \Delta k)L/2} \text{sinc}[(\Delta q + \Delta k)L/2].\end{aligned}\quad (3.11)$$

Here L is the thickness of the nonlinear crystal. Substituting the above expression into Eq. (3.8) and carrying out the $d\mathbf{q}_p$ integral, we obtain

$$\begin{aligned}|\psi\rangle &= A \int_0^\infty d\omega_p d\omega_s \iint d\mathbf{q}_s d\mathbf{q}_i V(\omega_p, \mathbf{q}_s + \mathbf{q}_i) e^{i(\Delta q + \Delta k)L/2} \\ &\quad \times \text{sinc}[(\Delta q + \Delta k)L/2] |\omega_s, \mathbf{q}_s\rangle_s |\omega_p - \omega_s, \mathbf{q}_i\rangle_i.\end{aligned}\quad (3.12)$$

This is the general expression for the state of the two-photon field produced by down-conversion. We have absorbed the constant factors into A . In what follows we assume, without any loss of generality, that the signal, idler and pump fields are monochromatic, with frequencies given by ω_0 , ω_s and ω_i , respectively. The two-photon state can then be written as

$$|\psi\rangle = A e^{i\Delta k L/2} \iint d\mathbf{q}_s d\mathbf{q}_i V(\mathbf{q}_s + \mathbf{q}_i) e^{i\Delta q L/2} \text{sinc}(\Delta q L/2) |\mathbf{q}_s\rangle_s |\mathbf{q}_i\rangle_i.\quad (3.13)$$

From now on, we shall not show the frequency arguments. The two-photon state given in Eq. (3.13) is a pure state from a single realization of the pump field. When the average is taken over an ensemble of different realizations of the pump field, the state of the down-converted two-photon field is given by the following density matrix ρ_{tp} :

$$\begin{aligned}\rho_{\text{tp}} &= |A|^2 \iiint d\mathbf{q}_s d\mathbf{q}_i d\mathbf{q}'_s d\mathbf{q}'_i \langle V(\mathbf{q}_s + \mathbf{q}_i) V^*(\mathbf{q}'_s + \mathbf{q}'_i) \rangle_e \\ &\quad e^{i(\Delta q - \Delta q')L/2} \text{sinc}(\Delta q L/2) \text{sinc}(\Delta q' L/2) |\mathbf{q}_s\rangle_s |\mathbf{q}_i\rangle_i \langle \mathbf{q}'_s| \langle \mathbf{q}'_i|.\end{aligned}\quad (3.14)$$

The ensemble average $\langle V(\mathbf{q}_s + \mathbf{q}_i)V^*(\mathbf{q}'_s + \mathbf{q}'_i) \rangle_e$ is recognized as the angular correlation function of the pump field [131], with $\mathbf{q}_s + \mathbf{q}_i = \mathbf{q}_p$ and $\mathbf{q}'_s + \mathbf{q}'_i = \mathbf{q}'_p$ being the transverse wave-vectors of the pump field. In the following sections, we use the above density matrix to calculate the correlation functions for the two-photon field.

3.3 Spatial two-photon interference: conceptual description

Figure 3.1 represents a generic situation for studying the spatial coherence properties of the two-photon field. The signal and idler photons produced by PDC go through a pair of double-holes located at plane z . They are detected in coincidence by detectors D_s and D_i located at positions \mathbf{r}_s and \mathbf{r}_i , respectively. There are two alternative pathways, by which signal and idler photons can reach detectors D_s and D_i . In alternative 1, the signal and idler photons go through the pair of holes located at $\mathbf{r}_{s1}(\boldsymbol{\rho}_{s1}, z)$ and $\mathbf{r}_{i1}(\boldsymbol{\rho}_{i1}, z)$, and in alternative 2, they go through those located at $\mathbf{r}_{s2}(\boldsymbol{\rho}_{s2}, z)$ and $\mathbf{r}_{i2}(\boldsymbol{\rho}_{i2}, z)$. In principle, there are two more alternative pathways: one in which the signal and idler photons go through the pair of holes located at $\mathbf{r}_{s1}(\boldsymbol{\rho}_{s1}, z)$ and $\mathbf{r}_{i2}(\boldsymbol{\rho}_{i2}, z)$, and the second in which they go through those located at $\mathbf{r}_{s2}(\boldsymbol{\rho}_{s2}, z)$ and $\mathbf{r}_{i1}(\boldsymbol{\rho}_{i1}, z)$. In what follows we explicitly assume that the phase matching condition is such that the probability amplitudes of these two other alternatives are negligibly small.

In Fig. 3.1, subscripts p , s , and i stand for pump, signal, and idler, respectively. The distance travelled by a photon from the crystal to a hole is denoted by r . The distance travelled from a hole to the corresponding detector is denoted by d and the associated time elapsed by $t = d/c$. The transverse position vector of a photon is denoted by $\boldsymbol{\rho}$. Thus $\boldsymbol{\rho}_{s1}$ represents the transverse position vector of the signal photon in alternative 1, etc. We define two displacement parameters in terms of the

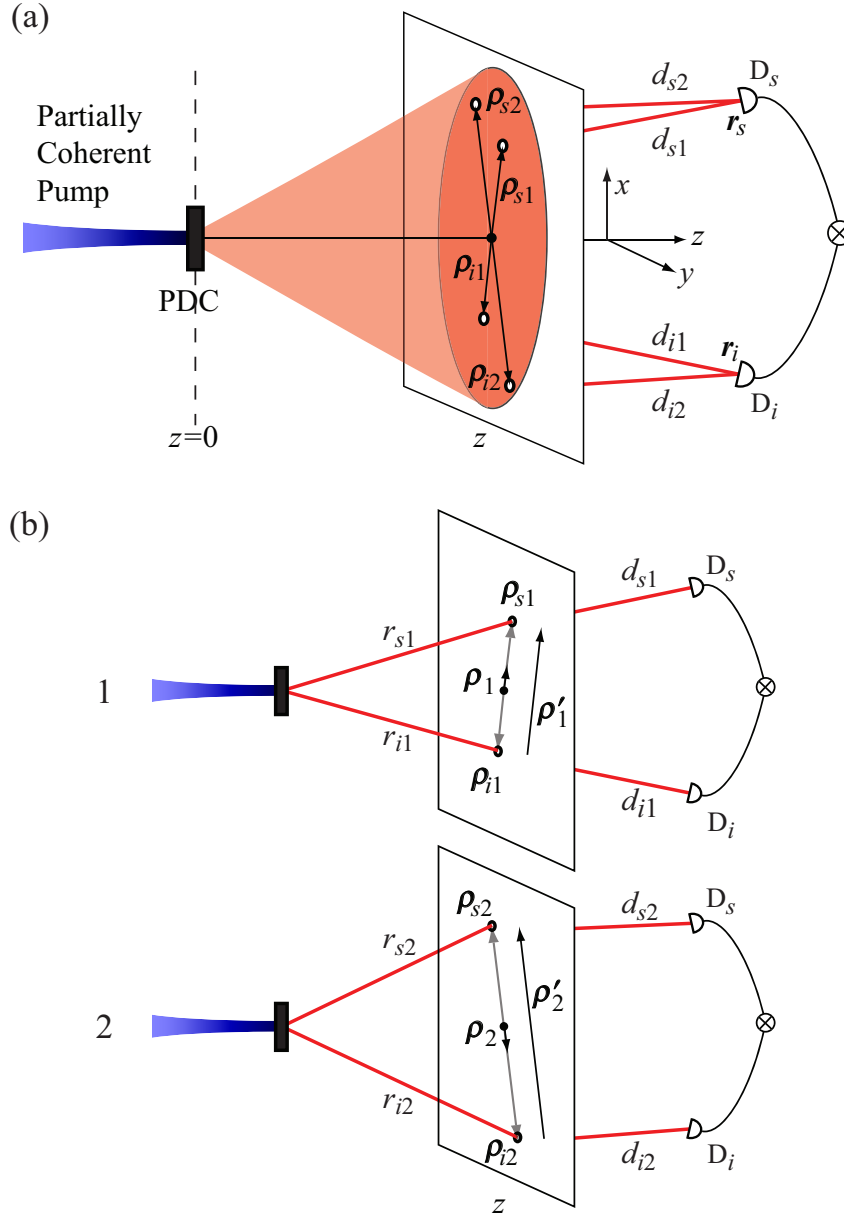


Figure 3.1: (a) Schematic laboratory setup that could be used to study the spatial coherence properties of the two-photon field produced by PDC using a partially coherent pump beam. (b) 1 and 2 represent two alternative pathways by which the down-converted signal and idler photons can pass through the holes and get detected in coincidence at detectors D_s and D_i . In alternative 1, the signal and idler photons go through the pair of holes located at $\mathbf{r}_{s1}(\rho_{s1}, z)$ and $\mathbf{r}_{i1}(\rho_{i1}, z)$, and in alternative 2, they go through those located at $\mathbf{r}_{s2}(\rho_{s2}, z)$ and $\mathbf{r}_{i2}(\rho_{i2}, z)$.

transverse position vectors of the signal and idler photons in the two alternatives as:

$$\begin{aligned}\Delta\boldsymbol{\rho} &= \boldsymbol{\rho}_1 - \boldsymbol{\rho}_2 \equiv \frac{\boldsymbol{\rho}_{s1} + \boldsymbol{\rho}_{i1}}{2} - \frac{\boldsymbol{\rho}_{s2} + \boldsymbol{\rho}_{i2}}{2}, \\ \Delta\boldsymbol{\rho}' &= \boldsymbol{\rho}'_1 - \boldsymbol{\rho}'_2 \equiv (\boldsymbol{\rho}_{s1} - \boldsymbol{\rho}_{i1}) - (\boldsymbol{\rho}_{s2} - \boldsymbol{\rho}_{i2}).\end{aligned}\quad (3.15)$$

Here $\boldsymbol{\rho}_{1(2)}$ and $\boldsymbol{\rho}'_{1(2)}$ are the two-photon transverse position vector and the two-photon position-asymmetry vector in alternative 1(2). For either alternative, the two-photon transverse position vector is defined to be the average of the transverse position vectors of the signal and idler photons, and the two-photon position-asymmetry vector is defined to be the difference of the transverse position vectors of the signal and idler photons.

We denote the positive-frequency parts of the electric fields at detectors D_s and D_i by $\hat{E}_s^{(+)}(\mathbf{r}_s, t)$ and $\hat{E}_i^{(+)}(\mathbf{r}_i, t)$, respectively. $\hat{E}_s^{(+)}(\mathbf{r}_s, t)$ and $\hat{E}_i^{(+)}(\mathbf{r}_i, t)$ are equal to the sum of the signal and idler fields arriving at detectors D_s and D_i by alternatives 1 and 2, i.e.,

$$\hat{E}_s^{(+)}(\mathbf{r}_s, t) = k_{s1}\hat{E}_{s1}^{(+)}(\mathbf{r}_{s1})e^{-i\omega_s(t-t_{s1})} + k_{s2}\hat{E}_{s2}^{(+)}(\mathbf{r}_{s2})e^{-i\omega_s(t-t_{s2})}, \quad (3.16)$$

$$\hat{E}_i^{(+)}(\mathbf{r}_i, t) = k_{i1}\hat{E}_{i1}^{(+)}(\mathbf{r}_{i1})e^{-i\omega_i(t-t_{i1})} + k_{i2}\hat{E}_{i2}^{(+)}(\mathbf{r}_{i2})e^{-i\omega_i(t-t_{i2})}. \quad (3.17)$$

Here $\hat{E}_{i1}^{(+)}(\mathbf{r}_{s1})$ is the positive-frequency part of the signal field at position \mathbf{r}_{s1} , etc. The constant factor k_{s1} depends on the size of the hole at r_{s1} and the geometry of the arrangement, etc. The coincidence count rate $R_{si}(\mathbf{r}_s, \mathbf{r}_i)$, which is the probability per (unit time)² that a photon is detected at position \mathbf{r}_s at time t and another at position \mathbf{r}_i at time $t+\tau$, is given by $R_{si}(\mathbf{r}_s, \mathbf{r}_i) = \alpha_s\alpha_i\text{tr}\{\rho_{\text{tp}}\hat{E}_s^{(-)}(\mathbf{r}_s)\hat{E}_i^{(-)}(\mathbf{r}_i)\hat{E}_i^{(+)}(\mathbf{r}_i)\hat{E}_s^{(+)}(\mathbf{r}_s)\}$ [31], where the symbol tr stands for the trace, α_s and α_i denote the quantum efficiencies of detectors D_s and D_i , respectively, and ρ_{tp} is the density matrix of the two-photon field produced by PDC. By substituting from Eqs. (3.16) and (3.17), we

write the coincidence count rate $R_{si}(\mathbf{r}_s, \mathbf{r}_i)$ as

$$R_{si}(\mathbf{r}_s, \mathbf{r}_i) = k_1^2 S^{(2)}(\boldsymbol{\rho}_{s1}, \boldsymbol{\rho}_{i1}, z) + k_2^2 S^{(2)}(\boldsymbol{\rho}_{s2}, \boldsymbol{\rho}_{i2}, z) \\ + k_1 k_2 W^{(2)}(\boldsymbol{\rho}_{s1}, \boldsymbol{\rho}_{i1}, \boldsymbol{\rho}_{s2}, \boldsymbol{\rho}_{i2}, z) e^{i[\omega_s(t_{s1}-t_{s2})+\omega_i(t_{i1}-t_{i2})]} + \text{c.c.} \quad (3.18a)$$

where $k_1 = \sqrt{\alpha_s \alpha_i} k_{s1} k_{i1}$, $k_2 = \sqrt{\alpha_s \alpha_i} k_{s2} k_{i2}$,

$$W^{(2)}(\boldsymbol{\rho}_{s1}, \boldsymbol{\rho}_{i1}, \boldsymbol{\rho}_{s2}, \boldsymbol{\rho}_{i2}, z) = \text{tr}\{\rho_{\text{tp}} \hat{E}^{(-)}(\mathbf{r}_{s1}) \hat{E}^{(-)}(\mathbf{r}_{i1}) \hat{E}^{(+)}(\mathbf{r}_{i2}) \hat{E}^{(+)}(\mathbf{r}_{s2})\} \quad (3.18b)$$

and

$$S^{(2)}(\boldsymbol{\rho}_{s1}, \boldsymbol{\rho}_{i1}, z) = W^{(2)}(\boldsymbol{\rho}_{s1}, \boldsymbol{\rho}_{i1}, \boldsymbol{\rho}_{s1}, \boldsymbol{\rho}_{i1}, z). \quad (3.18c)$$

Equation (3.18a) is the interference law for the two-photon field. The first and second terms of Eq. (3.18a) are the coincidence count rates when coincidences are collected from only alternatives 1 and 2, respectively. These terms are recognized as the two-photon analogs of the spectral density functions of the second-order coherence theory. $S^{(2)}(\boldsymbol{\rho}_{s1}, \boldsymbol{\rho}_{i1}, z)$ will be referred to as the two-photon spectral density in alternative 1, etc. The interference term $W^{(2)}(\boldsymbol{\rho}_{s1}, \boldsymbol{\rho}_{i1}, \boldsymbol{\rho}_{s2}, \boldsymbol{\rho}_{i2}, z)$, which appears when coincidences are collected from both the alternatives, is a four-point fourth-order (in the field) correlation function. It satisfies four Wolf Equations [2, 31, 122] and is recognized as the two-photon analog of the cross-spectral density function. $W^{(2)}(\boldsymbol{\rho}_{s1}, \boldsymbol{\rho}_{i1}, \boldsymbol{\rho}_{s2}, \boldsymbol{\rho}_{i2}, z)$ will be referred to as the two-photon cross-spectral density function. To keep the notations simpler, we do not show the frequency arguments in the definitions of the two-photon spectral density and the two-photon cross-spectral density functions.

3.4 Spatial coherence properties of the two-photon field: the degenerate case

We evaluate the two-photon cross-spectral density function $W^{(2)}(\boldsymbol{\rho}_{s1}, \boldsymbol{\rho}_{i1}, \boldsymbol{\rho}_{s2}, \boldsymbol{\rho}_{i2}, z)$, and thereby the coincidence count rate $R_{si}(\mathbf{r}_s, \mathbf{r}_i)$, in terms of the two displacement parameters defined in Eq. (3.15). This section presents our calculations for the case of degenerate down-conversion only; the non-degenerate case is presented in the next section. So, in this section, we take $\omega_s = \omega_i = \omega_0/2$ and, within the paraxial approximations, take $k_s \approx k_i \approx k_0/2$, where k_0 is the central wave-vector magnitude of the pump field. We take the down-conversion crystal to be very thin, that is $L = 0$. The general expression for the state of the two-photon field produced by PDC is given by the density matrix ρ_{tp} in Eq. (3.14). With the thin crystal approximation, Eq. (3.14) becomes

$$\rho_{\text{tp}} = |A|^2 \iiint d\mathbf{q}_s d\mathbf{q}_i d\mathbf{q}'_s d\mathbf{q}'_i \langle V(\mathbf{q}_s + \mathbf{q}_i) V^*(\mathbf{q}'_s + \mathbf{q}'_i) \rangle_e |\mathbf{q}_s\rangle |\mathbf{q}_i\rangle \langle \mathbf{q}'_i| \langle \mathbf{q}'_s| \quad (3.19)$$

where $\langle \dots \rangle_e$ represents the ensemble average over the different realizations of the pump field, and where \mathbf{q}_s and \mathbf{q}_i are the transverse wave-vectors of the signal and idler fields. As mentioned, $\langle V(\mathbf{q}_s + \mathbf{q}_i) V^*(\mathbf{q}'_s + \mathbf{q}'_i) \rangle_e$ is the angular correlation function of the pump field [131]. The electric field operators $\hat{E}_{s1}^{(+)}(\mathbf{r}_{s1})$ and $\hat{E}_{i1}^{(+)}(\mathbf{r}_{i1})$, within the paraxial approximation, can be written as [53, 86, 118]:

$$\hat{E}_{s1}^{(+)}(\mathbf{r}_{s1}) = e^{ik_0 z/2} \int d\mathbf{q} \hat{a}_s(\mathbf{q}) e^{i(\mathbf{q} \cdot \boldsymbol{\rho}_{s1} - q^2 z/k_0)}, \quad (3.20)$$

$$\hat{E}_{i1}^{(+)}(\mathbf{r}_{i1}) = e^{ik_0 z/2} \int d\mathbf{q}' \hat{a}_i(\mathbf{q}') e^{i(\mathbf{q}' \cdot \boldsymbol{\rho}_{i1} - q'^2 z/k_0)}, \quad (3.21)$$

where $q^2 = |\mathbf{q}|^2$, $q'^2 = |\mathbf{q}'|^2$ and $k_0 = |\mathbf{k}_0(\omega_0)|$. Substituting Eqs. (3.19), (3.20) and (3.21) into Eq. (3.18b), we write the two-photon cross-spectral density as

$$\begin{aligned}
 W^{(2)}(\boldsymbol{\rho}_{s1}, \boldsymbol{\rho}_{i1}, \boldsymbol{\rho}_{s2}, \boldsymbol{\rho}_{i2}, z) = & \\
 |A|^2 \iiint \iiint d\mathbf{q}_s d\mathbf{q}'_s d\mathbf{q}_i d\mathbf{q}'_i \langle V(\mathbf{q}_s + \mathbf{q}_i) V^*(\mathbf{q}'_s + \mathbf{q}'_i) \rangle_e & \\
 \times e^{i[\mathbf{q}_s \cdot \boldsymbol{\rho}_{s1} + \mathbf{q}_i \cdot \boldsymbol{\rho}_{i1} - \mathbf{q}'_s \cdot \boldsymbol{\rho}_{s2} - \mathbf{q}'_i \cdot \boldsymbol{\rho}_{i2}]} e^{-i(z/k_0)[(q_s^2 + q_i^2) - (q'^2_s + q'^2_i)]}, & \quad (3.22)
 \end{aligned}$$

The two-photon cross-spectral density function $W^{(2)}(\boldsymbol{\rho}_{s1}, \boldsymbol{\rho}_{i1}, \boldsymbol{\rho}_{s2}, \boldsymbol{\rho}_{i2}, z)$ is an integral of the angular correlation function of the pump field; and therefore, the spatial coherence properties of the pump field get transferred to the two-photon field. We calculate the analytical expression for the two-photon cross-spectral density, for the special case of a partially coherent pump field of Gaussian Schell-model type [42].

A Gaussian Schell-model beam is characterized by its beam waist width σ_s at $z = 0$ and its transverse coherence width σ_μ at $z = 0$, which is the distance scale over which the pump field at $z = 0$ remains spatially coherent. The angular correlation function for the Gaussian Schell-model pump field is given by (see Ref. [30], Section 5.6.4):

$$\begin{aligned}
 \langle V(\mathbf{q}_s + \mathbf{q}_i) V^*(\mathbf{q}'_s + \mathbf{q}'_i) \rangle_e \rightarrow \langle V(\mathbf{q}_p) V^*(\mathbf{q}'_p) \rangle_e = & \\
 (A_p \sigma_s \delta / 2\pi)^2 \exp \left[-\alpha (\mathbf{q}_p)^2 - \alpha (\mathbf{q}'_p)^2 + 2\beta \mathbf{q}_p \cdot \mathbf{q}'_p \right], & \quad (3.23a)
 \end{aligned}$$

where

$$\alpha = \sigma_s^2 (\sigma_\mu^2 + 2\sigma_s^2) / (\sigma_\mu^2 + 4\sigma_s^2), \quad (3.23b)$$

$$\beta = 2\sigma_s^4 / (\sigma_\mu^2 + 4\sigma_s^2), \quad (3.23c)$$

$$\delta^2 = 4\sigma_s^2 \sigma_\mu^2 / (\sigma_\mu^2 + 4\sigma_s^2), \quad (3.23d)$$

and A_p is a constant. The far-field expression of the cross-spectral density function

$W(\boldsymbol{\rho}_{p1}, \boldsymbol{\rho}_{p2}, z)$ of the pump field at positions $\mathbf{r}_{p1} \equiv (\boldsymbol{\rho}_{p1}, z)$ and $\mathbf{r}_{p2} \equiv (\boldsymbol{\rho}_{p2}, z)$ along the pump beam path is then given by (see Ref. [30], Section 5.6.4):

$$W(\boldsymbol{\rho}_{p1}, \boldsymbol{\rho}_{p2}, z) = e^{ik_0(r_{p1}-r_{p2})} \sqrt{S(\boldsymbol{\rho}_{p1}, z)S(\boldsymbol{\rho}_{p2}, z)} \mu(\Delta\boldsymbol{\rho}_p, z), \quad (3.24a)$$

where $r_{p1} = |\mathbf{r}_{p1}|$, $r_{p2} = |\mathbf{r}_{p2}|$, and $\Delta\boldsymbol{\rho}_p = \boldsymbol{\rho}_{p1} - \boldsymbol{\rho}_{p2}$.

$$S(\boldsymbol{\rho}_{p1}, z) = (A_p \sigma_s \delta k_0 / z)^2 \exp \left\{ -(1/2) [\boldsymbol{\rho}_{p1} / \sigma_s(z)]^2 \right\} \quad (3.24b)$$

is the spectral density of the pump field at position \mathbf{r}_{p1} , with

$$\sigma_s(z) = z \sqrt{\sigma_\mu^2 + 4\sigma_s^2 / 2k_0 \sigma_s \sigma_\mu} \quad (3.24c)$$

being the rms beam radius of the pump field at plane z in the far field; and

$$\mu(\Delta\boldsymbol{\rho}_p, z) = \exp \left\{ -(1/2) [\Delta\boldsymbol{\rho}_p / \sigma_\mu(z)]^2 \right\}, \quad (3.24d)$$

is the degree of spatial coherence of the pump field, with

$$\sigma_\mu(z) = z \sqrt{\sigma_\mu^2 + 4\sigma_s^2 / 2k_0 \sigma_s^2} \quad (3.24e)$$

being the rms spatial coherence width of the pump field at plane z in the far field. Figure 3.2(a) illustrates the beam radius $\sigma_s(z)$ and spatial coherence width $\sigma_\mu(z)$ of a partially coherent pump beam.

We now substitute Eq. (3.23) into Eq. (3.22) and calculate the far-field expression of the two-photon cross-spectral density $W^{(2)}(\boldsymbol{\rho}_{s1}, \boldsymbol{\rho}_{i1}, \boldsymbol{\rho}_{s2}, \boldsymbol{\rho}_{i2}, z)$. After a very long

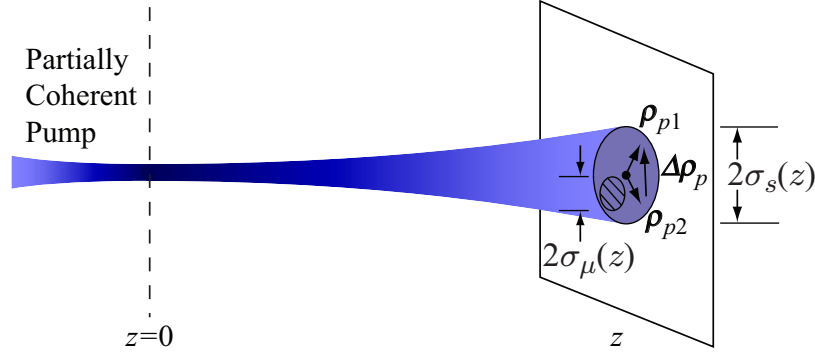


Figure 3.2: Schematic representation of a partially spatially coherent pump beam; $\sigma_s(z)$ is the rms beam radius of the pump field at plane z and $\sigma_\mu(z)$ is the rms spatial coherence width of the pump field at plane z . ρ_{p1} and ρ_{p2} are the transverse position vectors of the two points within the pump beam.

but straightforward calculation, we find that

$$\begin{aligned}
 W^{(2)}(\rho_{s1}, \rho_{i1}, \rho_{s2}, \rho_{i2}, z) &= C \exp \left[(ik_0/4z) (\rho_{s1}^2 + \rho_{i1}^2 - \rho_{s2}^2 - \rho_{i2}^2) \right] \\
 &\times \exp \left\{ -(\alpha k_0^2/4z^2) [(\rho_{s1} + \rho_{i1})^2 + (\rho_{s2} + \rho_{i2})^2] \right. \\
 &\quad \left. + (\beta k_0^2/2z^2) [(\rho_{s1} + \rho_{i1}) \cdot (\rho_{s2} + \rho_{i2})] \right\}, \quad (3.25)
 \end{aligned}$$

where $C = |A|^2 [(A_p \pi \sigma_s \delta k_0^2) / (2z^2)]^2$; $\rho_{s1} = |\rho_{s1}|$ is the distance from the z -axis of the hole located at \mathbf{r}_{s1} , etc. Since the distances of the holes from the z -axis were assumed to be much smaller than their distances from the crystal, we make the approximation $r_{s1} \approx z + \rho_{s1}^2/2z$, etc. and write $(1/2z)(\rho_{s1}^2 + \rho_{i1}^2 - \rho_{s2}^2 - \rho_{i2}^2) \approx (r_{s1} + r_{i1} - r_{s2} - r_{i2})$. Next, we substitute $r_1 = (r_{s1} + r_{i1})/2$ and $r_2 = (r_{s2} + r_{i2})/2$ and write down $W^{(2)}(\rho_{s1}, \rho_{i1}, \rho_{s2}, \rho_{i2})$ in terms of the two-photon transverse position vectors defined in Eq. (3.15). We then obtain

$$\begin{aligned}
 W^{(2)}(\rho_{s1}, \rho_{i1}, \rho_{s2}, \rho_{i2}, z) &\rightarrow W^{(2)}(\rho_1, \rho_2, z) \\
 &= e^{ik_0(r_1 - r_2)} \sqrt{S^{(2)}(\rho_1, z) S^{(2)}(\rho_2, z)} \mu^{(2)}(\Delta\rho, z) \quad (3.26a)
 \end{aligned}$$

where

$$S^{(2)}(\boldsymbol{\rho}_1, z) = C \exp \left\{ -(1/2) [\boldsymbol{\rho}_1 / \sigma_s^{(2)}(z)]^2 \right\} \quad (3.26b)$$

is the two-photon spectral density in alternative 1, or the coincidence count rate in alternative 1, with

$$\sigma_s^{(2)}(z) = z \sqrt{\sigma_\mu^2 + 4\sigma_s^2 / 2k_0 \sigma_s \sigma_\mu} \quad (3.26c)$$

being the rms correlation width of the two-photon field at plane z ; and where

$$\mu^{(2)}(\Delta\boldsymbol{\rho}, z) = \exp \left\{ -(1/2) [\Delta\boldsymbol{\rho} / \sigma_\mu^{(2)}(z)]^2 \right\}, \quad (3.26d)$$

is the degree of spatial two-photon coherence, with

$$\sigma_\mu^{(2)}(z) = z \sqrt{\sigma_\mu^2 + 4\sigma_s^2 / 2k_0 \sigma_s^2} \quad (3.26e)$$

being the rms spatial coherence width of the two-photon field at plane z . Comparing Eqs. (3.24) and (3.26), we at once find that in terms of the two-photon transverse position vectors, the two-photon cross-spectral density function assumes the same functional form as does the pump cross-spectral density function, in terms of the pump transverse position vectors. Thus, the spatial coherence properties of the pump field get entirely transferred to the spatial coherence properties of the down-converted two-photon field. We note that the functional forms of the two-photon correlation width $\sigma_s^{(2)}(z)$ and the two-photon transverse coherence width $\sigma_\mu^{(2)}(z)$ are the same as those of the pump beam radius $\sigma_s(z)$ and the pump transverse coherence width $\sigma_\mu(z)$, respectively. Thus, the two-photon field seems to propagate as if it were the pump beam with its transverse position vectors given by the two-photon transverse position vectors. Figure 3.3 illustrates the physical interpretation of the two-photon correlation width and the two-photon transverse coherence width.

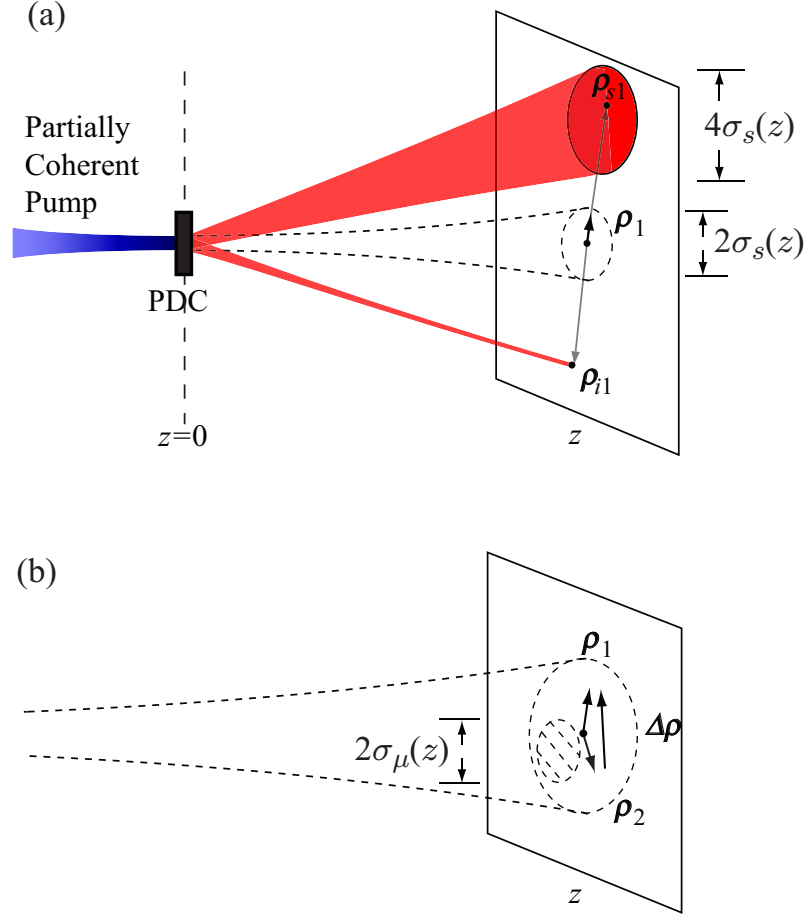


Figure 3.3: Physical interpretation of the two-photon correlation width $\sigma_s^{(2)}(z)$ and the two-photon transverse coherence width $\sigma_\mu^{(2)}(z)$ in terms of the two-photon transverse position vectors. (a) The two-photon correlation width $\sigma_s^{(2)}(z)$ is equal to the pump beam radius $\sigma_s(z)$. As a result, when an idler photon is detected at position $\boldsymbol{\rho}_{i1}$, the corresponding signal photon has an appreciable probability of being detected anywhere inside an area whose center is at $-\boldsymbol{\rho}_{i1}$ and whose radius is twice the pump beam radius $\sigma_s(z)$. (b) The two-photon spatial coherence width $\sigma_\mu^{(2)}(z)$ is equal to the spatial coherence width of the pump field $\sigma_\mu(z)$; thus, for alternatives 1 and 2 of Fig. 3.1 to remain mutually coherent, $|\Delta\boldsymbol{\rho}| = |\boldsymbol{\rho}_1 - \boldsymbol{\rho}_2|$ has to be less than the spatial coherence width $\sigma_\mu(z)$ of the pump field.

The coincidence count rate $R_{si}(\mathbf{r}_s, \mathbf{r}_i)$ of Eq. (3.18a) can now be written as

$$R_{si}(\mathbf{r}_s, \mathbf{r}_i) = k_1^2 S^{(2)}(\boldsymbol{\rho}_1, z) + k_2^2 S^{(2)}(\boldsymbol{\rho}_2, z) + 2k_1 k_2 \sqrt{S^{(2)}(\boldsymbol{\rho}_1, z) S^{(2)}(\boldsymbol{\rho}_2, z) \mu^{(2)}(\Delta\boldsymbol{\rho}, z)} \cos(k_0 \Delta L), \quad (3.27)$$

where we have replaced $\omega_0 t_{s1}$ by $k_0 d_{s1}$, etc. and substituted $l_1 = r_1 + (d_{s1} + d_{i1})/2$, $l_2 = r_2 + (d_{s2} + d_{i2})/2$ and $\Delta L = l_1 - l_2$. Here $l_{1(2)}$ is the two-photon path-length in alternative 1(2) [81]. The visibility V of the two-photon interference fringes is given by

$$V = \frac{2k_1 k_2 \sqrt{S^{(2)}(\boldsymbol{\rho}_1, z) S^{(2)}(\boldsymbol{\rho}_2, z)}}{k_1^2 S^{(2)}(\boldsymbol{\rho}_1, z) + k_2^2 S^{(2)}(\boldsymbol{\rho}_2, z)} \mu^{(2)}(\Delta \boldsymbol{\rho}, z). \quad (3.28)$$

We note that the two-photon cross-spectral density function $W^{(2)}(\boldsymbol{\rho}_{s1}, \boldsymbol{\rho}_{i1}, \boldsymbol{\rho}_{s2}, \boldsymbol{\rho}_{i2}, z)$ and the coincidence count rate $R_{si}(\mathbf{r}_s, \mathbf{r}_i)$ depend on only one displacement parameter, the two-photon transverse position vector, and remain independent of the other displacement parameter, the two-photon position-asymmetry vector. This is a special feature of the degenerate two-photon field. However, in the case of non-degenerate two-photon fields, the two-photon cross-spectral density depends on both the displacement parameters, as we show in the next section.

3.5 Spatial coherence properties of the two-photon field: the general case

In this section, we re-derive the expressions for the two-photon cross-spectral density function $W^{(2)}(\boldsymbol{\rho}_{s1}, \boldsymbol{\rho}_{i1}, \boldsymbol{\rho}_{s2}, \boldsymbol{\rho}_{i2}, z)$ and the coincidence count rate $R_{si}(\mathbf{r}_s, \mathbf{r}_i)$ for the general case. We take down-conversion to be non-degenerate and the thickness of the crystal to be finite. The state of the two-photon field produced by PDC in this case is given by the density matrix ρ_{tp} of Eq. (3.14)

$$\rho_{\text{tp}} = |A|^2 \iiint \int d\mathbf{q}_s d\mathbf{q}_i d\mathbf{q}'_s d\mathbf{q}'_i \langle V(\mathbf{q}_s + \mathbf{q}_i) V^*(\mathbf{q}'_s + \mathbf{q}'_i) \rangle_e e^{i(\Delta q - \Delta q')L/2} \text{sinc}(\Delta q L/2) \text{sinc}(\Delta q' L/2) |\mathbf{q}_s\rangle |\mathbf{q}_i\rangle \langle \mathbf{q}'_s| \langle \mathbf{q}'_i|. \quad (3.29)$$

In writing the above density matrix, we have assumed, as in the last section, that the pump, signal and idler fields are nearly monochromatic. The electric field operators $\hat{E}_{s1}^{(+)}(\mathbf{r}_{s1})$ and $\hat{E}_{i1}^{(+)}(\mathbf{r}_{i1})$ are given as:

$$\hat{E}_{s1}^{(+)}(\mathbf{r}_{s1}) = e^{ik_s z} \int d\mathbf{q} \hat{a}_s(\mathbf{q}) e^{i(\mathbf{q} \cdot \boldsymbol{\rho}_{s1} - q^2 z / 2k_s)}, \quad (3.30)$$

$$\hat{E}_{i1}^{(+)}(\mathbf{r}_{i1}) = e^{ik_i z} \int d\mathbf{q}' \hat{a}_i(\mathbf{q}') e^{i(\mathbf{q}' \cdot \boldsymbol{\rho}_{i1} - q'^2 z / 2k_i)}, \quad (3.31)$$

where ω_s and ω_i are the frequencies of the signal and idler fields, respectively. Using Eqs. (3.29), (3.30), and (3.31), we write the two-photon cross-spectral density of Eq. (3.18b) as:

$$\begin{aligned} W^{(2)}(\boldsymbol{\rho}_{s1}, \boldsymbol{\rho}_{i1}, \boldsymbol{\rho}_{s2}, \boldsymbol{\rho}_{i2}, z) = & \\ & |A|^2 \iiint d\mathbf{q}_s d\mathbf{q}'_s d\mathbf{q}_i d\mathbf{q}'_i \langle V(\mathbf{q}_s + \mathbf{q}_i) V^*(\mathbf{q}'_s + \mathbf{q}'_i) \rangle_e \\ & \times e^{i(\Delta q - \Delta q')L/2} \text{sinc}(\Delta q L/2) \text{sinc}(\Delta q' L/2) e^{i(\mathbf{q}_s \cdot \boldsymbol{\rho}_{s1} - q_s^2 z / 2k_s + \mathbf{q}_i \cdot \boldsymbol{\rho}_{i1} - q_i^2 z / 2k_i)} \\ & \times e^{-i(\mathbf{q}'_s \cdot \boldsymbol{\rho}_{s2} - q_s'^2 z / 2k_s + \mathbf{q}'_i \cdot \boldsymbol{\rho}_{i2} - q_i'^2 z / 2k_i)}. \end{aligned} \quad (3.32)$$

The sinc functions are approximated by Gaussian functions using the following formula: if $\Delta q < 0$, $\text{sinc}(\Delta q L/2) \approx \exp[-c_0 \sqrt{|\Delta q|}^2 L/2]$, where $c_0 = 0.455$ [132]. In replacing the sinc functions by their Gaussian approximations, we note that $\Delta q = q_p^2/2k_p - q_s^2/2k_s - q_i^2/2k_i$ and $\Delta q' = q_p'^2/2k_p - q_s'^2/2k_s - q_i'^2/2k_i$ are negative quantities. We now evaluate the two-photon cross-spectral density function, which after a very

long but straightforward calculation can be shown to be

$$\begin{aligned}
W^{(2)}(\boldsymbol{\rho}_{s1}, \boldsymbol{\rho}_{i1}, \boldsymbol{\rho}_{s2}, \boldsymbol{\rho}_{i2}, z) &= \frac{|A|^2 (4\pi A_p \sigma_s \delta k_s k_i)^2}{[(2z + L)^2 + c_0^2 L^2] [z^2 + 4k_p^2(\alpha^2 - \beta^2)]} \\
&\times \exp \left\{ -\frac{2\alpha k_p - iz}{2k_p [z^2 + 4k_p^2(\alpha^2 - \beta^2)]} (k_s \boldsymbol{\rho}_{s1} + k_i \boldsymbol{\rho}_{i1})^2 \right\} \\
&\times \exp \left\{ \frac{ik_s k_i}{k_p} \frac{(2z + L + ic_0 L)}{[(2z + L)^2 + c_0^2 L^2]} (\boldsymbol{\rho}_{s1} - \boldsymbol{\rho}_{i1})^2 \right\} \\
&\times \exp \left\{ -\frac{2\alpha k_p + iz}{2k_p [z^2 + 4k_p^2(\alpha^2 - \beta^2)]} (k_s \boldsymbol{\rho}_{s2} + k_i \boldsymbol{\rho}_{i2})^2 \right\} \\
&\times \exp \left\{ -\frac{ik_s k_i}{k_p} \frac{(2z + L - ic_0 L)}{[(2z + L)^2 + c_0^2 L^2]} (\boldsymbol{\rho}_{s2} - \boldsymbol{\rho}_{i2})^2 \right\} \\
&\times \exp \left\{ \frac{2\beta}{[z^2 + 4k_p^2(\alpha^2 - \beta^2)]} (k_s \boldsymbol{\rho}_{s1} + k_i \boldsymbol{\rho}_{i1}) \cdot (k_s \boldsymbol{\rho}_{s2} + k_i \boldsymbol{\rho}_{i2}) \right\}. \quad (3.33)
\end{aligned}$$

We restrict ourselves to the far field and use the following far-field approximations: $z^2/4k_p^2 \gg (\alpha^2 - \beta^2)$ and $z \gg L$. The first of the two approximation is the standard Fraunhofer approximation [133]. Equation (3.33) now reduces to a much simplified form

$$\begin{aligned}
W^{(2)}(\boldsymbol{\rho}_{s1}, \boldsymbol{\rho}_{i1}, \boldsymbol{\rho}_{s2}, \boldsymbol{\rho}_{i2}, z) &= \\
&|A|^2 (2\pi A_p \sigma_s \delta k_s k_i / z^2)^2 \exp \left[(i/2z) (k_s \rho_{s1}^2 + k_i \rho_{i1}^2 - k_s \rho_{s2}^2 - k_i \rho_{i2}^2) \right] \\
&\times \exp \left\{ -(\alpha/z^2) [(k_s \boldsymbol{\rho}_{s1} + k_i \boldsymbol{\rho}_{i1})^2 + (k_s \boldsymbol{\rho}_{s2} + k_i \boldsymbol{\rho}_{i2})^2] \right. \\
&\quad \left. + (2\beta/z^2) [(k_s \boldsymbol{\rho}_{s1} + k_i \boldsymbol{\rho}_{i1}) \cdot (k_s \boldsymbol{\rho}_{s2} + k_i \boldsymbol{\rho}_{i2})] \right. \\
&\quad \left. - [k_s k_i c_0 L / (4k_p z^2)] [(\boldsymbol{\rho}_{s1} - \boldsymbol{\rho}_{i1})^2 + (\boldsymbol{\rho}_{s2} - \boldsymbol{\rho}_{i2})^2] \right\}. \quad (3.34)
\end{aligned}$$

We substitute $k_0 = (k_s + k_i)$ and $k_d = (k_s - k_i)/2$, and writing $r_{s1} \approx z + \rho_{s1}^2/2z$, etc., we substitute $r'_1 = r_{s1} - r_{i1}$ and $r'_2 = r_{s2} - r_{i2}$. Next, substituting for α and β from Eq. (3.23), we write Eq. (3.34) in terms of the two displacement parameters defined

in Eq. (3.15):

$$W^{(2)}(\boldsymbol{\rho}_1, \boldsymbol{\rho}'_1, \boldsymbol{\rho}_2, \boldsymbol{\rho}'_2, z) = e^{i[k_0(r_1-r_2)+k_d(r'_1-r'_2)]} \\ \times \sqrt{S^{(2)}(\boldsymbol{\rho}_1, \boldsymbol{\rho}'_1, z)S^{(2)}(\boldsymbol{\rho}_2, \boldsymbol{\rho}'_2, z)\mu^{(2)}(\Delta\boldsymbol{\rho}, \Delta\boldsymbol{\rho}', z)} \quad (3.35a)$$

where

$$S^{(2)}(\boldsymbol{\rho}_1, \boldsymbol{\rho}'_1, z) = \\ C_1 \exp \left\{ -[2\sigma_s^2\sigma_\mu^2/z^2(\sigma_\mu^2 + 4\sigma_s^2)](k_0\boldsymbol{\rho}_1 + k_d\boldsymbol{\rho}'_1)^2 - [(k_0^2 - 4k_d^2)c_0L/(8k_0z^2)](\boldsymbol{\rho}'_1)^2 \right\} \quad (3.35b)$$

is the two-photon spectral density in alternative 1 with $C_1 = |A|^2\{[A_p\pi\sigma_s\delta(k_0^2 - 4k_d^2)]/(2z^2)\}^2$, and where

$$\mu^{(2)}(\Delta\boldsymbol{\rho}, \Delta\boldsymbol{\rho}', z) = \exp \left\{ -[2\sigma_s^4/z^2(\sigma_\mu^2 + 4\sigma_s^2)](k_0\Delta\boldsymbol{\rho} + k_d\Delta\boldsymbol{\rho}')^2 \right\} \quad (3.35c)$$

is the degree of spatial two-photon-coherence. The coincidence count rate $R_{si}(\mathbf{r}_s, \mathbf{r}_i)$ of Eq. (3.18a) can now be shown to be

$$R_{si}(\mathbf{r}_s, \mathbf{r}_i) = k_1^2 S^{(2)}(\boldsymbol{\rho}_1, \boldsymbol{\rho}'_1, z) + k_2^2 S^{(2)}(\boldsymbol{\rho}_2, \boldsymbol{\rho}'_2, z) \\ + 2k_1k_2 \sqrt{S^{(2)}(\boldsymbol{\rho}_1, \boldsymbol{\rho}'_1, z)S^{(2)}(\boldsymbol{\rho}_2, \boldsymbol{\rho}'_2, z)\mu^{(2)}(\Delta\boldsymbol{\rho}, \Delta\boldsymbol{\rho}', z)} \cos(k_0\Delta L + k_d\Delta L'), \quad (3.36)$$

where we have substituted $\omega_0 = (\omega_s + \omega_i)$ and $\omega_d = (\omega_s - \omega_i)/2$, and have replaced $\omega_0 t_{s1}$ by $k_0 d_{s1}$ and $\omega_d t_{s1}$ by $k_d d_{s1}$, etc. We have also substituted $l_1 = r_1 + (d_{s1} + d_{i1})/2$, $l_2 = r_2 + (d_{s2} + d_{i2})/2$; $l'_1 = r'_1 + (d_{s1} - d_{i1})$, $l'_2 = r'_2 + (d_{s2} - d_{i2})$; and $\Delta L = l_1 - l_2$ and $\Delta L' = l'_1 - l'_2$. Here $l'_{1(2)}$ is the two-photon path-asymmetry length in alternative 1(2) [81]. We note that the finite thickness of the crystal affects only the two-photon spectral densities in the two alternatives and has no effect on the degree of spatial two-photon-coherence, which has the same functional form as that of the degree of

spatial coherence of the pump field. The visibility V of two-photon interference fringes is given by

$$V = \frac{2k_1 k_2 \sqrt{S^{(2)}(\boldsymbol{\rho}_1, \boldsymbol{\rho}'_1, z) S^{(2)}(\boldsymbol{\rho}_2, \boldsymbol{\rho}'_2, z)}}{k_1^2 S^{(2)}(\boldsymbol{\rho}_1, \boldsymbol{\rho}'_1, z) + k_2^2 S^{(2)}(\boldsymbol{\rho}_2, \boldsymbol{\rho}'_2, z)} \mu^{(2)}(\Delta\boldsymbol{\rho}, \Delta\boldsymbol{\rho}', z). \quad (3.37)$$

3.6 Position-momentum entanglement

Two-photon coherence in the spatial domain is interrelated with entanglement in the position-momentum degree of freedom. The simple meaning of position-momentum entanglement is that the two photons become simultaneously correlated in their positions and momenta. As a consequence, by measuring either the position or the momentum of one of the two photons, either the position or the momentum, respectively, of the other photon can be inferred, in principle, with complete certainty [94]. This fact that the non-commuting observables, position and momentum, could be known with more certainty than is allowed by the uncertainty principle forms the core of the EPR paradox [17].

Position-momentum entanglement in the original EPR sense was demonstrated by Howell *et al.* in 2004 [94]. Using the signal and idler photons produced by type-II parametric down-conversion, Howell *et al.* measured the position and momentum correlations by making measurement in the near and far fields of the emitted photons. The measured two-photon position-momentum variance product was shown to violate the bound for the EPR and the separability criteria [134]. The first conclusive verification of position-momentum entanglement through the violation of a Bell inequality was reported by Yarnall *et al.* [66]. In their experiment, Yarnall *et al.* mapped the infinite dimensional Hilbert space of transverse momentum onto a two-dimensional space of spatial parity, thereby making an entangled two-qubit state in spatial-parity space. A violation of CHSH-Bell inequality was then demonstrated in this spatial-parity space.

Position-momentum entanglement of the down-converted photons has been exploited for preparing entangled states that could be used in quantum information based applications [25, 26, 27]. Utilizing either the position or the momentum correlations of the down-converted photons, several research groups have reported experimental demonstrations of entangled two-qudit states. Neves *et al.* [135, 136, 137] have used the position correlations to prepare entangled two-qudit states with $d = 4$ and 8. In their scheme, they employed apertures with d -slits to define the qudit space and placed them along the paths of the signal and idler photons. O’Sullivan *et al.* [138] have demonstrated another scheme, utilizing also the position correlations, to prepare two-qudit states with $d = 3$ and 6. In their scheme, each of the down-converted photons is mapped onto a set of discrete regions of space, which they refer to as ‘pixels’. These pixels, which are defined by the input facets of multi-mode optical fibers, form the qudit space for each photon.

3.7 Spatial two-photon coherence and entanglement of spatial two-qubit states

In the pervious sections, we discussed how the spatial coherence properties of the two-photon field propagate and how they depend on the spatial coherence properties of the pump field. In this section, we study the connection between the degree of spatial two-photon-coherence and the degree of entanglement of two-qubit states that are based on the spatial correlations of the position-momentum entangled photons. We limit our analysis in this section to the case of degenerate down-conversion only.

Two-qubit states are very important for quantum information technology, as they are the necessary ingredients for many quantum information based applications, such as quantum cryptography [25], quantum dense coding [26], and quantum teleportation [27]. Position-momentum entanglement of the down-converted photons has been exploited in several ways for preparing entangled two-qubit states (two-qudit states

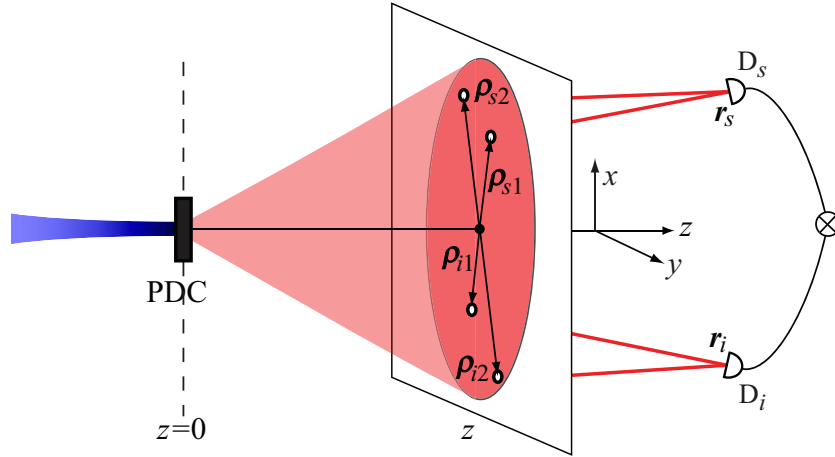


Figure 3.4: A generic scheme to prepare spatial two-qubit states. The phase-matching conditions and the coherence properties of the pump field are adjusted in such a way that there are only two alternative pathways, with nonzero probabilities, by which the signal and idler photons can reach detectors D_s and D_i . The state of the two photons after the double-hole aperture is then represented by the density matrix ρ_{qubit} of Eq. (3.38).

in general) [136, 138, 139, 140], by utilizing either the position or the momentum correlations of the entangled photons. When position correlations are used for the purpose, the prepared qubit states are referred to as spatial two-qubit states. Entanglement of the spatial two-qubit states are quite often quantified by an entanglement measure called concurrence [76, 77]. In what follow we establish a precise relationship between the degree of spatial two-photon-coherence and the entanglement of spatial two-qubit states. We derive an explicit relationship showing how the entanglement of a spatial two-qubit state gets affected by the spatial coherence properties of the two-photon field, and in turn by the spatial coherence properties of the pump field. We restrict our analysis to the class of two-qubit states that can be represented by a density matrix having only two non-zero diagonal elements.

A generic scheme for preparing spatial two-qubit states is depicted in Fig. 3.4. The states prepared by both Neves *et al.* [135, 136] and O’Sullivan *et al.* [138] can be analyzed using this generic scheme. In this scheme, position-momentum entangled photons are each made to pass through a double-hole. Thus $\{|s1\rangle, |s2\rangle\}$ and

$\{|i1\rangle, |i2\rangle\}$ form the two-dimensional orthonormal bases for the signal and idler photons, respectively, where $|s1\rangle$ represents the state of the signal photon passing through the hole located at transverse position $\boldsymbol{\rho}_{s1}$, etc. The four-dimensional basis set for the two-qubit state can then be represented by $\{|s1\rangle|i1\rangle, |s1\rangle|i2\rangle, |s2\rangle|i1\rangle, |s2\rangle|i2\rangle\}$, where $|s1\rangle|i1\rangle$ represents the joint state of the signal and idler photons when the signal photon passes through the hole located at $\boldsymbol{\rho}_{s1}$ and the idler photon passes through the hole located at $\boldsymbol{\rho}_{i1}$, etc.

We now make an explicit assumption that the probabilities of finding the signal and idler photons in states $|s1\rangle|i2\rangle$ and $|s2\rangle|i1\rangle$ are negligibly small. In an experiment, this can be ensured by keeping the separations between the two signal and the two idler holes to be much bigger than the two-photon correlation width so that the two-photon spectral densities for the pairs of transverse positions $(\boldsymbol{\rho}_{s1}, \boldsymbol{\rho}_{i2})$ and $(\boldsymbol{\rho}_{s2}, \boldsymbol{\rho}_{i1})$ are negligibly small. With the above assumption, the density matrix ρ_{qubit} of the two-qubit state thus prepared can be written in the basis $\{|s1\rangle|i1\rangle, |s1\rangle|i2\rangle, |s2\rangle|i1\rangle, |s2\rangle|i2\rangle\}$ as:

$$\rho_{\text{qubit}} = \begin{pmatrix} a & 0 & 0 & c \\ 0 & 0 & 0 & 0 \\ 0 & 0 & 0 & 0 \\ d & 0 & 0 & b \end{pmatrix}. \quad (3.38)$$

where a and b are the probabilities that the signal and idler photons are detected in states $|s1\rangle|i1\rangle$ and $|s2\rangle|i2\rangle$, respectively, with $a + b = 1$; the probabilities that the signal and idler photons are detected in states $|s1\rangle|i2\rangle$ and $|s2\rangle|i1\rangle$ are zero. The off-diagonal term c is a measure of coherence between states $|s1\rangle|i1\rangle$ and $|s2\rangle|i2\rangle$, with $c = d^*$. From our studies in Sections 3.4 and 3.5, we find that the probability a of detecting the signal and idler photons in state $|s1\rangle|i1\rangle$ is proportional to the two-photon spectral density $S^{(2)}(\boldsymbol{\rho}_1, z)$, where $\boldsymbol{\rho}_1 = (\boldsymbol{\rho}_{s1} + \boldsymbol{\rho}_{i1})/2$ is the two-photon transverse position vector for the pair of points $\boldsymbol{\rho}_{s1}$ and $\boldsymbol{\rho}_{i1}$. Similarly, the probability

b of detecting the signal and idler photons in state $|s2\rangle|i2\rangle$ is proportional to the two-photon spectral density $S^{(2)}(\boldsymbol{\rho}_2, z)$, where $\boldsymbol{\rho}_2 = (\boldsymbol{\rho}_{s2} + \boldsymbol{\rho}_{i2})/2$ is the two-photon transverse position vector for the pair of points $\boldsymbol{\rho}_{s2}$ and $\boldsymbol{\rho}_{i2}$. Thus, we write

$$a = \eta k_1^2 S^{(2)}(\boldsymbol{\rho}_1, z) \quad \text{and} \quad (3.39)$$

$$b = \eta k_2^2 S^{(2)}(\boldsymbol{\rho}_2, z), \quad (3.40)$$

where $\eta = 1/[k_1^2 S^{(2)}(\boldsymbol{\rho}_1, z) + k_2^2 S^{(2)}(\boldsymbol{\rho}_2, z)]$ is the constant of proportionality. Further, we find that the off-diagonal term c , which is a measure of coherence between the two-photon states $|s1\rangle|i1\rangle$ and $|s2\rangle|i2\rangle$, is proportional to the two-photon cross-spectral density $W^{(2)}(\boldsymbol{\rho}_1, \boldsymbol{\rho}_2, z) \equiv W^{(2)}(\boldsymbol{\rho}_{s1}, \boldsymbol{\rho}_{i1}, \boldsymbol{\rho}_{s2}, \boldsymbol{\rho}_{i2}, z)$ at the two pairs of transverse positions $(\boldsymbol{\rho}_{s1}, \boldsymbol{\rho}_{i1})$ and $(\boldsymbol{\rho}_{s2}, \boldsymbol{\rho}_{i2})$, that is,

$$c = d^* = \eta k_1 k_2 W^{(2)}(\boldsymbol{\rho}_1, \boldsymbol{\rho}_2, z). \quad (3.41)$$

We now quantify the entanglement of the two-qubit state represented by the density matrix ρ_{qubit} . The entanglement of a general two-qubit state can be characterized in terms of Wootters's concurrence [76, 77], which ranges from 0 to 1, with 1 corresponding to the maximally-entangled two-qubit state and 0 to a non-entangled state. For a given two-qubit density matrix ρ , the concurrence $C(\rho)$ is given by $C(\rho) = \max\{0, \sqrt{\lambda_1} - \sqrt{\lambda_2} - \sqrt{\lambda_3} - \sqrt{\lambda_4}\}$. Here the λ_i s are the eigenvalues, in descending order, of matrix $\zeta = \rho(\sigma_y \otimes \sigma_y)\rho^*(\sigma_y \otimes \sigma_y)$, with $\sigma_y = \begin{pmatrix} 0 & -i \\ i & 0 \end{pmatrix}$ being the usual Pauli operator and ρ^* the complex conjugate of ρ . For the density matrix ρ_{qubit} ,

the matrix ζ becomes

$$\zeta = \begin{pmatrix} ab + cd & 0 & 0 & 2ac \\ 0 & 0 & 0 & 0 \\ 0 & 0 & 0 & 0 \\ 2bd & 0 & 0 & ab + cd \end{pmatrix}. \quad (3.42)$$

The eigenvalues of ζ in descending order are:

$$\begin{aligned} \lambda_1 &= (\sqrt{ab} + \sqrt{cd})^2, \\ \lambda_2 &= (\sqrt{ab} - \sqrt{cd})^2, \\ \lambda_3 &= 0 \text{ and} \\ \lambda_4 &= 0. \end{aligned} \quad (3.43)$$

As $c = d^*$, the eigenvalues of ζ can be written as

$$\begin{aligned} \lambda_1 &= (\sqrt{ab} + |c|)^2, \\ \lambda_2 &= (\sqrt{ab} - |c|)^2, \\ \lambda_3 &= 0 \text{ and} \\ \lambda_4 &= 0. \end{aligned} \quad (3.44)$$

Thus, the concurrence $C(\rho_{\text{qubit}}) = \max\{0, \sqrt{\lambda_1} - \sqrt{\lambda_2} - \sqrt{\lambda_3} - \sqrt{\lambda_4}\}$ is given by

$$C(\rho_{\text{qubit}}) = 2|c| = \frac{2k_1 k_2 |W^{(2)}(\boldsymbol{\rho}_1, \boldsymbol{\rho}_2, z)|}{k_1^2 S^{(2)}(\boldsymbol{\rho}_1, z) + k_2^2 S^{(2)}(\boldsymbol{\rho}_2, z)}. \quad (3.45)$$

We thus find that for a spatial two-qubit state, concurrence is proportional to the magnitude of the two-photon cross-spectral density at the two pairs of transverse positions that define the two-qubit state. Using Eq. (3.26a), we rewrite the above

expression as

$$C(\rho_{\text{qubit}}) = \frac{2k_1k_2\sqrt{S^{(2)}(\boldsymbol{\rho}_1, z)S^{(2)}(\boldsymbol{\rho}_2, z)}}{k_1^2S^{(2)}(\boldsymbol{\rho}_1, z) + k_2^2S^{(2)}(\boldsymbol{\rho}_2, z)}\mu^{(2)}(\Delta\boldsymbol{\rho}, z). \quad (3.46)$$

Comparing the above equation with Eq. (3.28), we at once see that the quantity on the right hand side of the above equation is the far-field visibility V of two-photon interference fringes produced by the pair of double holes. This implies that for a two-qubit state that has only two non-zero diagonal elements, entanglement can be characterized using a single experimentally measurable quantity. In the special case in which $S^{(2)}(\boldsymbol{\rho}_1, z) = S^{(2)}(\boldsymbol{\rho}_2, z)$ and $k_1 = k_2$, we get

$$C(\rho_{\text{qubit}}) = \mu^{(2)}(\Delta\boldsymbol{\rho}, z); \quad (3.47)$$

that is, when the two-photon spectral densities at $\boldsymbol{\rho}_1$ and $\boldsymbol{\rho}_2$ are equal and when the diffracted intensities in the two alternatives are also equal, concurrence becomes equal to the degree of spatial two-photon-coherence. Since the degree of spatial two-photon-coherence depends on the degree of spatial coherence of the pump field, we find that the maximum achievable entanglement of a spatial two-qubit state is bounded by the degree of spatial coherence of the pump field. The results presented in this chapter are reported in Ref. [141].

3.8 Summary

In summary, we have studied the spatial coherence properties of the two-photon field produced by parametric down-conversion when the pump field producing PDC is, spatially, a partially coherent beam of Gaussian Schell-model type. We have constructed two displacement parameters using the transverse position vectors of the signal and idler photons in two interfering alternatives. In terms of these parameters, we have described two-alternative spatial two-photon interference and have shown

that in PDC the spatial coherence properties of the pump field get entirely transferred to the spatial coherence properties of the down-converted two-photon field. We have then analyzed the connection between the degree of spatial two-photon-coherence and entanglement of two-qubit states that are based on the spatial correlations of the position-momentum entangled photons. We have shown that the concurrence of a spatial two-qubit state is proportional to the magnitude of the two-photon cross-spectral density at the two pairs of transverse positions that define the two-qubit state. Further, we have shown that for such states the maximum achievable entanglement is bounded by the degree of spatial coherence of the pump field and that it can therefore be tailored by controlling the spatial coherence properties of the pump field.

It has been recently shown that spatially partially coherent beams are less affected by atmospheric turbulence than are spatially fully coherent beams [142, 143, 144]. In light of the results presented in this chapter, it then follows, at least intuitively, that the entangled two-photon field produced by using a partially coherent pump beam will be less susceptible to atmospheric turbulence than will the entangled two-photon field produced by using a fully coherent pump beam. This may have important implications for many quantum-information based real-world applications.

Chapter 4

Two-Photon Coherence Effects: Angular

4.1 Introduction

In recent years, much attention has been devoted to studying the orbital angular momentum (OAM) of light beams [44, 45, 48, 49, 50, 145], and to studying and characterizing the OAM-entanglement of the down-converted two-photon fields [22, 146, 147, 148, 149, 150, 151, 152]. In particular, it has been shown that angular position and orbital angular momentum form Fourier pairs [44, 45, 46]. The existence of such a Fourier relationship gives rise to angular interference—interference in the distribution of OAM modes of a photon field when it passes through an angular aperture [45, 49, 50]. The angular Fourier relationship in the context of angular-position–OAM entanglement leads to what is known as the angular EPR paradox [153].

Entanglement in angular-position–OAM degree of freedom gives rise to two-photon interference in the angular domain, which is the subject of the present chapter. In this chapter, we also report experimental demonstrations of two-qubit states that are based on the angular-position correlations of entangled photons. Entangled two-qubit

states are the essential ingredient for many quantum information based applications, such as quantum cryptography [25], quantum dense coding [26], and quantum teleportation [27].

The chapter is organized as follows. Section 4.2 describes beams that carry well-defined orbital angular momentum. The angular Fourier relationship is described in Section 4.3. Sections 4.4 and 4.5 discuss, respectively, the conservation of orbital angular momentum in parametric down-conversion and the angular-position–OAM entanglement of the down-converted photons. In Sections 4.6 and 4.7, we describe our studies of angular two-photon interference and present a new method of preparing entangled two-qubit states. Section 4.8 contains the summary.

4.2 Orbital angular momentum of light

In 1936 Beth [154] made the first observation of the spin angular momentum of photons. In his experiment, a right circularly polarized light was passed through a birefringence plate that transformed it into a left circularly polarized light. A $2\hbar$ of spin angular momentum per photon was found to have been transferred to the birefringence plate. In 1992, Allen *et al.* showed that a light beam with a Laguerre-Gaussian amplitude distribution carries a well-defined orbital angular momentum [48]. The field amplitude $\psi_{pl}(\rho, \phi, z)$ of a Laguerre-Gaussian mode is given by

$$\psi_{pl}(\rho, \phi, z) = \frac{C}{(1 + z^2/z_R^2)^{1/2}} \exp \left[i(2p + l + 1) \tan^{-1} \left(\frac{z}{z_R} \right) \right] \left[\frac{\rho/2}{w(z)} \right]^l L_p^l \left[\frac{2\rho^2}{w^2(z)} \right] \times \exp \left[-\frac{\rho^2}{w^2(z)} \right] \exp \left[-\frac{ik^2\rho^2 z}{2(z^2 + z_R^2)} \right] e^{-il\phi}, \quad (4.1)$$

where C is a constant, k the wave-vector magnitude of the field, Z_R the Rayleigh range, and $w(z)$ the radius of the beam at $z = 0$. L_p^l is the associated Laguerre

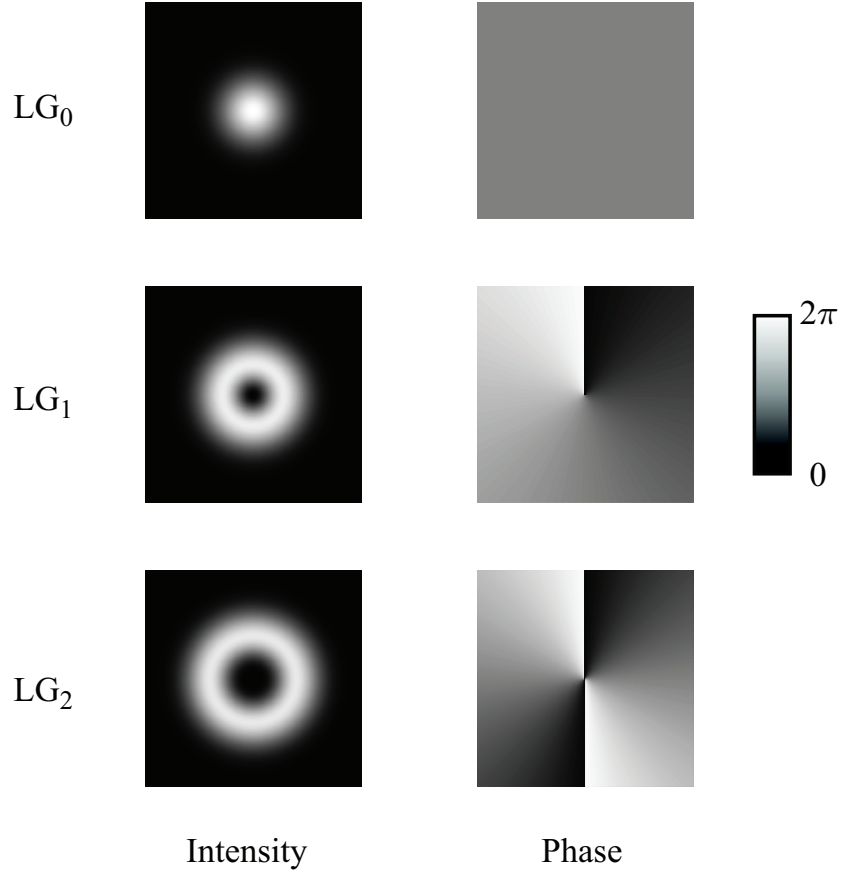


Figure 4.1: The intensity and phase patterns of the first three Laguerre-Gaussian modes: LG₀, LG₁, and LG₂. The scales on the intensity plots are arbitrary, whereas the scales on the phase plots go from 0 to 2π , as shown.

polynomial given by

$$L_p^l(x) = \sum_{m=0}^p (-1)^m C_{p-m}^{p+l} \frac{x^m}{m!}, \quad (4.2)$$

with $C_k^n = \frac{n!}{k!(n-k)!}$. The amplitude of a Laguerre-Gaussian (LG) mode has an azimuthal phase dependence $e^{-il\phi}$, where l is called the azimuthal mode index. Allen *et al.* showed that a Laguerre-Gaussian mode with index l possesses an orbital angular momentum of $l\hbar$ per photon. Although Laguerre-Gaussian modes are, in general, characterized using two indices, l and p , in what follows we consider only those LG

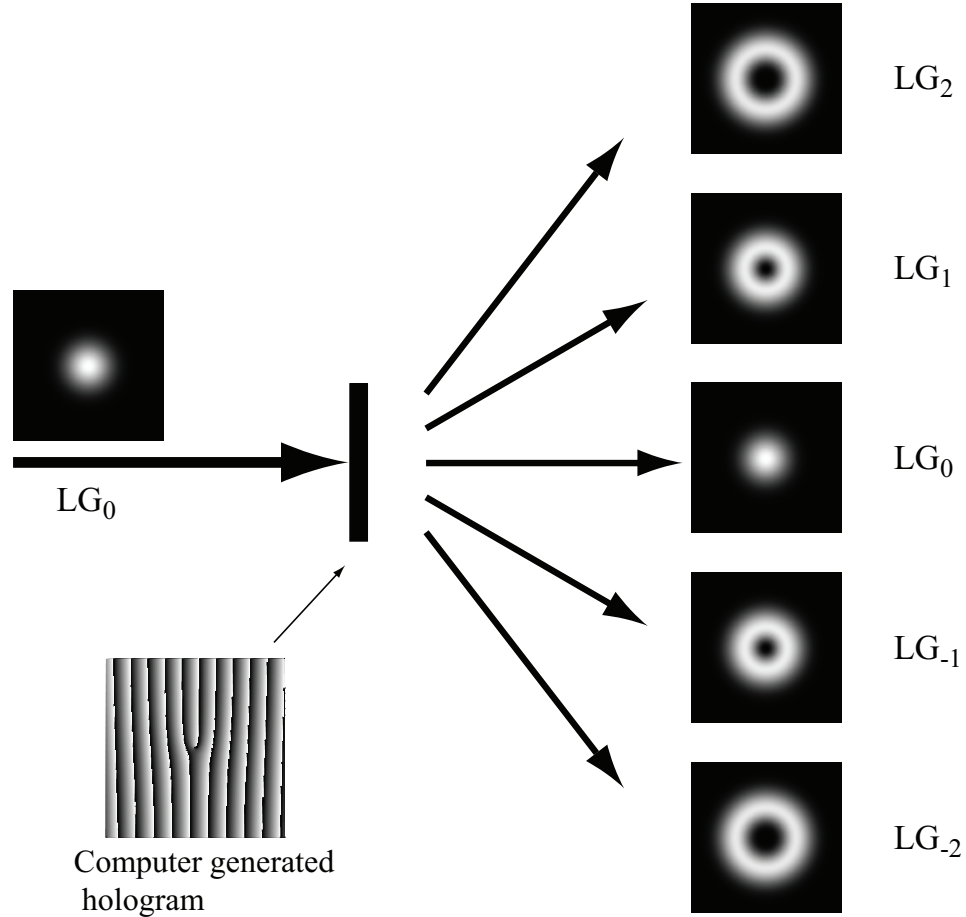


Figure 4.2: Schematic of the method used to generate Laguerre-Gaussian (LG) beams using a computer generated hologram. The phase pattern of the computer generated hologram contains a phase grating and an azimuthal phase $e^{-il\phi}$, with $l = 1$. When a Gaussian beam (LG_0) falls on such a hologram, it gets diffracted into many different orders. In the 0th diffraction order, a beam with original phase and intensity structure is obtained. In the ± 1 diffraction order, $LG_{\pm 1}$ beam is obtained. Similarly in ± 2 diffraction order, $LG_{\pm 2}$ beam is obtained, and so on.

modes that have $p = 0$. So in the rest of this chapter, we shall drop the index p while writing LG modes and show the index l alone. Figure 4.1 shows the intensity and phase patterns of the first three LG modes: LG_0 , LG_1 and LG_2 .

Light beams carrying orbital angular momentum are now routinely produced. There are many methods that are currently being employed to produce such beams. One method is based on using the so-called spiral-phase plates [47], and the other is

based on using the computer generated holograms [147]. Both these methods have their own advantages. Whereas the spiral-phase-plate method is more efficient, the computer generated holograms are easier to implement in experiments. One other method is using stress birefringence [155]. Figure 4.2 depicts the schematic of a method used to generate LG beams using computer generated holograms.

4.3 Angular Fourier relationship

Just as position and linear momentum of a photon form Fourier pairs, a photon's angular position and orbital angular momentum (OAM) form Fourier pairs [44, 45, 46]. The Fourier relationship is

$$\psi_l = \frac{1}{\sqrt{2\pi}} \int_{-\pi}^{\pi} d\phi \Psi(\phi) \exp(-il\phi), \quad (4.3)$$

$$\Psi(\phi) = \frac{1}{\sqrt{2\pi}} \sum_{l=-\infty}^{+\infty} \psi_l \exp(il\phi). \quad (4.4)$$

Here ψ_l , which represent the field amplitude of an LG mode of azimuthal index l , is the probability amplitude that the photon field is carrying orbital angular momentum $l\hbar$, while $\Psi(\phi)$ is the probability amplitude that the angular position of the photon is angle ϕ . The form of this angular Fourier relationship is different from what one obtains for position and linear momentum. This is because of the fact that both position and linear momentum are unbounded and continuous variables, whereas angle is 2π periodic and orbital angular momentum unbounded and discrete. Nevertheless, because of the angular Fourier relationship, interference effects are observed in the distribution of the OAM-mode distribution of a photon field when it passes through an angular aperture [49, 50].

Angular Fourier relationship has been verified in several experiments [49, 50]. More recently, we have demonstrated angular Fourier relationship using the down-converted signal and idler photons [50]. In our experiments, we have demonstrated

that an angular aperture placed in the signal photon-path causes angular interference in the OAM-mode distribution of the idler photons.

4.4 Conservation of orbital angular momentum in down-conversion

The homogeneity in time, or the time translational invariance, leads to conservation of energy. Similarly, the homogeneity in space, or the space translational invariance, leads to the conservation of linear momentum [156]. In the same way, the rotational invariance leads to the conservation of orbital angular momentum. In the context of parametric down-conversion, energy and momentum conservation laws are always valid. However, due to the anisotropy of the nonlinear crystal involved in parametric down-conversion, there has been a debate as to whether in PDC orbital angular momentum remains conserved or not. Most workers have pointed out that orbital angular momentum remains conserved in PDC [22, 148, 149, 152, 157], and they have attributed the conservation either to the phase-matching in the nonlinear crystal [148] or to the transfer of the plane-wave spectrum from the pump beam to the down-converted field [149]. However, there are others who hold contrary views [146, 158]. A recent paper by Feng and Kumar [159] has tried to settle the controversy. It is now generally believed that in type-I down-conversion with nearly collinear configurations, OAM is conserved, whereas in type-II down-conversion, orbital angular is not completely conserved.

The first experimental demonstration of the conservation of orbital angular momentum was reported by Mair *et al.* [147]. In their experiment, the down-converted photons were produced with type-I phase-matching condition. Pump beams with different orbital angular momenta ($\hbar l_p$) were used, and for each $\hbar l_p$, orbital angular momenta of the signal ($\hbar l_s$) and idler ($\hbar l_i$) photons were measured using computer generated holograms. It was found that for every set of measured values of l_p , l_s and

l_i , the OAM of the pump photon was equal to the sum of the OAMs of the signal and idler photons, that is, $\hbar l_p = \hbar l_s + \hbar l_i$. Thus the conservation of orbital angular momentum in PDC was confirmed.

4.5 Angular-position–orbital-angular-momentum entanglement

The conservation of orbital angular momentum in parametric down-conversion leads to entanglement of the signal and idler photons in angular-position–OAM degree of freedom. An EPR-type interpretation of angular-position–OAM entanglement was presented by Götte *et al.* in their work entitled “angular EPR paradox [153].”

Angular-position–OAM entanglement of the down-converted photons have been verified in many experiments. The first such demonstration was reported by Vaziri *et al.* [22], who showed a violation of a generalized CHSH-type Bell inequality [73] in three dimensions by more than 18 standard deviations. More recently, Leach *et al.* [68] have demonstrated OAM entanglement through violations of CHSH-Bell inequalities in a number of two-dimensional subspaces. Using non-integer spiral phase plates, Oemrawsingh *et al.* have also demonstrated OAM entanglement, although not through a Bell-inequality violation [151, 160].

The angular-position–OAM entanglement of the down-converted photons has also been exploited for preparing entangled two-qudit states for use in quantum information protocols. In 2004, Langford *et al.* demonstrated an entangled two-qutrit state that was based on the OAM correlations of down-converted photons [161]. Leach *et al.* have also utilized the OAM correlations of down-converted photons to prepare entangled two-qubit states [68]. Recently, we reported experimental demonstrations of two-qubit states that was based on the angular-position correlations of down-converted photons [162]. In our experiment, the two-qubit state was prepared by using apertures in the form of double angular-slits, and the state was characterized

through separate measurements in the angular position and orbital angular momentum bases. The degree of entanglement of the state was quantified by evaluating its concurrence.

4.6 Angular two-qubit states and two-photon angular interference

Two-qubit states are, in general, prepared by exploiting correlations of the entangled photons in one of the variables. Such states have been realized by exploring correlations in several variables: polarization [99, 163], time-bin [95, 164], frequency [67], position [135, 136], transverse momentum [21, 138], and OAM [22, 68, 161]; however, to date, the angular-position correlations of the entangled photons have not been utilized for preparing entangled two-qubit states. In this and the next sections, we describe our studies related to angular two-photon interference and our experimental demonstrations of angular two-qubit states.

Let us consider the situation shown in Fig. 4.3(a). A Gaussian pump beam produces signal and idler photons by type-I degenerate PDC with non-collinear phase matching. The state $|\psi_{\text{tp}}\rangle$ of the down-converted two-photon field is given by [148, 149]:

$$|\psi_{\text{tp}}\rangle = \sum_{l=-\infty}^{\infty} c_l |l\rangle_s | -l\rangle_i. \quad (4.5)$$

Here s and i stand for signal and idler respectively; and $|l\rangle$ represents an OAM eigenmode of order l , corresponding to an azimuthal phase $e^{-il\phi}$. $|c_l|^2$ is the probability that the signal and idler photons are generated in modes of order l and $-l$, respectively. The width of the mode probability distribution is referred to as the spiral bandwidth of the two-photon field, which depends on the nonlinear crystal and pump beam parameters [152]. In an experimental situation, the observed bandwidth also

depends on, and is often limited by, the finite numerical aperture of the detection system.

The signal and idler photons are made to pass through double angular-slits [as shown in Fig. 4.3(a)] located in the image planes of the crystal. The amplitude transmission functions of the individual angular-slits are given by

$$A_{ja}(\phi_j) = \begin{cases} 1 & \text{if } -\alpha/2 < \phi_j < \alpha/2, \\ 0 & \text{otherwise;} \end{cases} \quad (4.6)$$

$$A_{jb}(\phi_j) = \begin{cases} 1 & \text{if } \beta - \alpha/2 < \phi_j < \beta + \alpha/2, \\ 0 & \text{otherwise,} \end{cases} \quad (4.7)$$

where $j = s, i$. There are in principle four alternative pathways—represented by the two-photon path diagrams [81] of Fig. 4.3(c)—by which the down-converted photons can pass through the apertures and get detected in coincidence at detectors D_s and D_i . In alternative 1(4), the signal photon passes through slit $A_{sa}(A_{sb})$ and the idler photon passes through slit $A_{ia}(A_{ib})$. In alternative 2(3), the signal photons passes through slit $A_{sa}(A_{sb})$ and the idler photon passes through slit $A_{ib}(A_{ia})$. We represent the states of the signal and idler photons in alternatives 1, 2, 3 and 4 by $|sa\rangle|ia\rangle$, $|sa\rangle|ib\rangle$, $|sb\rangle|ia\rangle$ and $|sb\rangle|ib\rangle$, respectively. Due to the strong position correlations of the down-converted photons in the image planes of the crystal, only two of the alternatives, alternatives 1 and 4, have appreciable probabilities whereas the other two alternatives, alternatives 2 and 3, have almost negligible probabilities. The state $|\psi_2\rangle$ of the two qubits thus prepared can ideally be given by $|\psi_{\text{qubit}}\rangle = 1/\sqrt{2} [|sa\rangle|ia\rangle + |sb\rangle|ib\rangle]$. In physical situations, however, quantum states are never completely pure; and therefore, they have to be represented by density matrices. The density matrix ρ_{qubit} of the two-qubit state thus prepared can be written in the angular-position basis

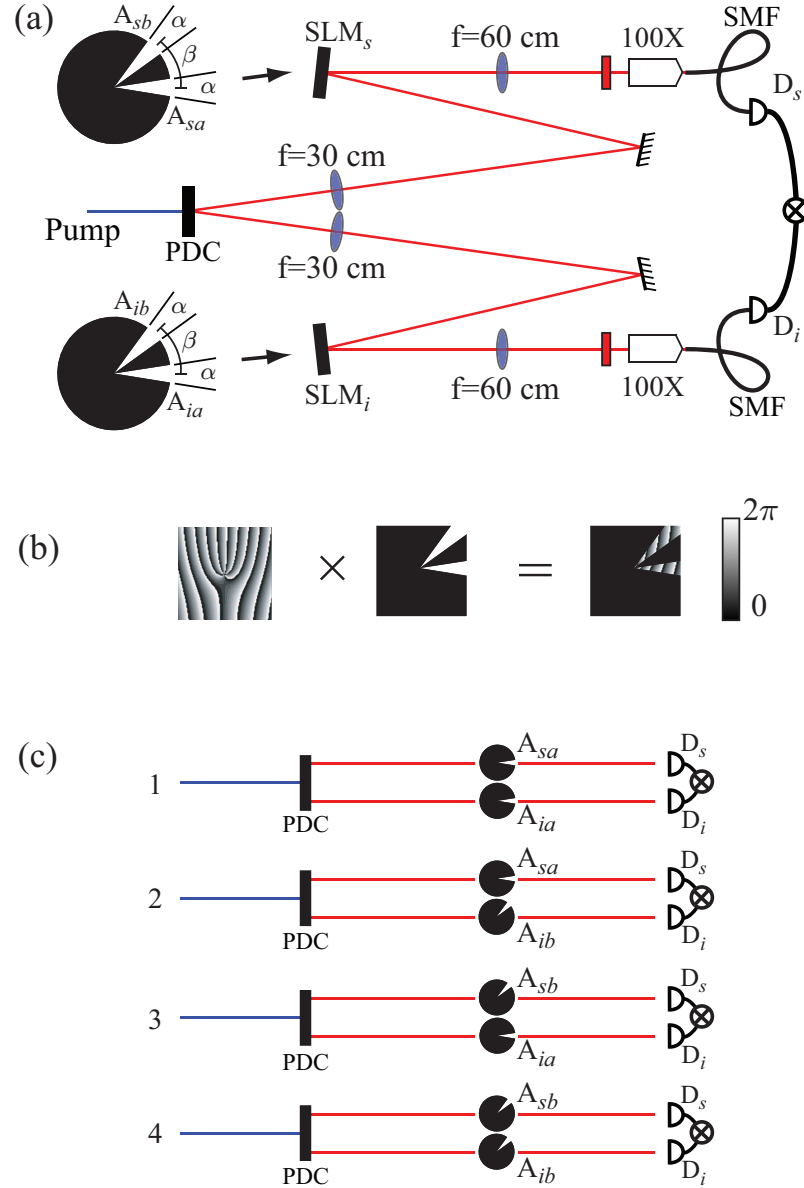


Figure 4.3: (a) Schematic of the experimental setup. The pump is a frequency-tripled, mode-locked, Nd-YAG laser (Excyte) with a pulse repetition frequency of 100 MHz and an average power of 150 mW at 355 nm. SLM denotes a spatial light modulator from Hamamatsu, SMF a single mode fiber, and F an interference filter centered at 710 nm. (b) A typical design of the SLM-phase pattern. (c) Two-photon path diagrams showing four alternative pathways by which signal and idler photons can pass through the angular-slits and be detected in coincidence at detectors D_s and D_i .

$\{|sa\rangle|ia\rangle, |sa\rangle|ib\rangle, |sb\rangle|ia\rangle, |sb\rangle|ib\rangle\}$ as:

$$\begin{aligned} \rho_{\text{qubit}} = & \rho_{11}|sa\rangle|ia\rangle\langle ia|\langle sa| + \rho_{14}|sa\rangle|ia\rangle\langle ib|\langle sb| \\ & + \rho_{41}|sb\rangle|ib\rangle\langle ia|\langle sa| + \rho_{44}|sb\rangle|ib\rangle\langle ib|\langle sb|, \end{aligned} \quad (4.8)$$

where ρ_{11} and ρ_{44} are the probabilities that the signal and idler photons are detected in alternatives 1 and 4, respectively, with $\rho_{11} + \rho_{44} = 1$. The off-diagonal term ρ_{14} is a measure of coherence between alternatives 1 and 4, with $\rho_{14} = \rho_{41}^*$; it is in general a complex number and can be written as $\rho_{14} = \sqrt{\rho_{11}\rho_{44}} \mu e^{i\theta}$, where μ is the degree of coherence and $e^{i\theta}$ the complex part of ρ_{14} . In writing Eq. (4.8), we have explicitly assumed that the probabilities ρ_{22} and ρ_{33} of finding the signal and idler photons in alternatives 2 and 3 are negligibly small.

We now write the density matrix ρ_{qubit} in the OAM basis. By taking the Fourier transforms of the amplitude transmission functions $A_{sa}(\phi_s)$ and $A_{ia}(\phi_i)$ [44, 45], corresponding to each OAM mode in the summation of Eq. (4.5), we write $|sa\rangle|ia\rangle$ in the OAM basis as

$$\begin{aligned} |sa\rangle|ia\rangle = & A \sum_l c_l \sum_{l'} \frac{1}{\sqrt{2\pi}} \int_{-\pi}^{\pi} d\phi_s A_{sa}(\phi_s) e^{-i(l'-l)\phi_s} |l'\rangle_s \\ & \times \sum_{l''} \frac{1}{\sqrt{2\pi}} \int_{-\pi}^{\pi} d\phi_i A_{ia}(\phi_i) e^{-i(l''+l)\phi_i} |l''\rangle_i, \end{aligned} \quad (4.9)$$

where A is the normalization constant to ensure that $\langle ia|\langle sa|sa\rangle|ia\rangle = 1$. Substituting for $A_{s1}(\phi_s)$ and $A_{i1}(\phi_i)$ from Eqs. (4.6), we evaluate the state to be

$$|s1\rangle|i1\rangle = \frac{A\alpha^2}{2\pi} \sum_l \sum_{l'} \sum_{l''} c_l \text{sinc} \left[(l' - l) \frac{\alpha}{2} \right] \text{sinc} \left[(l'' + l) \frac{\alpha}{2} \right] |l'\rangle_s |l''\rangle_i. \quad (4.10)$$

Because of the angular Fourier relationship, the OAM of the photon gets distributed among an envelope of OAM modes. In a similar manner, we evaluate $|s2\rangle|i2\rangle$ by

substituting from Eq. (4.7) to be

$$|s2\rangle|i2\rangle = \frac{A\alpha^2}{2\pi} \sum_l \sum_{l'} \sum_{l''} c_l \operatorname{sinc} \left[(l' - l) \frac{\alpha}{2} \right] \operatorname{sinc} \left[(l'' + l) \frac{\alpha}{2} \right] e^{-i(l'+l'')\beta} |l'\rangle_s |l''\rangle_i. \quad (4.11)$$

The coincidence count rate R_{si} of detectors D_s and D_i , which is the probability per (unit time)² that a photon is detected at detector D_s in mode l_s and another at detector D_i in mode l_i is given by $R_{si} = {}_i\langle l_i|_s\langle l_s|\rho|l_s\rangle_s|l_i\rangle_i$. Using Eqs. (4.6) through (4.11), we find that

$$R_{si} = \frac{A^2\alpha^4}{4\pi^2} \left| \sum_l c_l \operatorname{sinc} \left[(l_s - l) \frac{\alpha}{2} \right] \operatorname{sinc} \left[(l_i + l) \frac{\alpha}{2} \right] \right|^2 \times \{1 + 2\sqrt{\rho_{11}\rho_{44}} \mu \cos [(l_s + l_i)\beta + \theta]\}, \quad (4.12)$$

The interference between the two alternatives manifests itself in the periodic dependence on the angular separation β and on the sum of the OAMs $l_s + l_i$. From Eq. (4.12), ignoring the effects due to diffraction envelopes, the visibility V of the coincidence fringes can be seen to be

$$V = 2\sqrt{\rho_{11}\rho_{44}} \mu. \quad (4.13)$$

The entanglement of a general two-qubit state can be characterized in terms of Wootters's concurrence [76, 77], which ranges from 0 to 1, with 1 corresponding to the maximally-entangled two-qubit state and 0 to a non-entangled state. For a given two-qubit density matrix ρ , the concurrence $C(\rho)$ is then given by $C(\rho) = \max\{0, \sqrt{\lambda_1} - \sqrt{\lambda_2} - \sqrt{\lambda_3} - \sqrt{\lambda_4}\}$. Here the λ_i s are the eigenvalues, in descending order, of the matrix $\zeta = \rho(\sigma_y \otimes \sigma_y)\rho^*(\sigma_y \otimes \sigma_y)$, with $\sigma_y = \begin{pmatrix} 0 & -i \\ i & 0 \end{pmatrix}$ being the usual Pauli matrix, and where ρ^* is the complex conjugate of ρ .

To calculate the concurrence of our two-qubit state, we write the density matrix

ρ_{qubit} in the full 4×4 form, which is given as

$$\rho_{\text{qubit}} = \begin{pmatrix} \rho_{11} & 0 & 0 & \rho_{14} \\ 0 & 0 & 0 & 0 \\ 0 & 0 & 0 & 0 \\ \rho_{41} & 0 & 0 & \rho_{44} \end{pmatrix}, \quad (4.14)$$

Now, we evaluate the matrix $\zeta = \rho(\sigma_y \otimes \sigma_y)\rho^*(\sigma_y \otimes \sigma_y)$, which is given by:

$$\zeta = \begin{pmatrix} \rho_{11} & 0 & 0 & \rho_{14} \\ 0 & 0 & 0 & 0 \\ 0 & 0 & 0 & 0 \\ \rho_{41} & 0 & 0 & \rho_{44} \end{pmatrix} \cdot \begin{pmatrix} 0 & 0 & 0 & -1 \\ 0 & 0 & 1 & 0 \\ 0 & 1 & 0 & 0 \\ -1 & 0 & 0 & 0 \end{pmatrix} \cdot \begin{pmatrix} \rho_{11} & 0 & 0 & \rho_{41} \\ 0 & 0 & 0 & 0 \\ 0 & 0 & 0 & 0 \\ \rho_{14} & 0 & 0 & \rho_{44} \end{pmatrix} \cdot \begin{pmatrix} 0 & 0 & 0 & -1 \\ 0 & 0 & 1 & 0 \\ 0 & 1 & 0 & 0 \\ -1 & 0 & 0 & 0 \end{pmatrix} \quad (4.15)$$

Carrying out the above multiplication, we obtain

$$\zeta = \begin{pmatrix} \rho_{11}\rho_{44} + \rho_{14}\rho_{41} & 0 & 0 & 2\rho_{11}\rho_{14} \\ 0 & 0 & 0 & 0 \\ 0 & 0 & 0 & 0 \\ 2\rho_{44}\rho_{41} & 0 & 0 & \rho_{11}\rho_{44} + \rho_{14}\rho_{41} \end{pmatrix}. \quad (4.16)$$

The four eigenvalues of ζ , in the descending order, are:

$$\begin{aligned}\lambda_1 &= (\sqrt{\rho_{11}\rho_{44}} + \sqrt{\rho_{14}\rho_{41}})^2, \\ \lambda_2 &= (\sqrt{\rho_{11}\rho_{44}} - \sqrt{\rho_{14}\rho_{41}})^2, \\ \lambda_3 &= 0 \text{ and} \\ \lambda_4 &= 0.\end{aligned}\tag{4.17}$$

Since we have $\rho_{14} = \rho_{41}^*$, the four eigenvalues can be written as

$$\begin{aligned}\lambda_1 &= (\sqrt{\rho_{11}\rho_{44}} + |\rho_{14}|)^2, \\ \lambda_2 &= (\sqrt{\rho_{11}\rho_{44}} - |\rho_{14}|)^2, \\ \lambda_3 &= 0 \text{ and} \\ \lambda_4 &= 0.\end{aligned}\tag{4.18}$$

Thus, for the density matrix of Eq. (4.14), which has only two non-zero diagonal elements, the concurrence $C(\rho_{\text{qubit}}) = \max\{0, \sqrt{\lambda_1} - \sqrt{\lambda_2} - \sqrt{\lambda_3} - \sqrt{\lambda_4}\}$ is

$$C(\rho_{\text{qubit}}) = 2|\rho_{14}| = 2\sqrt{\rho_{11}\rho_{44}}\mu.\tag{4.19}$$

By comparing Eqs. (4.13) and (4.19), we see that the concurrence is equal to the visibility of the angular two-photon interference fringes

$$C(\rho_{\text{qubit}}) = V.\tag{4.20}$$

Thus, for a two-qubit state that can be represented by a density matrix having only two non-zero diagonal elements, the entanglement can be characterized using a single experimentally measurable quantity.

4.7 Experimental realization of an angular two-qubit state

In the setup of Fig. 4.3, the pump is a frequency-tripled, mode-locked, Nd-YAG laser (Excyte) with a pulse repetition frequency of 100 MHz and an average power of 150 mW at 355 nm. SLM denotes a spatial light modulator from Hamamatsu, SMF a single mode fiber, and F an interference filter centered at 710 nm. The beam waist width of the Gaussian pump beam at the PDC crystal plane was approximately 400 μm . The crystal plane was imaged, with a magnification of about 5, onto the SLM planes, which were then imaged onto the input facets of the SMFs with a demagnification of about 380. The SLMs were used for two purposes as illustrated in Fig. 4.3(b). One, they were used for selecting out OAM modes [147]; and two, they were used for simulating amplitude apertures [165] described by Eqs. (4.6) and (4.7).

First of all, without any apertures, the mode probabilities $|c_l|^2$ were measured. Figure 4.4 shows the measured coincidence counts plotted against l , with signal and idler photons being detected in modes of order l and $-l$, respectively. The mode probabilities $|c_l|^2$ were calculated by normalizing the counts of Fig. 4.4.

Secondly, we verify the preparation of the two-qubit state as represented by Eq. (4.8). Coincidence counts were measured with only one of the signal and one of the idler slits, with $\alpha = \pi/10$ and $\beta = \pi/4$, being displayed on the SLMs and with both signal and idler photons being detected in modes of order 0. Figure 4.5 shows the measured coincidence detection probabilities of the signal and idler photons in the four different alternatives. We find that the probabilities ρ_{22} and ρ_{33} are negligibly small and that only the two probabilities, ρ_{11} and ρ_{44} , are appreciably greater than zero. Therefore, as shown by Eq. (4.20), the entanglement of the prepared two-qubit state can be characterized by measuring the visibility of two-photon interference fringes in the OAM basis.

Next, measurements were made in the OAM basis. Both signal and idler slits,

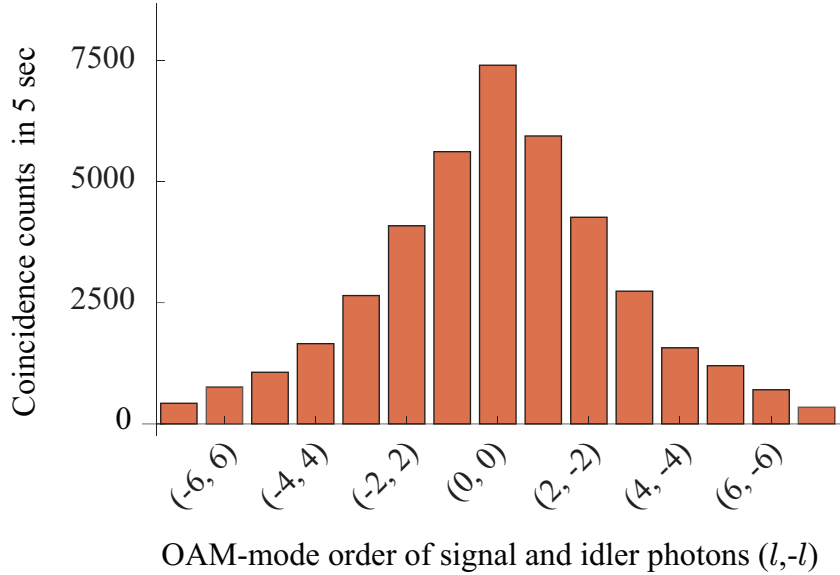


Figure 4.4: Measurements of the OAM-mode probabilities, with no patterns being displayed on the SLMs. Measured coincidence counts are given as a function of l , the OAM-mode order of the detected signal photon, with $-l$ being the OAM-mode order of the idler photon. The width of this distribution is known as the spiral bandwidth, which is limited by the finite numerical aperture of the detection system.

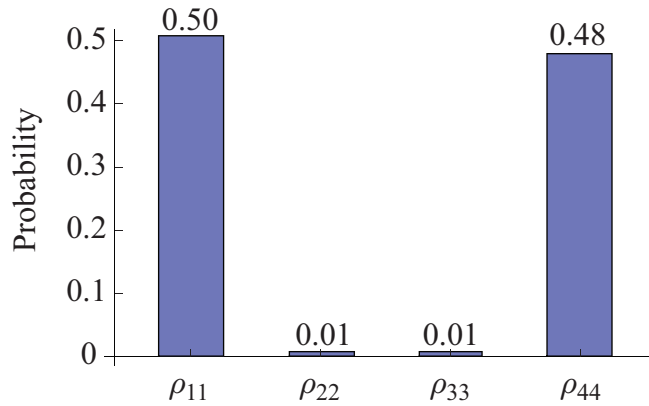


Figure 4.5: Measurements in the angular position basis. Measured coincidence detection probabilities ρ_{11} , ρ_{22} , ρ_{33} and ρ_{44} of the signal and idler photons in alternatives 1, 2, 3 and 4, respectively, are shown. The probabilities ρ_{22} and ρ_{33} are negligibly small, showing that the two-qubit state prepared in our experiment resembles the state represented by Eq. (4.8) to an excellent approximation.

with $\alpha = \pi/10$ and $\beta = \pi/4$, were displayed on the SLMs. SLM_{*i*} was adjusted to successively select out two different idler OAM modes: $l_i = 2$ and $l_i = -2$. For each

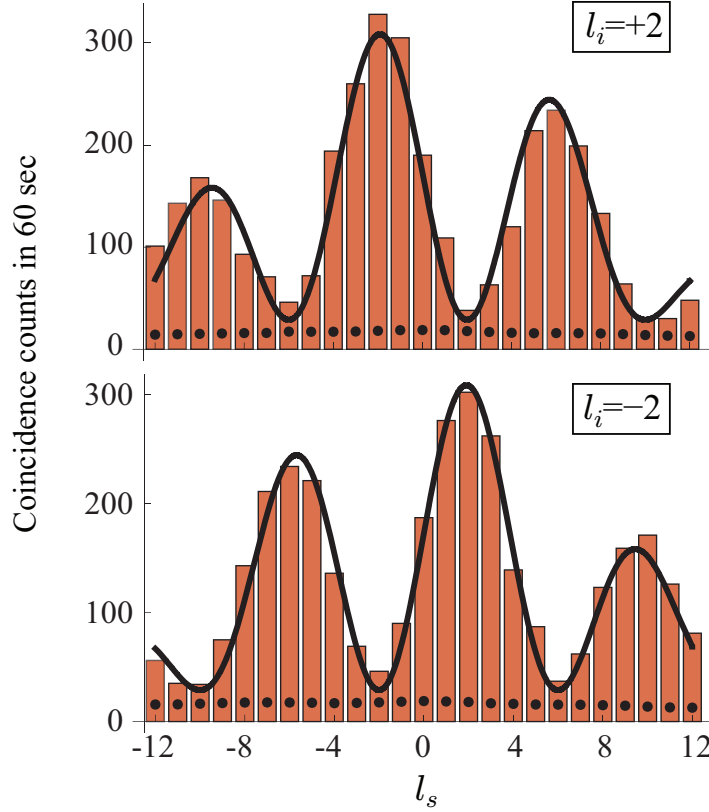


Figure 4.6: Measurements in the OAM basis. Measured coincidence counts are given as functions of l_s for two different values of l_i , with $\alpha = \pi/10$ and $\beta = \pi/4$. The dotted lines are measured random coincidences for the 25-ns coincidence detection-window. The solid lines are theoretical fits obtained from Eq. (4.12). The high visibility of angular two-photon interference fringes shows that the prepared two-qubit state is highly entangled.

selected idler mode l_i , coincidence counts were measured as a function of the signal OAM mode l_s . Figure 4.6 shows the coincidence counts plotted against l_s for two different values of l_i . The dotted lines are measured random coincidences for the 25-ns coincidence detection-window. The solid lines are theoretical fits based on Eq. (4.12), using the values of $|c_l|^2$ calculated from Fig. 4.4. The visibility of the two-photon fringes is about 83%, without subtracting random coincidences, and about 90%, with random coincidences subtracted. Thus, using Eq. (4.20), we find that the concurrence of the prepared two-qubit state, which is equal to the visibility of angular two-photon fringes, is 0.83 (0.90, with random coincidences subtracted). The reason for less

than unit concurrence is mostly imperfect experimental alignment. We note that the angular-position correlations as observed in Fig. 4.5 and the angular two-photon interference effects as observed in Fig. 4.6 can be produced simultaneously only by angular-position–OAM entangled sources. A non-entangled source can produce one but not both set of correlations. The results presented in this chapter have been reported in Ref. [162].

4.8 Summary

In this chapter, we have described a two-alternative angular two-photon interference using the entangled photons produced by parametric down-conversion. We have reported experimental demonstrations of an entangled two-qubit state based on the angular-position correlations of the down-converted two-photon field. The state was prepared by using apertures in the form of double angular-slits, and it was characterized through separate measurements in angular position and OAM bases. We have quantified the entanglement of the state by evaluating the concurrence. A demonstration of an angular-position-based entangled two-qubit state not only provides an additional resource for quantum information science but also has significance in the discussions related to the angular uncertainty relation and angular EPR paradox. We believe that our method of preparing entangled two-qubit states can be easily generalized to preparing entangled two-qudit states $|\psi_d\rangle$ of the form: $|\psi_d\rangle = 1/\sqrt{d} [|s1\rangle|i1\rangle + |s2\rangle|i2\rangle \cdots + |sd\rangle|id\rangle]$, using apertures with d angular-slits.

The description of angular two-photon interference presented in this chapter only considers a particular interference scenario; the present description does not account for situations in which the angular slits are not located in the image planes of the crystals. The present description also does not explicitly treat the effects due to the limited spatial coherence of the pump field. These and similar other questions will form the topic of further research on the subject.

Chapter 5

Conclusions and Discussion

Parametric down-conversion is the most widely used process for generating entangled two-photon fields. It is a second-order nonlinear optical process in which a pump photon interacts with a nonlinear crystal and breaks up into two separate photons known as the signal photon and the idler photon. The constraints of energy and momentum conservation in parametric down-conversion render the two photons entangled in several different variables including time and energy, position and momentum, and angular position and orbital angular momentum. In this thesis, we have developed a theoretical formalism to study the coherence properties of the entangled two-photon field produced by down-conversion. We have also carried out several experiments to study, explore and quantify entanglement of the down-converted two-photon field, and have used our theoretical formalism to analyze these experiments successfully.

In the first part of this thesis, the temporal coherence properties of the down-converted two-photon field were studied. The description of temporal two-photon interference with the down-converted signal and idler photons involves, in general, six different length parameters, which are the path lengths traveled by the pump, signal and idler photons in two interfering alternatives. In terms of these six length parameters, two separate length parameters—called the two-photon path length difference and the two-photon path-asymmetry length difference—were constructed. A

theoretical formalism was developed in terms of the two constructed length parameters to describe temporal two-photon interference, in situations in which the frequency bandwidth of the pump field is much narrower than that of the down-converted signal and idler fields. It was shown that temporal two-photon interference effects, including one-photon interference effects observed in certain two-photon interference experiments, can be completely characterized in terms of the variations of these two parameters. A two-photon interference experiment was performed in a double-pass setup, in which the variations of the two length parameters could be independently controlled and studied. In the setup, which did not involve mixing of signal and idler photons at a beam splitter, experimental observations of Hong-Ou-Mandel- (HOM-)like effects were reported both in coincidence and in one-photon count rates. These results were then used to argue that HOM and HOM-like effects are best described as observations of how two-photon coherence changes with a variation in the two-photon path-asymmetry-length difference.

As part of the temporal coherence studies, an alternative way to explore time-energy entanglement was investigated; the common way to exploit time-energy entanglement of the down-converted photons is by means of the dynamic phases of the signal and idler photons. Through an experimental observation of a purely-geometric-phase-based violation of Bell inequality for time and energy, it was shown that the time-energy entanglement of the down-converted photons can also be explored using the geometric phases of the signal and idler photons. This result provides an additional means by which time-energy entanglement, which is a resource to many quantum information protocols, can be manipulated.

In the second part of the thesis, the spatial coherence properties of the down-converted two-photon field were investigated, in situations in which the pump field is, spatially, a partially coherent beam of Gaussian Schell-model type. A description of spatial two-photon interference was presented in terms of two displacement parameters, which were constructed using the transverse position vectors of the signal

and idler photons in two interfering alternatives. In terms of the two displacement parameters, it was shown that in parametric down-conversion the spatial coherence properties of the pump field get entirely transferred to the spatial coherence properties of the down-converted two-photon field. Next, the connection between the degree of spatial two-photon-coherence and the entanglement of two-qubit states that are based on the spatial correlations of down-converted photons was investigated. It was found that the entanglement of a spatial two-qubit state, as quantified by concurrence, is proportional to the magnitude of the two-photon cross-spectral density at the two pairs of transverse positions that define the two-qubit state. In the special case for which the two-photon spectral densities at the two pairs of transverse positions are equal, concurrence of the state becomes equal to the degree of spatial two-photon-coherence. Since the degree of spatial two-photon-coherence depends on the degree of spatial coherence of the pump field, it then follows that the maximum achievable entanglement of a spatial two-qubit state is bounded by the degree of spatial coherence of the pump field.

In the last part of the thesis, two-photon-coherence effects in the angular domain were studied. An entangled two-qubit state that is based on the angular-position correlations of the down-converted photons was experimentally demonstrated. The qubit-state was prepared by using apertures in the form of double angular-slits, and it was characterized by making separate measurements in the angular position and orbital angular momentum bases. The entanglement of the prepared angular two-qubit state was quantified by evaluating its concurrence. This result is important as it shows that the angular-position basis can be usefully exploited for applications in quantum information science. The method used in this experiment can be easily generalized for preparing entangled two-qudit states, using apertures with d angular-slits.

In this thesis, the coherence properties of the entangled two-photon field were studied using four-point correlation functions. An equivalent description of two-photon

coherence, something that could be pursued as a follow-up work, can also be given in terms of the two-photon-analogs of the phase-space distribution functions, such as the Wigner distribution function [166] and the Glauber-Sudarshan P-function [32, 167]. As two-photon coherence and bipartite entanglement are related concepts, studying the phase-space descriptions of two-photon fields may even lead to a more intuitive understanding of bipartite entanglement.

Bibliography

- [1] L. Mandel, “Quantum effects in one-photon and two-photon interference,” *Rev. Mod. Phys.* **71**, S274 (1999).
- [2] M. Born and E. Wolf, *Principles of Optics*, 7th expanded ed. (Cambridge University Press, Cambridge, 1999).
- [3] C. K. Hong, Z. Y. Ou, and L. Mandel, “Measurement of subpicosecond time intervals between two photons by interference,” *Phys. Rev. Lett.* **59**, 2044 (1987).
- [4] X. Y. Zou, L. J. Wang, and L. Mandel, “Induced coherence and indistinguishability in optical interference,” *Phys. Rev. Lett.* **67**, 318 (1991).
- [5] T. J. Herzog, J. G. Rarity, H. Weinfurter, and A. Zeilinger, “Frustrated two-photon creation via interference,” *Phys. Rev. Lett.* **72**, 629 (1994).
- [6] T. B. Pittman, D. V. Strekalov, A. Migdall, M. H. Rubin, A. V. Sergienko, and Y. H. Shih, “Can two-photon interference be considered the interference of two photons?,” *Phys. Rev. Lett.* **77**, 1917 (1996).
- [7] J. D. Franson, “Bell inequality for position and time,” *Phys. Rev. Lett.* **62**, 2205 (1989).
- [8] P. G. Kwiat, A. M. Steinberg, and R. Y. Chiao, “High-visibility interference in a Bell-inequality experiment for energy and time,” *Phys. Rev. A* **47**, R2472 (1993).

-
- [9] J. Brendel, E. Mohler, and W. Martienssen, “Time-resolved dual-beam two-photon interferences with high visibility,” *Phys. Rev. Lett.* **66**, 1142 (1991).
- [10] D. V. Strekalov, T. B. Pittman, and Y. H. Shih, “What we can learn about single photons in a two-photon interference experiment,” *Phys. Rev. A* **57**, 567 (1998).
- [11] M. Mitchell, J. Lundeen, and A. Steinberg, “Super-resolving phase measurements with a multiphoton entangled state,” *Nature* **429**, 161 (2004).
- [12] P. Walther, J. Pan, M. Aspelmeyer, R. Ursin, S. Gasparoni, and A. Zeilinger, “De Broglie wavelength of a non-local four-photon state,” *Nature* **429**, 158 (2004).
- [13] R. Hanbury Brown and R. Q. Twiss, “Correlation between photons in two coherent beams of light rays,” *Nature* **177**, 27 (1956).
- [14] R. Hanbury Brown and R. Q. Twiss, “The question of correlation between photons in coherent light rays,” *Nature* **178**, 1447 (1956).
- [15] C. A. Kocher and E. D. Commins, “Polarization correlation of photons emitted in an atomic cascade,” *Phys. Rev. Lett.* **18**, 575 (1967).
- [16] S. J. Freedman and J. F. Clauser, “Experimental test of local hidden-variable theories,” *Phys. Rev. Lett.* **28**, 938 (1972).
- [17] A. Einstein, B. Podolsky, and N. Rosen, “Can quantum-mechanical description of physical reality be considered complete?,” *Phys. Rev.* **47**, 777 (1935).
- [18] J. S. Bell, “On the Einstein Podolsky Rosen paradox,” *Physics* **1**, 195 (1964).
- [19] A. Aspect, P. Grangier, and G. Roger, “Experimental tests of realistic local theories via Bell’s theorem,” *Phys. Rev. Lett.* **47**, 460 (1981).

-
- [20] A. Aspect, P. Grangier, and G. Roger, “Experimental realization of Einstein-Podolsky-Rosen-Bohm gedankenexperiment: A new violation of Bell’s inequalities,” *Phys. Rev. Lett.* **49**, 91 (1982).
- [21] J. G. Rarity and P. R. Tapster, “Experimental violation of Bell’s inequality based on phase and momentum,” *Phys. Rev. Lett.* **64**, 2495 (1990).
- [22] A. Vaziri, G. Weihs, and A. Zeilinger, “Experimental two-photon, three-dimensional entanglement for quantum communication,” *Phys. Rev. Lett.* **89**, 240401 (2002).
- [23] D. Bohm, “A suggested interpretation of the quantum theory in terms of “hidden” variables. I,” *Phys. Rev.* **85**, 166 (1952).
- [24] D. Bohm, “A suggested interpretation of the quantum theory in terms of “hidden” variables. II,” *Phys. Rev.* **85**, 180 (1952).
- [25] A. K. Ekert, “Quantum cryptography based on Bell’s theorem,” *Phys. Rev. Lett.* **67**, 661 (1991).
- [26] C. H. Bennett and S. J. Wiesner, “Communication via one- and two-particle operators on Einstein-Podolsky-Rosen states,” *Phys. Rev. Lett.* **69**, 2881 (1992).
- [27] C. H. Bennett, G. Brassard, C. Crépeau, R. Jozsa, A. Peres, and W. K. Wootters, “Teleporting an unknown quantum state via dual classical and Einstein-Podolsky-Rosen channels,” *Phys. Rev. Lett.* **70**, 1895 (1993).
- [28] B. Yurke and D. Stoler, “Einstein-Podolsky-Rosen effects from independent particle sources,” *Phys. Rev. Lett.* **68**, 1251 (1992).
- [29] A. N. Boto, P. Kok, D. S. Abrams, S. L. Braunstein, C. P. Williams, and J. P. Dowling, “Quantum interferometric optical lithography: Exploiting entanglement to beat the diffraction limit,” *Phys. Rev. Lett.* **85**, 2733 (2000).

- [30] L. Mandel and E. Wolf, *Optical Coherence and Quantum Optics* (Cambridge university press, New York, 1995).
- [31] R. J. Glauber, "The quantum theory of optical coherence," *Phys. Rev.* **130**, 2529 (1963).
- [32] R. J. Glauber, "Coherent and incoherent states of the radiation field," *Phys. Rev.* **131**, 2766 (1963).
- [33] R. W. Boyd, *Nonlinear Optics*, 2nd ed. (Academic Press, New York, 2003).
- [34] H. Takesue and K. Inoue, "Generation of polarization-entangled photon pairs and violation of Bell's inequality using spontaneous four-wave mixing in a fiber loop," *Phys. Rev. A* **70**, 031802 (2004).
- [35] M. Y. Shverdin, D. R. Walker, D. D. Yavuz, G. Y. Yin, and S. E. Harris, "Generation of a single-cycle optical pulse," *Phys. Rev. Lett.* **94**, 033904 (2005).
- [36] L. Mandel, "Coherence and indistinguishability," *Opt. Lett.* **16**, 1882 (1991).
- [37] A. T. Forrester, R. A. Gudmundsen, and P. O. Johnson, "Photoelectric mixing of incoherent light," *Phys. Rev.* **99**, 1691 (1955).
- [38] G. Magyar and L. Mandel, "Interference fringes produced by superposition of two independent maser light beams," *Nature (London)* **198**, 255 (1963).
- [39] P. Pääkkönen, J. Turunen, P. Vahimaa, A. T. Friberg, and F. Wyrowski, "Partially coherent Gaussian pulses," *Opt. Comm.* **204**, 53 (2002).
- [40] B. Cairns and E. Wolf, "The instantaneous cross-spectral density of non-stationary wavefields," *Opt. Comm.* **62**, 215 (1987).
- [41] S. A. Ponomarenko, G. P. Agrawal, and E. Wolf, "Energy spectrum of a non-stationary ensemble of pulses," *Opt. Lett.* **29**, 394 (2004).

-
- [42] W. H. Carter and E. Wolf, “Correlation theory of wavefields generated by fluctuating, three-dimensional, primary, scalar sources. I. general theory,” *Opt. Acta* **28**, 227 (1981).
- [43] W. H. Carter and E. Wolf, “Correlation theory of wavefields generated by fluctuating, three-dimensional, primary, scalar sources. II. radiation from isotropic model sources,” *Opt. Acta* **28**, 245 (1981).
- [44] S. M. Barnett and D. T. Pegg, “Quantum theory of rotation angles,” *Phys. Rev. A* **41**, 3427 (1990).
- [45] S. Franke-Arnold, S. Barnett, E. Yao, J. Leach, J. Courtial, and M. Padgett, “Uncertainty principle for angular position and angular momentum,” *New Journal of Physics* **6**, 103 (2004).
- [46] G. W. Forbes, M. A. Alonso, and A. E. Siegman, “Uncertainty relations and minimum uncertainty states for the discrete Fourier transform and the Fourier series,” *J. Phys. A: Math. Gen.* **36**, 7027 (2003).
- [47] M. W. Beijersbergen, R. P. C. Coerwinkel, M. Kristensen, and J. P. Woerdman, “Helical-wavefront laser beams produced with a spiral phaseplate,” *Opt. Comm.* **112**, 321 (1994).
- [48] L. Allen, M. Beijersbergen, R. Spreeuw, and J. Woerdman, “Orbital angular momentum of light and the transformation of Laguerre-Gaussian laser modes,” *Phys. Rev. A* **45**, 8185 (1992).
- [49] B. Jack, M. Padgett, and S. Franke-Arnold, “Angular diffraction,” *New Journal of Physics* **10**, 103013 (2008).
- [50] A. K. Jha *et al.*, “Fourier relationship between the angle and angular momentum of entangled photons,” *Phys. Rev. A* **78**, 043810 (2008).

-
- [51] N. Bloembergen, “Conservation laws in nonlinear optics,” *J. Opt. Soc. Am.* **70**, 1429 (1980).
- [52] D. A. Kleinman, “Theory of optical parametric noise,” *Phys. Rev.* **174**, 1027 (1968).
- [53] C. K. Hong and L. Mandel, “Theory of parametric frequency down conversion of light,” *Phys. Rev. A* **31**, 2409 (1985).
- [54] D. N. Klyshko, “Scattering of light in a medium with nonlinear polarizability,” *Soviet Physics JETP* **28**, 522 (1969).
- [55] D. C. Burnham and D. L. Weinberg, “Observation of simultaneity in parametric production of optical photon pairs,” *Phys. Rev. Lett.* **25**, 84 (1970).
- [56] B. R. Mollow, “Quantum statistics of coupled oscillator systems,” *Phys. Rev.* **162**, 1256 (1967).
- [57] B. R. Mollow and R. J. Glauber, “Quantum theory of parametric amplification. I,” *Phys. Rev.* **160**, 1076 (1967).
- [58] R. Loudon, *The Quantum Theory of Light*, 3rd ed. (Oxford University Press, New York, USA, 2000).
- [59] E. Schrödinger, “Die gegenwärtige situation in der quantenmechanik,” *Naturewiss* **23**, 807 (1935).
- [60] R. Horodecki, P. Horodecki, M. Horodecki, and K. Horodecki, “Quantum entanglement,” *Reviews of Modern Physics* **81**, 865 (2009).
- [61] P. G. Kwiat and L. Hardy, “The mystery of the quantum cakes,” *American Journal of Physics* **68**, 33 (2000).
- [62] L. Hardy, “Spooky action at a distance in quantum mechanics,” *Contemporary physics* **39**, 419 (1998).

- [63] J. F. Clauser, M. A. Horne, A. Shimony, and R. A. Holt, “Proposed experiment to test local hidden-variable theories,” *Phys. Rev. Lett.* **23**, 880 (1969).
- [64] Z. Y. Ou and L. Mandel, “Violation of Bell’s inequality and classical probability in a two-photon correlation experiment,” *Phys. Rev. Lett.* **61**, 50 (1988).
- [65] Y. H. Shih and C. O. Alley, “New type of Einstein-Podolsky-Rosen-Bohm experiment using pairs of light quanta produced by optical parametric down conversion,” *Phys. Rev. Lett.* **61**, 2921 (1988).
- [66] T. Yarnall, A. Abouraddy, B. Saleh, and M. Teich, “Experimental violation of Bell’s inequality in spatial-parity space,” *Phys. Rev. Lett.* **99**, 170408 (2007).
- [67] S. Ramelow, L. Ratschbacher, A. Fedrizzi, N. Langford, and A. Zeilinger, “Discrete, tunable color entanglement,” Arxiv preprint arXiv:0904.4916 (2009).
- [68] J. Leach *et al.*, “Violation of a Bell inequality in two-dimensional orbital angular momentum state-spaces,” *Opt. Express* **17**, 8287 (2009).
- [69] D. V. Strekalov, T. B. Pittman, A. V. Sergienko, Y. H. Shih, and P. G. Kwiat, “Postselection-free energy-time entanglement,” *Phys. Rev. A* **54**, R1 (1996).
- [70] C. Cinelli, M. Barbieri, R. Perris, P. Mataloni, and F. D. Martini, “All-versus-nothing nonlocality test of quantum mechanics by two-photon hyperentanglement,” *Phys. Rev. Lett.* **95**, 240405 (2005).
- [71] T. Yang *et al.*, “All-versus-nothing violation of local realism by two-photon, four-dimensional entanglement,” *Phys. Rev. Lett.* **95**, 240406 (2005).
- [72] J. T. Barreiro, N. K. Langford, N. A. Peters, and P. G. Kwiat, “Generation of hyperentangled photon pairs,” *Phys. Rev. Lett.* **95**, 260501 (2005).
- [73] D. Collins, N. Gisin, N. Linden, S. Massar, and S. Popescu, “Bell inequalities for arbitrarily high-dimensional systems,” *Phys. Rev. Lett.* **88**, 040404 (2002).

- [74] V. Vedral and M. B. Plenio, “Entanglement measures and purification procedures,” *Phys. Rev. A* **57**, 1619 (1998).
- [75] B. M. Terhal and P. Horodecki, “Schmidt number for density matrices,” *Phys. Rev. A* **61**, 040301 (2000).
- [76] S. Hill and W. K. Wootters, “Entanglement of a pair of quantum bits,” *Phys. Rev. Lett.* **78**, 5022 (1997).
- [77] W. K. Wootters, “Entanglement of formation of an arbitrary state of two qubits,” *Phys. Rev. Lett.* **80**, 2245 (1998).
- [78] K. Życzkowski, P. Horodecki, A. Sanpera, and M. Lewenstein, “Volume of the set of separable states,” *Phys. Rev. A* **58**, 883 (1998).
- [79] V. Coffman, J. Kundu, and W. K. Wootters, “Distributed entanglement,” *Phys. Rev. A* **61**, 052306 (2000).
- [80] P. A. M. Dirac, *The Principles of Quantum Mechanics*, 3rd ed. (Clarendon Press, Oxford, 1947).
- [81] A. K. Jha, M. N. O’Sullivan, K. W. C. Chan, and R. W. Boyd, “Temporal coherence and indistinguishability in two-photon interference effects,” *Phys. Rev. A* **77**, 021801(R) (2008).
- [82] Y.-H. Kim, M. V. Chekhova, S. P. Kulik, Y. Shih, and M. H. Rubin, “First-order interference of nonclassical light emitted spontaneously at different times,” *Phys. Rev. A* **61**, 051803 (2000).
- [83] J. Brendel, W. Dultz, and W. Martienssen, “Geometric phases in two-photon interference experiments,” *Phys. Rev. A* **52**, 2551 (1995).
- [84] Z. Y. Ou, L. J. Wang, and L. Mandel, “Vacuum effects on interference in two-photon down conversion,” *Phys. Rev. A* **40**, 1428 (1989).

-
- [85] L. J. Wang, X. Y. Zou, and L. Mandel, “Induced coherence without induced emission,” *Phys. Rev. A* **44**, 4614 (1991).
- [86] C. H. Monken, P. H. S. Ribeiro, and S. Pádua, “Transfer of angular spectrum and image formation in spontaneous parametric down-conversion,” *Phys. Rev. A* **57**, 3123 (1998).
- [87] A. K. Jha, M. Malik, and R. W. Boyd, “Exploring energy-time entanglement using geometric phase,” *Phys. Rev. Lett.* **101**, 180405 (2008).
- [88] W. P. Grice and I. A. Walmsley, “Spectral information and distinguishability in type-II down-conversion with a broadband pump,” *Phys. Rev. A* **56**, 1627 (1997).
- [89] R. Bhandari and J. Samuel, “Observation of topological phase by use of a laser interferometer,” *Phys. Rev. Lett.* **60**, 1211 (1988).
- [90] M. H. Rubin, D. N. Klyshko, Y. H. Shih, and A. V. Sergienko, “Theory of two-photon entanglement in type-II optical parametric down-conversion,” *Phys. Rev. A* **50**, 5122 (1994).
- [91] T. E. Keller and M. H. Rubin, “Theory of two-photon entanglement for spontaneous parametric down-conversion driven by a narrow pump pulse,” *Phys. Rev. A* **56**, 1534 (1997).
- [92] A. K. Jha, M. N. O’Sullivan, K. W. C. Chan, and R. W. Boyd, “Temporal coherence of the entangled two-photon field produced by parametric down-conversion,” to be submitted .
- [93] P. Grangier, “Single photons stick together,” *Nature* **419**, 577 (2002).
- [94] J. C. Howell, R. S. Bennink, S. J. Bentley, and R. W. Boyd, “Realization of the Einstein-Podolsky-Rosen paradox using momentum- and position-entangled

- photons from spontaneous parametric down conversion,” *Phys. Rev. Lett.* **92**, 210403 (2004).
- [95] J. Brendel, N. Gisin, W. Tittel, and H. Zbinden, “Pulsed energy-time entangled twin-photon source for quantum communication,” *Phys. Rev. Lett.* **82**, 2594 (1999).
- [96] R. T. Thew, A. Acín, H. Zbinden, and N. Gisin, “Bell-type test of energy-time entangled qutrits,” *Phys. Rev. Lett.* **93**, 010503 (2004).
- [97] S. Aerts, P. Kwiat, J.-A. Larsson, and M. Żukowski, “Two-photon Franson-type experiments and local realism,” *Phys. Rev. Lett.* **83**, 2872 (1999).
- [98] A. Cabello, A. Rossi, G. Vallone, F. D. Martini, and P. Mataloni, “Proposed Bell experiment with genuine energy-time entanglement,” *Phys. Rev. Lett.* **102**, 040401 (2009).
- [99] P. G. Kwiat, K. Mattle, H. Weinfurter, A. Zeilinger, A. V. Sergienko, and Y. Shih, “New high-intensity source of polarization-entangled photon pairs,” *Phys. Rev. Lett.* **75**, 4337 (1995).
- [100] M. Berry, “Quantal phase factors accompanying adiabatic changes,” *Proc. Roy. Soc. (London) A* **392**, 45 (1984).
- [101] S. Pancharatnam, “Generalized theory of interference and its applications. part 2: Partially coherent pencils,” *Proceedings of the Indian Academy of Sciences A* **44**, 247 (1956).
- [102] S. Ramaseshan and R. Nityananda, “The interference of polarized light as an early example of Berry’s phase,” *Current Science* **55**, 1225 (1986).
- [103] M. V. Berry, “The adiabatic phase and Pancharatnam’s phase for polarized light,” *J. Mod. Opt.* **34**, 1401 (1987).

-
- [104] T. H. Chyba, L. J. Wang, L. Mandel, and R. Simon, “Measurement of the Pancharatnam phase for a light beam,” *Opt. Lett.* **13**, 562 (1988).
- [105] A. Tomita and R. Y. Chiao, “Observation of Berry’s topological phase by use of an optical fiber,” *Phys. Rev. Lett.* **57**, 937 (1986).
- [106] P. G. Kwiat and R. Y. Chiao, “Observation of a nonclassical Berry’s phase for the photon,” *Phys. Rev. Lett.* **66**, 588 (1991).
- [107] D. V. Strekalov and Y. H. Shih, “Two-photon geometrical phase,” *Phys. Rev. A* **56**, 3129 (1997).
- [108] T. P. Grayson, J. R. Torgerson, and G. A. Barbosa, “Observation of a nonlocal Pancharatnam phase shift in the process of induced coherence without induced emission,” *Phys. Rev. A* **49**, 626 (1994).
- [109] E. J. Galvez, M. Malik, and B. C. Melius, “Phase shifting of an interferometer using nonlocal quantum-state correlations,” *Phys. Rev. A* **75**, 020302 (2007).
- [110] B. Hessmo and E. Sjöqvist, “Quantal phase for nonmaximally entangled photons,” *Phys. Rev. A* **62**, 062301 (2000).
- [111] B. Terhal, “Bell inequalities and the separability criterion,” *Phys. Lett. A* **271**, 319 (2000).
- [112] C. Cinelli, G. Di Nepi, F. De Martini, M. Barbieri, and P. Mataloni, “Parametric source of two-photon states with a tunable degree of entanglement and mixing: Experimental preparation of Werner states and maximally entangled mixed states,” *Phys. Rev. A* **70**, 022321 (2004).
- [113] G. Vallone, E. Pomarico, P. Mataloni, F. D. Martini, and V. Berardi, “Realization and characterization of a two-photon four-qubit linear cluster state,” *Phys. Rev. Lett.* **98**, 180502 (2007).

-
- [114] P. Hariharan, K. Larkin, and M. Roy, “The geometric phase: interferometric observations with white light,” *J. Mod. Opt.* **41**, 663 (1994).
- [115] R. Bhandari, “Polarization of light and topological phases,” *Phys. Rep.* **281**, 1 (1997).
- [116] S. Carrasco *et al.*, “Broadband light generation by noncollinear parametric downconversion,” *Opt. Lett.* **31**, 253 (2006).
- [117] M. B. Nasr *et al.*, “Ultrabroadband biphotons generated via chirped quasi-phase-matched optical parametric down-conversion,” *Phys. Rev. Lett.* **100**, 183601 (2008).
- [118] M. H. Rubin, “Transverse correlation in optical spontaneous parametric down-conversion,” *Phys. Rev. A* **54**, 5349 (1996).
- [119] A. Joobeur, B. E. A. Saleh, T. S. Larchuk, and M. C. Teich, “Coherence properties of entangled light beams generated by parametric down-conversion: Theory and experiment,” *Phys. Rev. A* **53**, 4360 (1996).
- [120] P. H. Souto Ribeiro, “Partial coherence with twin photons,” *Phys. Rev. A* **56**, 4111 (1997).
- [121] E. J. S. Fonseca, C. H. Monken, S. Pádua, and G. A. Barbosa, “Transverse coherence length of down-converted light in the two-photon state,” *Phys. Rev. A* **59**, 1608 (1999).
- [122] B. E. A. Saleh, M. C. Teich, and A. V. Sergienko, “Wolf equations for two-photon light,” *Phys. Rev. Lett.* **94**, 223601 (2005).
- [123] L. Mandel, “Photon interference and correlation effects produced by independent quantum sources,” *Phys. Rev. A* **28**, 929 (1983).

-
- [124] R. Ghosh, C. K. Hong, Z. Y. Ou, and L. Mandel, “Interference of two photons in parametric down conversion,” *Phys. Rev. A* **34**, 3962 (1986).
- [125] R. Ghosh and L. Mandel, “Observation of nonclassical effects in the interference of two photons,” *Phys. Rev. Lett.* **59**, 1903 (1987).
- [126] D. V. Strekalov, A. V. Sergienko, D. N. Klyshko, and Y. H. Shih, “Observation of two-photon “ghost” interference and diffraction,” *Phys. Rev. Lett.* **74**, 3600 (1995).
- [127] M. D’Angelo, M. V. Chekhova, and Y. Shih, “Two-photon diffraction and quantum lithography,” *Phys. Rev. Lett.* **87**, 013602 (2001).
- [128] C. K. Hong and T. G. Noh, “Two-photon double-slit interference experiment,” *J. Opt. Soc. Am. B* **15**, 1192 (1998).
- [129] G. Brida, E. Cagliero, G. Falzetta, M. Genovese, M. Gramegna, and E. Predazzi, “Biphoton double-slit experiment,” *Phys. Rev. A* **68**, 033803 (2003).
- [130] E. J. S. Fonseca, J. C. Machado da Silva, C. H. Monken, and S. Pádua, “Controlling two-particle conditional interference,” *Phys. Rev. A* **61**, 023801 (2000).
- [131] E. W. Marchand and E. Wolf, “Angular correlation and the far-zone behavior of partially coherent fields,” *J. Opt. Soc. Am.* **62**, 379 (1972).
- [132] K. W. Chan, J. P. Torres, and J. H. Eberly, “Transverse entanglement migration in hilbert space,” *Phys. Rev. A* **75**, 050101 (2007).
- [133] J. Goodman, *Introduction to Fourier Optics*, 2nd ed. (McGraw Hill, New York, 1996).
- [134] S. Mancini, V. Giovannetti, D. Vitali, and P. Tombesi, “Entangling macroscopic oscillators exploiting radiation pressure,” *Phys. Rev. Lett.* **88**, 120401 (2002).

-
- [135] L. Neves, G. Lima, J. G. Aguirre Gómez, C. H. Monken, C. Saavedra, and S. Pádua, “Generation of entangled states of qudits using twin photons,” *Phys. Rev. Lett.* **94**, 100501 (2005).
- [136] L. Neves, G. Lima, E. J. S. Fonseca, L. Davidovich, and S. Pádua, “Characterizing entanglement in qubits created with spatially correlated twin photons,” *Phys. Rev. A* **76**, 032314 (2007).
- [137] T. Yarnall, A. F. Abouraddy, B. E. A. Saleh, and M. C. Teich, “Synthesis and analysis of entangled photonic qubits in spatial-parity space,” *Phys. Rev. Lett.* **99**, 250502 (2007).
- [138] M. N. O’Sullivan-Hale, I. Ali Khan, R. W. Boyd, and J. C. Howell, “Pixel entanglement: Experimental realization of optically entangled $d = 3$ and $d = 6$ qudits,” *Phys. Rev. Lett.* **94**, 220501 (2005).
- [139] S. P. Walborn and C. H. Monken, “Transverse spatial entanglement in parametric down-conversion,” *Phys. Rev. A* **76**, 062305 (2007).
- [140] G. Taguchi *et al.*, “Measurement and control of spatial qubits generated by passing photons through double slits,” *Phys. Rev. A* **78**, 012307 (2008).
- [141] A. K. Jha and R. W. Boyd, “Spatial coherence of the two-photon field produced by down-conversion using a partially coherent pump beam,” to be submitted .
- [142] G. Gbur and E. Wolf, “Spreading of partially coherent beams in random media,” *J. Opt. Soc. Am. A* **19**, 1592 (2002).
- [143] T. Shirai, A. Dogariu, and E. Wolf, “Mode analysis of spreading of partially coherent beams propagating through atmospheric turbulence,” *J. Opt. Soc. Am. A* **20**, 1094 (2003).

-
- [144] M. Salem, T. Shirai, A. Dogariu, and E. Wolf, “Long-distance propagation of partially coherent beams through atmospheric turbulence,” *Opt. Comm.* **216**, 261 (2003).
- [145] L. Allen, S. Barnett, and M. Padgett, *Optical Angular Momentum* (Institute of Physics Publishing, Bristol, 2003).
- [146] H. H. Arnaut and G. A. Barbosa, “Orbital and intrinsic angular momentum of single photons and entangled pairs of photons generated by parametric down-conversion,” *Phys. Rev. Lett.* **85**, 286 (2000).
- [147] A. Mair, A. Vaziri, G. Weihs, and A. Zeilinger, “Entanglement of the orbital angular momentum states of photons,” *Nature* **412**, 313 (2001).
- [148] S. Franke-Arnold, S. M. Barnett, M. J. Padgett, and L. Allen, “Two-photon entanglement of orbital angular momentum states,” *Phys. Rev. A* **65**, 033823 (2002).
- [149] S. P. Walborn, A. N. de Oliveira, R. S. Thebaldi, and C. H. Monken, “Entanglement and conservation of orbital angular momentum in spontaneous parametric down-conversion,” *Phys. Rev. A* **69**, 023811 (2004).
- [150] S. S. R. Oemrawsingh *et al.*, “Experimental demonstration of fractional orbital angular momentum entanglement of two photons,” *Phys. Rev. Lett.* **95**, 240501 (2005).
- [151] A. Aiello, S. S. R. Oemrawsingh, E. R. Eliel, and J. P. Woerdman, “Nonlocality of high-dimensional two-photon orbital angular momentum states,” *Phys. Rev. A* **72**, 052114 (2005).
- [152] J. P. Torres, A. Alexandrescu, and L. Torner, “Quantum spiral bandwidth of entangled two-photon states,” *Phys. Rev. A* **68**, 050301 (2003).

-
- [153] J. Götte, S. Franke-Arnold, and M. Barnett, “Angular EPR paradox,” *J. Mod. Opt.* **53**, 627 (2006).
- [154] R. A. Beth, “Mechanical detection and measurement of the angular momentum of light,” *Phys. Rev.* **50**, 115 (1936).
- [155] A. K. Spilman and T. G. Brown, “Stress birefringent, space-variant wave plates for vortex illumination,” *Appl. Opt.* **46**, 61 (2007).
- [156] R. Shankar, *Principles of Quantum Mechanics*, 2nd ed. (Kluwer Academic Press/ Plenum Publishers, New York, 1994).
- [157] J. P. Torres, Y. Deyanova, L. Torner, and G. Molina-Terriza, “Preparation of engineered two-photon entangled states for multidimensional quantum information,” *Phys. Rev. A* **67**, 052313 (2003).
- [158] G. A. Barbosa, “Transverse coincidence structures in spontaneous parametric down-conversion with orbital angular momentum: Theory,” *Phys. Rev. A* **76**, 033821 (2007).
- [159] S. Feng and P. Kumar, “Spatial symmetry and conservation of orbital angular momentum in spontaneous parametric down-conversion,” *Phys. Rev. Lett.* **101**, 163602 (2008).
- [160] S. S. R. Oemrawsingh, A. Aiello, E. R. Eliel, G. Nienhuis, and J. P. Woerdman, “How to observe high-dimensional two-photon entanglement with only two detectors,” *Phys. Rev. Lett.* **92**, 217901 (2004).
- [161] N. K. Langford *et al.*, “Measuring entangled qutrits and their use for quantum bit commitment,” *Phys. Rev. Lett.* **93**, 053601 (2004).
- [162] A. K. Jha *et al.*, “Angular two-qubit states and two-photon angular interference,” Submitted to *Phys. Rev. Lett.* .

-
- [163] J. C. Howell, A. Lamas-Linares, and D. Bouwmeester, “Experimental violation of a spin-1 Bell inequality using maximally entangled four-photon states,” *Phys. Rev. Lett.* **88**, 030401 (2002).
- [164] R. T. Thew, S. Tanzilli, W. Tittel, H. Zbinden, and N. Gisin, “Experimental investigation of the robustness of partially entangled qubits over 11 km,” *Phys. Rev. A* **66**, 062304 (2002).
- [165] J. Leach, M. Dennis, J. Courtial, and M. Padgett, “Vortex knots in light,” *New Journal of Physics* **7**, 1 (2005).
- [166] E. Wigner, “On the quantum correction for thermodynamic equilibrium,” *Phys. Rev.* **40**, 749 (1932).
- [167] E. C. G. Sudarshan, “Equivalence of semiclassical and quantum mechanical descriptions of statistical light beams,” *Phys. Rev. Lett.* **10**, 277 (1963).

Appendix A

Calculating $\gamma'(\Delta L')$ for various phase matching conditions

In this appendix, we calculate the time-averaged degree of correlation $\gamma'(\Delta L')$ of the signal-idler field, for various phase matching conditions. $\gamma'(\Delta L')$ is defined in Eq. (2.34) as

$$\gamma'(\Delta L') = \frac{\langle g_1^*(\tau + \tau'_1)g_2(\tau + \tau'_2) \rangle_\tau}{\sqrt{\langle |g_1(\tau + \tau'_1)|^2 \rangle_\tau \langle |g_2(\tau + \tau'_2)|^2 \rangle_\tau}}. \quad (\text{A.1})$$

To calculate $\gamma'(\Delta L')$, we first evaluate the phase-matching function given in Eq. (2.12) and then the function $g_1^*(\tau)$ given in Eq. (2.26). The phase-matching function defined in Eq. (2.12) assumes the following form for the phase-matching function $\Phi_1(\omega'_s + \omega_{s0}, \omega_0 - \omega_{s0} - \omega'_s)$ in alternative 1:

$$\Phi_1(\omega'_s + \omega_{s0}, \omega_0 - \omega_{s0} - \omega'_s) = \int_{-L_1}^0 dz e^{i[k_{pz1}(\omega_0) - k_{sz1}(\omega'_s + \omega_{s0}) - k_{iz1}(\omega_0 - \omega_{s0} - \omega'_s)]z}. \quad (\text{A.2})$$

Here L_1 is the length of the nonlinear crystal in alternative 1 and k_{sz1} and k_{iz1} are the z -component of the signal and idler wavevectors in alternative 1. These wavevectors

are expanded in power series around ω_{s0} and $\omega_0 - \omega_{s0}$ to give

$$\begin{aligned} k_{sz1}(\omega'_s + \omega_{s0}) &= k_{sz1}(\omega_{s0}) + \omega'_s \frac{d}{d\omega'_s} k_{sz1}(\omega'_s + \omega_{s0}) \Big|_{\omega'_s=0} + \dots \\ k_{iz1}(\omega_0 - \omega_{s0} - \omega'_s) &= k_{iz1}(\omega_0 - \omega_{s0}) - \omega'_s \frac{d}{d\omega'_s} k_{iz1}(\omega_0 - \omega_{s0} - \omega'_s) \Big|_{\omega'_s=0} + \dots \end{aligned} \quad (\text{A.3})$$

The ellipses represent higher order terms, which can be neglected for most cases except when degenerate type-I phase-matching is satisfied and the frequency bandwidths of the filters are much broader than the down-conversion bandwidth. This case will be treated separately in the next section. We now assume that perfect phase-matching is satisfied at frequencies ω_0 , ω_{s0} and $\omega_0 - \omega_{s0}$ with $k_{pz1}(\omega_0) = k_{sz1}(\omega_{s0}) + k_{iz1}(\omega_0 - \omega_{s0})$. Thus Eq. (A.2) becomes

$$\Phi_1(\omega'_s + \omega_{s0}, \omega_0 - \omega_{s0} - \omega'_s) = \int_{-L_1}^0 dz e^{-i\omega'_s D_1 z}, \quad (\text{A.4})$$

where

$$D_1 \equiv \frac{d}{d\omega'_s} k_{sz1}(\omega'_s + \omega_{s0}) \Big|_{\omega'_s=0} - \frac{d}{d\omega'_s} k_{iz1}(\omega_0 - \omega_{s0} - \omega'_s) \Big|_{\omega'_s=0} \quad (\text{A.5})$$

is the group velocity mismatch [90] in alternative 1. Since the signal and idler wave-vectors k_{sz1} and k_{iz1} are polarization-dependent, D_1 differs for type-I and type-II phase-matching conditions. By substituting from Eq. (A.4) into Eq. (2.26), we obtain the following expression for $g_1^*(\tau)$:

$$g_1^*(\tau) = L_1 \int_{-\infty}^{\infty} d\omega'_s \text{sinc} \left(\frac{\omega'_s D_1 L_1}{2} \right) f_s(\omega'_s) f_i(-\omega'_s) e^{i\omega'_s(\tau - D_1 L_1/2)}. \quad (\text{A.6})$$

The frequency bandwidths of the signal and idler filters are $\Delta\omega_s$ and $\Delta\omega_i$, respectively; $1/(D_1 L_1)$ is a measure of the down-conversion frequency-bandwidth in alternative 1.

A similar expression for $g_s^*(\tau)$ is obtained:

$$g_2^*(\tau) = L_2 \int_{-\infty}^{\infty} d\omega'_s \text{sinc}\left(\frac{\omega'_s D_2 L_2}{2}\right) f_s(\omega'_s) f_i(-\omega'_s) e^{i\omega'_s(\tau - D_2 L_2/2)}. \quad (\text{A.7})$$

where L_2 is the length of the crystal in alternative 2 and D_2 the group velocity mismatch in alternative 2; $1/(D_2 L_2)$ is a measure of the down-conversion frequency-bandwidth in alternative 2. In two-photon interference experiments in which the same crystal is involved in both the alternatives, L_1 and L_2 are equal. The magnitudes of D_1 and D_2 are also the same; however, D_1 and D_2 may have opposite signs.

Using Eqs. (A.6) and (A.7), we evaluate the time-averaged signal-idler correlation function $\langle g_1^*(\tau + \tau'_1) g_2(\tau + \tau'_2) \rangle_\tau$ to be:

$$\begin{aligned} \langle g_1^*(\tau + \tau'_1) g_2(\tau + \tau'_2) \rangle_\tau &= 2\pi L_1 L_2 \int_{-\infty}^{\infty} d\omega'_s \text{sinc}\left(\frac{\omega'_s D_1 L_1}{2}\right) \text{sinc}\left(\frac{\omega'_s D_2 L_2}{2}\right) \\ &\quad \times |f_s(\omega'_s) f_i(-\omega'_s)|^2 e^{i\omega'_s(\Delta L'/c + D_1 L_1/2 - D_2 L_2/2)}. \end{aligned} \quad (\text{A.8})$$

We now evaluate the time-averaged degree of correlation $\gamma'(\Delta L')$ of the signal-idler field, as defined in Eq. (A.1), for two limiting cases.

A.1 Filter bandwidths much broader than the down-conversion bandwidth

In this case we have $\Delta\omega_s, \Delta\omega_i \gg \frac{1}{D_1 L_1}, \frac{1}{D_2 L_2}$. The product $|f_s(\omega'_s) f_i(-\omega'_s)|^2$ in Eq. (A.8) remains essentially equal to unity over the frequency-range of interest. The time-averaged signal-idler correlation function of Eq. (A.8) can therefore be written as

$$\begin{aligned} \langle g_1^*(\tau + \tau'_1) g_2(\tau + \tau'_2) \rangle_\tau &= 2\pi L_1 L_2 \int_{-\infty}^{\infty} d\omega'_s \text{sinc}\left(\frac{\omega'_s D_1 L_1}{2}\right) \text{sinc}\left(\frac{\omega'_s D_2 L_2}{2}\right) \\ &\quad \times e^{i\omega'_s(\Delta L'/c + D_1 L_1/2 - D_2 L_2/2)}. \end{aligned} \quad (\text{A.9})$$

The above integral can be calculated analytically and the time-averaged degree of correlation $\gamma'(\Delta L')$ of the signal-idler field, of Eq. (A.1), can be shown to be

$$\gamma'(\Delta L') = \frac{|D_1 L_1| + |D_2 L_2|}{2\sqrt{|D_1 L_1 D_2 L_2|}} \text{tri} \left[\frac{D_1 L_1 - D_2 L_2 + \Delta L'/c}{|D_1 L_1| + |D_2 L_2|} \right], \quad (\text{A.10})$$

where the symbol tri stands for the triangle function. We find that $\gamma'(\Delta L')$ is a triangle function and is, in general, not centered at $\Delta L' = 0$ [90, 91]. In the special case when $D_1 L_1 = D_2 L_2 = DL$, the correlation function simplifies to $\gamma'(\Delta L') = \text{tri}[\Delta L'/(cDL)]$. Here $1/DL$ is a measure of the bandwidth of the signal-idler field, and thus cDL can be regarded as the coherence length of the signal-idler field in this case.

The expression for the time-averaged degree of correlation of the signal-idler field given by Eq. (A.10) holds for all phase-matching conditions other than the degenerate type-I phase-matching, in which case $D_1 = D_2 = 0$ and the approximation used in Eq. (A.3) is no longer valid. In the case of degenerate type-I phase-matching, the phase-matching function and thus the time-averaged degree of correlation $\gamma'(\Delta L')$ of the signal-idler field has to be evaluated by repeating the above calculation while keeping the higher order terms in Eq. (A.3). The exact calculation is slightly involved [91]. However, we note that for degenerate type-I phase-matching, the phase-matching function $\Phi_1(\omega'_s + \omega_{s0}, \omega_0 - \omega_{s0} - \omega'_s)$ in Eq. (A.2) remains symmetric with respect to the signal and idler frequencies. Thus, to a good approximation $\Phi_1(\omega'_s + \omega_{s0}, \omega_0 - \omega_{s0} - \omega'_s)$ can be treated as a Gaussian function and therefore the time-averaged degree of correlation $\gamma'(\Delta L')$ of the signal-idler field can be written as $\gamma'(\Delta L') = \exp[-(1/2)(\Delta L' \Delta \omega/c)^2]$, where $\Delta \omega$ is the effective signal-idler frequency bandwidth. In most cases, $\Delta \omega$ is decided by the limiting apertures of the detection system [3].

A.2 Filter bandwidths much narrower than the down-conversion bandwidth

In this case we have $\Delta\omega_s, \Delta\omega_i \ll 1/D_1L_1, 1/D_2L_2$. The product of the sinc functions in Eq. (A.8) remains essentially equal to unity over the frequency range of interest. Eq. (A.8) can therefore be written as

$$\begin{aligned} \langle g_1^*(\tau + \tau'_1)g_2(\tau + \tau'_2) \rangle_\tau &= 2\pi L_1L_2 \int_{-\infty}^{\infty} d\omega'_s \\ &\times |f_s(\omega'_s)f_i(-\omega'_s)|^2 e^{i\omega'_s(\Delta L'/c + D_1L_1/2 - D_2L_2/2)}. \end{aligned} \quad (\text{A.11})$$

We assume Gaussian transmission functions for the two filters, with rms frequency bandwidths given by $\Delta\omega_s$ and $\Delta\omega_i$. Eq. (A.8) can now be evaluated analytically and the time-averaged degree of correlation $\gamma'(\Delta L')$ of the signal-idler field can be shown to be

$$\gamma'(\Delta L') = \exp \left[-\frac{\Delta\omega^2}{2} \left(\frac{D_1L_1}{2} - \frac{D_2L_2}{2} + \frac{\Delta L'}{c} \right)^2 \right], \quad (\text{A.12})$$

with $1/\Delta\omega^2 = 1/\Delta\omega_s^2 + 1/\Delta\omega_i^2$. In the special case when $D_1L_1 = D_2L_2$ the above equation simplifies to $\gamma'(\Delta L') = \exp [-(1/2)(\Delta L'\Delta\omega/c)^2]$, where $\Delta\omega$ represents the bandwidth of the signal-idler field, and thus $l_{\text{coh}} = c/\Delta\omega$ can be referred to as the coherence length of the signal-idler field.

Appendix B

Induced coherence experiment

In this appendix, we describe Mandel’s famous “induced coherence experiment [4],” using the formalism developed in Chapter 2 for describing temporal two-photon interference effects. The schematic of the experiment is depicted in Fig. B.1. In this experiment, two parametric down-converters (PDC1 and PDC2) are pumped coherently. When the paths of the idler photons (i_1 and i_2) are aligned, one-photon fringes are observed at detector D_A as the beam splitter position x is varied. To explain this effect, we first calculate the coincidence count rate R_{AB} of detectors D_A and D_B . From the two-photon path diagrams shown in Fig. B.1(b), one finds that that $\Delta L = x \cos \theta$, $\Delta L' = 2x \cos \theta$ and $\Delta \phi = \pi$. Substituting these quantities into Eq. (2.39), we obtain

$$R_{AB} = C [1 - \gamma'(2x \cos \theta) \gamma(x \cos \theta) \cos(k_0 x \cos \theta)]. \quad (\text{B.1})$$

Next, we calculate the coincidence count rate R_{CB} of detectors D_C and D_B . From the two-photon path diagrams shown in Fig. B.1(c), we have, $\Delta L = -x \cos \theta$, $\Delta L' = -2x \cos \theta$ and $\Delta \phi = 0$. Substituting these quantities into Eq. (2.39), we obtain

$$R_{CB} = C [1 + \gamma'(2x \cos \theta) \gamma(x \cos \theta) \cos(k_0 x \cos \theta)]. \quad (\text{B.2})$$

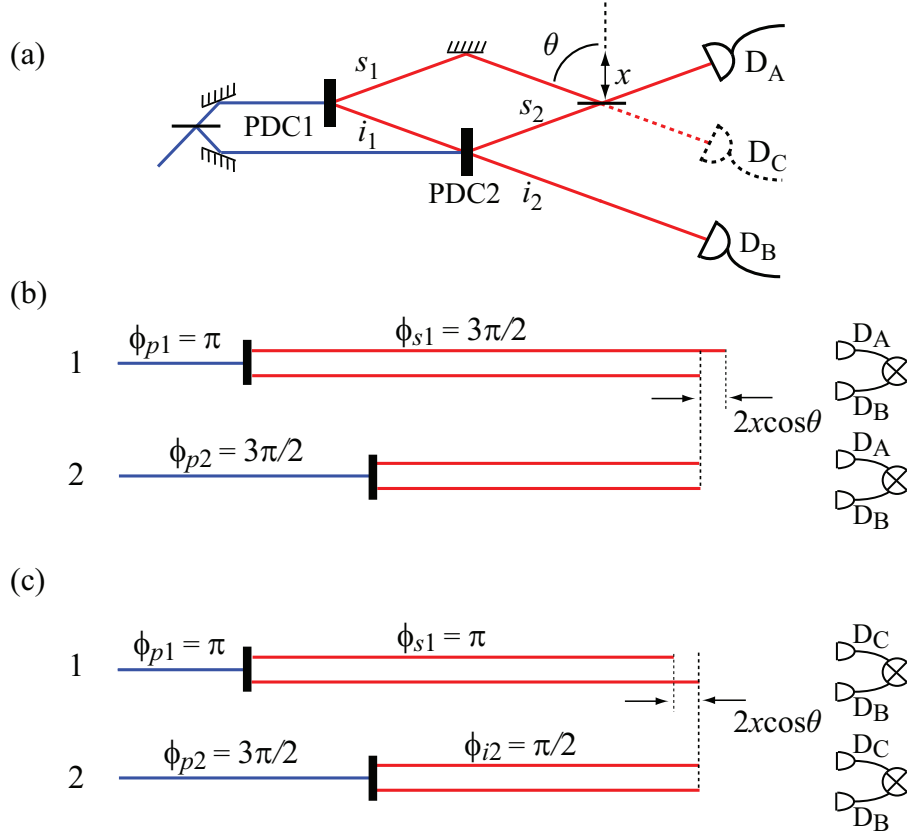


Figure B.1: (a) The schematic setup for the induced-coherence experiment [4]. In alternative 1, the pump photon gets down-converted in PDC1 while in alternative 2, it gets down-converted in PDC2. (b) Two-photon path diagrams representing the alternative pathways by which the signal and idler photons can get to detectors D_A and D_B . (c) Two-photon path diagrams representing the alternative pathways by which the signal and idler photons can get to detectors D_C and D_B .

To calculate the one-photon count rates at detectors D_A and D_B , we note that the twin of a photon detected at D_A can go only to D_B while the twin of a photon detected at D_B can go to both D_A and D_C . Therefore, using Eqs. (2.46), we find that the one-photon count rates R_A and R_B at detectors D_A and D_B , respectively are given as:

$$R_A = R_{AB} \quad \text{and} \quad (\text{B.3})$$

$$R_B = R_{AB} + R_{CB}. \quad (\text{B.4})$$

Using Eqs. (B.1) and (B.2), we then obtain

$$R_A = C [1 - \gamma'(2x \cos \theta) \gamma(x \cos \theta) \cos(k_0 x \cos \theta)], \quad (\text{B.5})$$

$$R_B = 2C. \quad (\text{B.6})$$

The one-photon count rate R_A at detector D_A thus shows interference fringes as a function of x whereas the one-photon count rate R_B at detector D_B does not. These were the results reported in Ref. [4] and explained in terms of ‘induced coherence’. Here we have shown that they can also be explained in terms of two-photon interference effects alone.